STUDY OF KINEMATICS OF EXTREME WAVES IMPACTING OFFSHORE AND COASTAL STRUCTURES BY NON INTRUSIVE MEASUREMENT TECHNIQUES

A Dissertation

by

YOUN KYUNG SONG

Submitted to the Office of Graduate and Professional Studies of
Texas A&M University
in partial fulfillment of the requirements for the degree of

DOCTOR OF PHILOSOPHY

Chair of Committee,	Kuang-An Chang
Co-Chair of Committee,	Jennifer L. Irish
Committee Members,	Richard Mercier
	Robert Hetland
Head of Department,	Robin Autenrieth

December 2013

Major Subject: Civil Engineering

ABSTRACT

Extreme wave flows associated with a large scale wave breaking during interactions with marine structures or complex coastal geography of is one of the major concerns in a design of coastal and ocean structures. In order to properly understand the impact mechanisms of breaking extreme waves, full field evaluations of impacting multiphase flow velocities should be properly conducted first. In this context, this present dissertation experimentally investigated velocity structures of turbulent, multiphase wave flow velocities during active interactions with various offshore and onshore ocean environments.

First, initial inundation flow structures of tsunami-like long waves interacting with complex coastal topography are experimentally investigated. Turbulent wave surface velocities were effectively measured by introducing a non-intrusive video imagery technique, the “wave front tracing method”. Three distinctive configurations for patch layouts that vary either in characteristic patch diameter (D) or in center-to-center spacing between patches (ΔS) were employed. That is, patch layouts consisted of six (G1) and twelve (G2), “small” circular macro roughness patches of D =1.2 m and six, “large” circular macro roughness patches (G3) of D = 1.7 m were employed, respectively. A patch layout employed for G1 appears to be effective in reducing the u velocities along the centerlines of the reference patch that consistently decreased to 85% of a convergence velocity U = 2m/s and to 45% of U. However, in the channel, u velocities hardly reduced below the convergence velocity. On the other hand, the patch layout G2 is observed as rather effective in uniformly reducing the u velocities alongshore. The hand, the patch layout G3 is observed as effective in suppressing the alongshore variability in flow behind the frontal patches. This may be due to the "holding-up" effects produced by the large patches holding the flow within the patch for a longer duration. Furthermore, such a "holding-up" effect from G3 appears to induce a large inundation depth in the flow along the opening.

Next, green water velocities and dynamic impacts of the extreme ocean waves on a fixed offshore deck structure are investigated. The experiments focused on the impacting waves generated in a large-scale, three-dimensional ocean wave basin. Using the BIV technique, overall flow structures and temporal and spatial distributions of the maximum velocities were successfully evaluated. The most significant spatial variability in mean velocities in the propagating direction was found from the protruding wave front near the center of the deck during early stages of the wave run-up. The maximum front speed of 1.4C was first observed in

the center of the deck near y = 0 at a midpoint of the deck (x = 0.5*L*), where *C* is the wave phase speed. The flow velocities started decreasing below 1*C* over all fields once the wave frontal flow passed the rear edge and started leaving the deck. Pressure measurements were also conducted at four different vertical positions on vertical measurement planes at three different locations on the horizontal plane. Most of measured pressures showed impulsive impact patterns with sudden rises of pressure peaks. The highest pressure was observed as $1.56\rho C^2$ at x = *L*/2. Correlations between wave kinematic energy and dynamic pressure were examined to determine the impact coefficients c_i'. c_i' varied within relatively narrow ranges $0.29 \leq c_i' \leq 1.56$. In the present large scale experiments, the impact pressures on the structures are strongly affected by both variability of flow structures and impulsiveness of impacting waves containing considerable air volumes.

Lastly, the study is extended for more violent sloshing wave flows. The study experimentally investigated flow kinematics and impact pressures of a partially filled liquid sloshing flow during the periodic longitudinal motion of a rectangular tank. The horizontal velocities near the free surface reached 1.6*C* with *C* being the wave phase speed calculated based on the shallow water assumption. As the tank reached its maximum displacement and about to reverse, the dominant flow changed its direction rapidly to vertical upward after the breaking wave crest impinging on the side wall and forming an up-rushing jet. The vertical velocity of the rising jet reached 3.4*C* before it impacted the top wall. During the flip-through event as the fast moving wave crest collided with the side wall, the steep wave crest resulted in a focused impact on the side wall at the SWL. The resulting impulsive peak pressure was recorded as about $10\rho gh$ immediately followed by the evident pressure oscillation with a frequency approximately 500 Hz. After the wall impact, the multiphase up-rushing jet shot up and impacted the top wall. The magnitude of the pressure was again about $10\rho gh$, similar to that recorded by the breaking wave impact on the side wall. Correlating the dynamic impact pressures with the corresponding local maximum flow velocities in the direction normal to the walls was performed by introducing the impact coefficient c_i and the modified impact coefficient c_i', defined as $p_{\max} = c_i \rho V_{\max}^2 = c_i' \rho C^2$ with $V_{\max}$ being the magnitude of the maximum local velocities. The average values of the modified impact coefficient c_i' between the side wall impacts and the top wall impacts were nearly identical, with the average value of $c_i' = 5.2$.

DEDICATION

This dissertation is dedicated,
with love and respect,
to my husband and our sister, brothers, and parents.

AKNOWLEDGEMENTS

I would like to first thank my advisor, Dr. Kuang-An Chang, for his guidance and advice. This dissertation could not have been completed without his insight, experience and comments. I also deeply appreciate his continuous encouragement from the beginning of the study.

I also would like to thank my advisor, Dr. Jennifer Irish, for her time, leadership and dedication. Her example as a professional researcher will carry with me throughout my career and her commitment to teaching and research was an inspiration.

I would like to thank the rest of my committee members, Dr. Richard Mercier, for his continuous guidance and support throughout the course of this research, and Dr. Robert Hetland, for his advice and commitment to teaching.

Thanks go to my senior research mate and mentor, Dr. Ho Joon Lim, who and helped me to learn the laboratory methods used in this dissertation and aided in my initial understanding of BIV processing. I would like to thank Yong Uk Ryu and Dr. Kusalika Ariyarathne for their help, friendship and encouragement. Thanks to the staff at Offshore Technology Research Center for their technical support and friendly aids and also wish to thank staff at O.H. Hinsdale Wave Research Laboratory for their assistant and collaboration during my laboratory research.

Lastly, I would like to express my special gratitude and love to my husband, Aldric Baquet, my parents, and parents-in-law. I am also thankful to my brother, Min Soo Song, and my sister, Youn Jung Song. This dissertation would not have been possible without their invaluable love, trust, encouragement, and support.

TABLE OF CONTENTS

Page

LIST OF FIGURES

Page

Page

LIST OF TABLES

Page

CHAPTER I

INTRODUCTION

I.1 Flow characteristics during extreme wave breaking and interactions with ocean structures

Extreme wave flows associated with a large scale wave breaking during interactions with marine structures or complex coastal geography of is one of the major concerns in a design of coastal and ocean structures. When intensified under severe weather condition and by extreme geophysical force such as hurricane and earthquake, ocean waves increase wave heights and reach above the deck of marine structures producing highly aerated overtopping wave flow associated with fast flows and wave forces. When the wave breaks prior to reaching a coastal shoreline, the broken wave undergoes rapid deformation and develops air-water mixed fluid structures that form a turbulent frontal face near the free surfaces.

If the extreme wave accompanies aerated bores on the surface, it induces increased shear frictions and randomness in the velocity structures during the wave runup. Furthermore, the breaking wave entraps air bubbles of various sizes beneath the free surface and form a water-air mixed flow. The flow aeration during the wave breaking process affect various dynamic properties of wave flows, such as impact pressure, viscosity, and surface tension, that are impossible to evaluate without considering kinematic features of the wave flows. On the other hand, due to increased randomness in the motion and inhomogeneity of the multiphase fluids, some techniques customarily implemented for the velocity measurements of moderately evolving flow are inadequate to capture full-field evolutions of fast-varying breaking flows.

Therefore, in order to properly understand the impact mechanisms of breaking extreme waves, full field evaluations of impacting multiphase flow velocities should be properly conducted first. Furthermore, the dynamic wave impact pressures measured from the scaled hydraulic model tests often fail to simulate the effect of such air entrapment; hence the measurement results are need to be properly interpreted in order to account for the “scale effect” present in the laboratory test results prior to general applications.

In this context, this present dissertation experimentally investigated velocity structures of turbulent, multiphase wave flow velocities during active interactions with various offshore and onshore ocean environments.

I.2 Outlines of this dissertation and objectives of each chapter

In CHAPTER II, the study experimentally investigated initial inundation flow structures of tsunami-like long waves interacting with complex coastal topography. Due to the instability of fluid composition and variability of the wave front lines during wave runup over the vegetated fields, the measurements of wave surface using typical in-situ measurements are ineffective. Therefore, for measurements of turbulent wave surface velocities, this present study developed a "wave front tracing method", implementing non-intrusive video imagery techniques. Specifically, the objectives of this chapter are to present an optic methodology that continuously traces and evaluate turbulent wave front velocities and to evaluate effects of different vegetation patch configurations on the initial flow patterns of tsunami inundation flows during initial run up of turbulent wave bores.

In CHAPTER III, the study conducted the laboratory investigations to measure the green water velocities and dynamic impacts of the extreme ocean waves on a fixed offshore deck structure. The experiments focused on the impacting waves generated in a large-scale, three-dimensional ocean wave basin. The Bubble Image Velocimetry (BIV) developed for the highly aerated, turbulent flow velocities were employed for calculations of the green water flow velocities. Ultimately, this study aims to provide quantitative estimations for potential wave impacts on offshore structures associated with both kinematic and dynamic characteristics of extreme ocean waves.

In CHAPTER IV, the study is extended for more violent sloshing wave flows. The study experimentally investigated flow kinematics and impact pressures of a partially filled liquid sloshing flow during the periodic longitudinal motion of a rectangular tank. The study focused on quantifying the flow velocities and impact pressures induced by the flow. The study aims to obtain full-field flow velocities, and to investigate possible correlation between impact potential of the sloshing liquid kinematics and the dynamic response in term of pressure on the liquid container in simple oscillatory motion.

CHAPTER II

TSUNAMI-LIKE LONG WAVE KINEMATICS AROUND MACRO-ROUGHNESS PATCH TYPE VEGETATION

II.1 Introduction

Since the disastrous 2004 Indian Ocean tsunami, research has concentrated more actively on investigation of the functionality of coastal vegetation as a defensive mechanism during extreme wave inundation. Laboratory experiments have focused on the macro roughness effects from a single vegetation patch or a simple green belt layout composed with a uniform opening across a shore. Tsunami wave runup was often simulated as uniform or quasi-uniform open channel flows with controlled incoming velocities and depth. However, evolutions of tsunami inundation flow exhibit much complexity in both the surface elevation profile and propagation velocities. Moreover, the interaction between the tsunami inundation flow and discontinuous macro roughness structures in the coastal vegetation system promotes dynamic variability in the flow depth and speed. Therefore, employment of the discontinuous, patch-type coastal vegetation must be conducted based on an understanding of the effect of spatial variability in the macro roughness resistance on dynamic evolutions of the runup flow patterns with tsunami-like wave conditions.

II.1.1 Characteristics of tsunami inundation flows propagating with a turbulent bore front

Progressive waves advancing into shallow water over a mildly sloping beach develop a steep frontal face in response to water depth limits, causing acceleration in horizontal water velocities (Airy, 1845). If the shallow-water steepening is rapid due to large variations in water depth (e.g., a beach slope >1/50; Miller, 1968), the steep-fronted wave breaks far ahead of the shore. When the broken long wave travels a sufficient distance before running up, the wave flow develops turbulent bore fronts that appear as white, wall-like formations of foaming water, as seen during tsunami inundation during the disastrous 2004 Indian Ocean tsunami (e.g., Lynett, 2011).

Despite energy loss and turbulence dissipation after the wave breaks, evidence has shown that the tsunami inundation with a fully developed bore front delivers devastating tsunami forces on the shore (Yeh and Mok, 1990; Yeh,1991). In fact, the maximum runup height of fully broken

tsunami waves was found to be lower on a beach than that of unbroken waves of equivalent energy potential. Yeh (1991) also observed significant variations in the wave front velocities during this "momentum exchange" process: it first reduced rapidly down to 20% of a convergence velocity U (predicted based on a shallow-water theory) at the shoreline as it pushed up the still water. Then the consequential runup flow accelerated up to 90% of U until it again decreased gradually on the beach. In conclusion, Yeh postulated that the enormous impacts on the shore observed during past tsunami disasters must be largely attributed to the bore impacts: the sudden release of turbulent energy at the wave front during tsunami runup.

The degrees of wave energy dissipation during tsunami runup are affected by both the rate of variation in water depth (e.g., steepness of bottom slope) and natural bottom roughness (Miller, 1968). Macro-roughness obstacles as engineered tsunami damage reduction enhance the local variability of inundation flow patterns (e.g., Tomita and Honda, 2007). Especially, the presence of vegetation arrays induces large-scale variability in flow depth and direction around discontinuous interfaces, where macro-roughness density changes. Consequently, velocity structures developed in connection with the spatial variability of vegetation roughness affect flow channelization and turbulence production. This significantly alters inundation flow dynamics. Therefore, any design of the coastal vegetation zone must be based on an integrated understanding of the vegetated flow dynamics, the kinematic behavior of the most impactive turbulent inundation bores and the complexity of a given coastal topography.

Accurate vegetated flow research requires more supporting data regarding turbulent wave kinematics, either by means of field surveys or by laboratory physical-model studies. While data collected through post-tsunami surveys may be effectively in providing evidence of the maximum water levels and flow pathways at the site, it is hard to directly extract information about temporal and spatial variations in inundation flow velocities. Furthermore, in order to validate model predictions of breaking turbulent flows, experimental investigations on the complex vegetated flow field are also essential. Few laboratory studies have employed inundation flows from tsunami-like long waves to investigate the fluid kinematics of complex terrain.

II.1.2 Flow characteristics within emergent vegetation

Inundation flows propagate inland while interacting with various coastal features, either natural (e.g., forests, sediments) or artificial (e.g. houses, shore defense structures). Bottom

friction provided by natural bottom topography (e.g., relatively smooth sands) may be minor, while bottom irregularity or increased roughness due to structures with massive volume and macro-roughness may produce significant changes in flow directions and speeds as well as on energy dissipations of inundation flows.

Several post-tsunami research investigations have provided evidence demonstrating the influence of shore-defensive structures, such as reefs, seawalls, and dunes, on variability of inundation depth and flow velocity impact (e.g., Cross, 1967; Synolakis et al., 1995; Borrero et al., 1997; Fernando et al., 2008). Numerous field investigations have followed recent historic tsunami events such as the 1998 Papua, New Guinea, Tsunami and the 2004 Indian Ocean Tsunami (e.g., Danielsen et al., 2005; Dahdouh-Guebas et al., 2005; Liu et al., 2005; Forbes and Broadhead, 2007; Tanaka et al., 2007; Nandasena et al., 2008; Kaplan et al., 2009; Tanaka, 2009). These studies found evidence of a correlation between badly damaged areas and absence of coastal forests (e.g., Forbes and Broadhead, 2007). Consequently, more research interest has been drawn to the role of the "natural" macro-roughness provided by coastal vegetation systems, such as trees, mangrove, and salt marshes, in mitigating tsunami wave impacts.

The presence of finite vegetation arrays, namely vegetation patch or canopy, provides additional drag resistance and eddy viscosity on the mean flow velocities U. Various scales of spatial variation in the characteristics of the vegetation canopy contribute to the effect, limiting the flow patterns differently during the advection, energy dissipation, and turbulence production processes of the mean vegetated flow. Nepf (1999, 2004, 2012) has categorized a range of characteristic length scales that increases from a stem scale d or a stem spacing scale Δs to a patch scale L_a over which the stem density a (m^{-1}) varies. This study explains their respective contributions to the mass transport mechanisms on different stages of kinematic conditions. Of particular interest, the study finds that for the flow structure within a scope larger than L_a, the advection produced by the variation in the mean velocity U due to differences in density over L_a was found to be a dominant force inducing the longitudinal dispersion of the flow (Nepf, 1999).

Following is a summary of Nepf's vegetated flow dynamic model (2004), describing the mean flow velocities associated with emergent vegetation resistance.

The spatial variability of the vegetation density has a major effect on velocity structures of flows in and around the vegetated region. Nepf (1999, 2004) introduced a definition for the stem density a (m^{-1}) that represents the nominal area of plants projected on a plane perpendicular to the incoming flow direction:

$$a = nd = \frac{d}{\Delta s^2} \tag{1}$$

where

- d is the mean stem diameter,
- Δs is the mean spacing between neighboring stems, and
- n is the mean number of stems (cylinders) within a horizontal length scale of a patch L_a (>> d or Δs).

Note that for vegetation arrays of width W (in the x direction), unit length (in the y direction), the stem density ϕ (number of trees/m^2) is defined with ad (Tanaka et al., 2007) as:

$$\phi = \frac{n}{W \times 1} = \frac{1}{\Delta s^2} = \frac{a}{d}, \tag{2}$$

hence, $\phi = \frac{n}{W \times 1} = \frac{1}{\Delta s^2} = \frac{a}{d}$. Within a patch spanning over a length scale L_a, the vegetation characteristics (e.g., d, Δs) are assumed as homogeneous.

Figure II-1 defines a control volume of the vegetated flow field. The dominant flow is in the x direction with a mean fluid velocity U within the length scale $L_a \gg \Delta s, d$ (with constant vegetation characteristics $\Delta s, d$). The control volume is determined to evaluate the momentum balance between the fluid and net forces acting on a control volume $\partial x \partial y \partial z$. Here,

- x_1 and x_2 are lower (flow entries) and upper (flow exits) boundaries, respectively, of the control volume in the x direction, where $x_1 \le x \le x_2$,
- y_1 and y_2 are lower and upper boundaries, respectively, of the control volume in the y direction, where $y_1 \le y \le y_2$,
- z_1 and z_2 are lower and upper boundaries, respectively, of the control volume in the z direction, where $z_1 \le z \le z_2$ and $z_2 \le l$ for the emergent vegetated flow.

Therefore, the horizontal and vertical ranges of the control volume are $\partial x = x_2 - x_1$, $\partial y = y_2 - y_1$, and $\partial z = z_2 - z_1$, respectively, where the spatial scale is chosen to be larger than Δs or d in any direction.

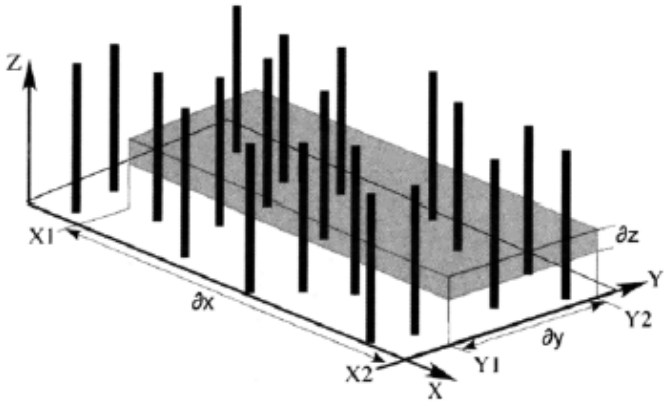

Figure II-1 Definition sketch of control volume of vegetated flow (from Nepf, 2004)

Nepf (2004) stated the equation of momentum conservation for the control volume $\partial x\partial y\partial z$ within the vegetation consisting of cylindrical stems as:

$$\rho\frac{\partial U}{\partial t}\partial x\partial y\partial z\left(1-\frac{\pi}{4}ad\right)+\rho\left(U^2\Big|_{x_2}-U^2\Big|_{x_1}\right)\partial y\partial z\left(1-ad\right)=\sum F_x \quad (3)$$

Here, $U^2\Big|_{x_1}$ and $U^2\Big|_{x_2}$ denote the U^2 evaluated at x_1 and x_2, respectively. Mean velocity U is assumed as a vertically averaged velocity over a scale greater than Δs or d but smaller than L_a. The net force acting on the control volume at the scale being considered is the sum of pressure force that is defined by assuming the hydrostatic pressure (P) gradients as

$$P=-\rho g\frac{\partial H}{\partial x}\left(1-ad\right)\partial x\partial y\partial z \quad (4)$$

the net fluid shear stress (T) as

$$T=\frac{\partial \tau}{\partial z}\left(1-\frac{\pi}{4}ad\right)\partial x\partial y\partial z \quad (5)$$

the body force accounting for the gravitational force (G) of the fluid over the bed slope S as

$$G=-\rho gS\left(1-\frac{\pi}{4}ad\right)\partial x\partial y\partial z \quad (6)$$

and the vegetation drag force (F_v) as

$$F_v = -\frac{1}{2}\rho\widetilde{C_D}aU^2\partial x\partial y\partial z \tag{7}$$

where

- H is the inundation flow depth and
- $\widetilde{C_D}$ is the vegetation drag coefficient evaluated as an averaged value over the multiple stems within $\partial x\partial y \gg \Delta s^2$.

If we equate Eqn. (3) to Eqn. (4) - (7) and assume unit volume $\partial x\partial y\partial z \approx 1$, Eqn. (3) may be restated as:

$$\rho\frac{\partial U}{\partial t}\left(1-\frac{\pi}{4}ad\right)+\rho U\frac{\partial U}{\partial x}(1-ad)= \\ -\rho g\frac{\partial H}{\partial x}(1-ad)+\frac{\partial \tau}{\partial z}\left(1-\frac{\pi}{4}ad\right)-\rho gS\left(1-\frac{\pi}{4}ad\right)-\frac{1}{2}\rho\widetilde{C_D}aU^2 \tag{8}$$

In order to provide a general description of the flow-vegetation interactions, assume that the flow within the spatial scale L_a is steady and uniform. For simplicity, we may approximate the fluid volume fraction as $1-\frac{\pi}{4}ad = 1-ad$. Because the fluid surface's shear is assumed as insignificant when $H/l < 1$ after integration over depth H, when we divide both sides by $1-\frac{\pi}{4}ad (or\ 1-ad)$, Eqn. (8) can be simplified as:

$$\rho g\left(S+\frac{\partial H}{\partial x}\right)H = \tau_b - \frac{1}{2}\rho C_D aU^2 H \tag{9}$$

where τ_b denotes bed stress.

Eqn. (9) states that the fluid force is balanced by the bed stress and that drag resistance is balanced by vegetation. This also means that with a sufficiently dense vegetation stem relative to the water depth above the fixed bed slope (e.g., $aH > 0.3$, which is a typical marsh condition according to Nepf, 2004), the vegetation decreases the effect of bed stress relative to the drag force. Furthermore, the focus is limited for the vegetation in emergent or nearly emergent conditions ($H/l \leq 1$); hence, viscous stresses on the bottom are assumed to be negligible. In addition, when the spatial scale of the water depth is sufficiently larger than the length scale of

turbulence eddies (~*d*), thus ignoring the effect of turbulence stress, Eqn. (9) can be further simplified to account for the balance between fluid force and the vegetated drag force:

$$\rho g\left(S+\frac{\partial H}{\partial x}\right)=-\rho C_D^{'} aU \quad . \tag{10}$$

Here, C_D' is the linear drag coefficient. Introducing hydraulic gradient $i = S + \partial h/\partial x$ allows derivation of the relationship between flow velocity and vegetated drag by Darcy's law (1979):

$$U=-\frac{g}{C_D^{'} a}i \quad . \tag{11}$$

Eqn. (10) and (11) show that the principal determinants of dominant driving force and mean flow velocity profile around a vegetated region are inundation depth *H* relative to the height of the vegetation patch *l* and drag within the vegetated area aC_D'. This suggests that investigation of vegetated flow velocities, by accounting for the effects of stem size and density, can aid the study of spatial variations of vegetation drag resistance. In emergency conditions, the C_D increases with *ad* and also with the stem Reynolds number $Re_{d-} = Ud / \nu_m$ (where ν_m is the molecular kinematic viscosity) until Re_d < 100. However, C_D tends to remain nearly constant at ~1 within 100 < Re_d < 3×10^5, which is a typical flow state in the coastal vegetation systems covering both laminar and turbulent (Re_d > 200) flow regimes (Nepf, 1999).

Furthermore, the wake structure generated by the viscous drag of the vegetation stems provides for dissipation of the mean flow energy and its conversion for turbulence production when Re_d < 200. Raupach and Shaw (1982) define spatially averaged turbulence energy production per unit mass per unit time (P_w in m^2/s^2) with vegetation stem density *a* as:

$$P_w=\frac{1}{2}C_D aU^3 \quad . \tag{12}$$

With the weakened effect of bed friction on turbulence production in the presence of vegetation stems, the rate of turbulent energy production can be evaluated by the rate of the mean energy loss within the vegetated flow. Therefore, Eqn. (12) allows evaluation of the viscous dissipations ε by approximating $P_w = \varepsilon$. This relationship can be extended to evaluate the turbulent kinetic energy *k* at stem scale (~*d*) by:

$$\varepsilon \approx k^{3/2}/d \quad . \tag{13}$$

Typically, turbulence intensity increases with *ad* due to increased wake production. However, the increase in *ad* also results in a decrease of the flow speed *U*. Such nonlinear

balance between k and U is almost impossible to predict analytically. Thus, more active investigations are needed in order to develop turbulence dissipation models. Therefore, it is essential to gain additional information on vegetated flow velocity structure over spatial extents where vegetation roughness varies in order to gain enhanced understanding of the physics governing the variability of C_D and turbulence production, both of which impact flow inundation patterns and consequential damage processes. Furthermore, such study can provide physical data for further development of numerical models.

II.1.3 Reviews of vegetated flow research emphasizing patch-type vegetation roughness

Early research on vegetated flow mechanics was conducted for small-scale (~d) flow structures focusing on flow interference by small numbers of circular cylinders. Numerous studies have been conducted to simulate the flow through rigid, emergent vegetation using circular cylinders, investigating the variation in flow depth, velocity, and bulk drag coefficient at various stages of flow passage (e.g., Raupach, 1992; Luo et al., 1996; Nepf, 1999; Stone and Shen, 2002). Physical description of the flow mechanics has been a major focus: inducing eddy generations, vortex shedding, and downstream Reynolds shear stress ($\rho\overline{u'v'}$) in the flow around the side-by-side cylinder arrays (Sangani and Acrivos, 1982; Koch and Ladd, 1997; Zdravkovich, 1977; Tatsuno et al.,1998; Sumner et al., 2000; Lam et al., 2003; Akilli et al., 2004; Wang and Zhou, 2005). Typically tested parameters include arrangement, ratio of spacing to cylinder diameter, and characteristics of incoming flows (i.e., Re_d).

On the other hand, actual coastal vegetation systems are built with patch-type forests, consisting of large numbers of stands with complex aerial structures (e.g., Jarvela, 2002; Zong and Nepf, 2010). Patch vegetation is defined as a multi-cylinder arrangement with a finite outer radius of a length scale (~L_a), within which the characteristic cylinder stem size and density (d or $\Delta s << L_a$) are homogeneous. Figure II-2 shows examples of the patch-type coastal vegetation.

(a)  (b) 

Figure II-2 Examples of the patch-type coastal vegetation. (a) Isolated tress in patch at Shark River Slough in southern Florida (Short, N., M., Sr., 2005), (b) Tidal marsh along the Edisto River, South Carolina (United States Environmental Protection Agency, 2013)

The finite macro roughness from patch-type vegetation has demonstrated effectiveness in reducing water depth and flow velocities behind the vegetated area. However, negative effects are also present, mainly caused by the discontinuity in drag resistances between discrete vegetation patches. For example, the open gaps perpendicular to the shoreline between finite vegetation zones, such as those created by roads, serve as a pathway for tsunami inundation flows. This enhances the inland runup extents both horizontally and vertically (Fernando et al., 2008; Mascarenhas and Jayakumar, 2008). Furthermore, variations in C_D along the interface between a patch and a free stream region promote lateral transports of water over a length scale larger than L_a. This results in rapid variations in the lateral flow velocities that, in turn, create a large-scale shear-layer vortex ($\approx L_a$) structure around the outer boundary of a patch (Chu et al., 1991; Lawrence, 1995; White and Nepf, 2008; Zong and Nepf, 2010, 2011). Recent investigations have focused on the influence of the geometrical characteristics of a single or finite macro roughness patch (i.e., a "clump-type" vegetation model for randomly distributed stem arrays or a "colony-type" model for staggered or parallel arrangements) on the large-scale ($\geq L_a$) velocity variability in surrounding flows.

Zong and Nepf (2010) have investigated variations in both streamwise and lateral velocities with an emergent vegetation patch uniformly occupying half the flume channel. They observed that, at the leading edge of the patch, the vegetation reduced the flow speed in the streamwise direction and diverted it toward the open channel, increasing the lateral velocities. The dense

patch (volume fraction $\phi = 0.1$) tended to decrease the streamwise velocities more efficiently within the patch, reducing them nearly to zero. However, only about 20% reduction relative to the initial velocity was observed in the rear portion of the patch with coarse density ($\phi = 0.02$). The lateral velocities at the leading edge of the patch increased sharply to 20~70% of the initial velocities.

Zong and Nepf (2011) studied vortex structures behind a single circular patch made with rigid circular cylinders. They observed a steady wake region behind a patch where the downstream velocities decreased and became nearly steady due to porous roughness. Both the steady wake velocities and the longitudinal length demonstrated steady wake lasts decreasing with increasing volume fractions. On the other hand, with solid obstructions, velocity recovery started right behind the patch end without a steady wake zone presented.

Takemura and Tanaka (2007) have investigated the flow structures around an emergent patch ("colony-type" roughness model) consisting of seven equally spaced cylinders in both staggered (space between cylinders *L* is same in every direction) and parallel arrangements. They observed that a small gap between cylinders ($L/d < 3$) within a patch caused significant variations in velocities between the flow beside and behind individual cylinders that led to a large scale (>> d) vortex street (LKV) downstream of the patch. At L/d = 3, a stable, primitive Kármán vortex street (PKV) at a stem scale was achieved, while the velocities and drag resistance within a patch tended to increase until $L/d \leq 3$.

Some research has focused on quantifying the effects of discontinuity in vegetation forests with regard to enhancements of flow speed and inundation water depth in the channel formed by the open gap between finite vegetation patches (Nandasena et al., 2008; Tanimoto et al., 2008; Thuy et al., 2009, 2010). They commonly found significant increases in maximum velocities at the exit of the open gap between coastal forest belts. The increases varied depending mainly on the widths of the opening on a fixed wave condition (Tanimoto et al., 2008). Even a narrow open gap effectively promoted velocity accelerations (Nandasena et al., 2008), while the water depths at the exit were generally decreased. The cross-shore velocities behind the end of the open gap between vegetation belts tended to increase more rapidly in the beginning of flow exits: up to 1.7 times higher than that measured without vegetation (Thuy et al., 2009). The negative effects due to discontinuity in vegetation could be reduced either by constructing the open channel with an orientation inclined to the dominant flow direction or by arranging the vegetation patches in staggered arrays (Tanaka, 2009).

II.1.4 Reviews of video optic imagery techniques implemented for nearshore wave dynamic research

In physical experimental setups, hydrodynamic processes of nearshore waves were frequently measured by in-situ measurement devices such as capacitive wave rods or acoustic Doppler velocimeter (ADV) probes. However, due to the instability of fluid composition and rapid variability of the wave front lines, wave measurements through such in-situ measurements often result in unreliable information. Moreover, such in-situ measurement sensors are intrusive and deployed at discrete locations. Thus, they easily induce disturbances in the natural flow or are incapable of capturing the rapid evolutions of tsunami-like extreme wave flows (e.g., Curtis et al., 2002) without costly instrumentation and repetition. On the other hand, inundation flow propagating on macro roughness construction develops a turbulent interface between the wave water front and the rough surface of the structures. As such, water front lines are readily visually discernible. With the development of high-speed cameras and various laser sources for illumination techniques, water wave research has increasingly employed digital imaging techniques to capture evolutions of breaking wave surface structures (e.g., Yeh, 1991; Rockwell et al., 2001).

Moreover, benefited by the wide coverage of recording areas both in space and time, large-scale laboratory experimental and field investigations have increasingly employed non-intrusive optic imagery techniques. The advanced photogrammetric technology developed by the Argus Research Program (e.g., Lippmann and Holman 1989; Holman and Stanley, 2007), with its capability for realizing three-dimensional, real-world scenes in two-dimensional plane images and associated image processing techniques, is of special note for its contribution to the implementation of remote sensing images for observation of nearshore wave dynamic processes.

For example, Holland et al. (1997) have developed a “two-step” photogrammetric algorithm as an advancement of the traditional photogrammetric schemes. This algorithm allows accounting for geometric variables in the camera installation (such as the camera roll, lens distortion, image centers, and scale factors) during the transformation to the images. It was employed for field investigations that quantified the large-scale, long-term morphology changes of the sand bar and wave drifter motions of the nearshore waves.

Stockdon and Holman (2000) developed remote sensing techniques for long-term (~30 days) observations of the shoreward propagation of nearshore waves. Using the time stacks of pixel intensity images collected by remotely operated cameras at selected location arrays, the wave

crests of regular waves were traced. The time stack images were analyzed to calculate the shoreward wave speed as the gradient in phase of the empirically obtained waves' spectral orthogonal function. Finally, based on the linear, shallow-water dispersion relationship, information on the wave phase speeds and wave numbers were used to infer the long-term (corresponding to the image recording period) bathymetry changes in the coastal field.

Catálan and Haller (2008) investigated the effect of nonlinearity and dispersion on wave phase speeds and directions in the surf zone. Remote sensing video data was used to trace local wave amplitude and to calculate wave phase velocities. Wave phase speed results from wave crest tracing were compared to the existing various non-linear phase speed models. The study concluded that predictions for surf zone wave phase speed could be improved when the model incorporated both non-linearity and dispersive effects.

Advancements in use of remote sensing systems and optic video imagery techniques contributed significant improvements in understanding of nearshore hydrodynamics. However, only a few laboratory studies have measured the complex overland flow dynamics associated with wave flow interactions with inland macro roughness structures. Recently, Rueben et al. (2011) implemented a high-resolution optic measurement technique in order to trace tsunami wave fronts invading urban boundaries in the inundation zone as they interacted with miniature building structures. They approved the optical measurement technique that effectively captured the propagating wave front positions on an urban plain. Based on tracing the wave front position in time during its passage through the buildings, they evaluated a 40% reduction in the inundation speed (e.g., a local variation in the position of the wave front lines in time) due to macro roughness from the building "forests" compared to the wave frontal speed passing along unimpeded areas. Bridge (2011) experimentally investigated the runup force on building elements in an idealized urban waterfront in a large-scale wave basin. By varying the number and spacing of elements, the study examined the effects of various configurations of the constructed macro roughness elements on the force generated during the tsunami wave front runup. The results found that the relative spacing of neighboring buildings could have substantial influence on the tsunami inundation forces further inland.

II.1.5 Summary of this section

In sum, experiments studying tsunami wave overflow on complex inland topography have advocated significant influence for macro roughness elements, especially sensitivity to gaps

between neighboring elements, on inundation flow dynamics and resulting runup wave impacts on the beachfront. However, the investigations presented rather qualitative measurements of the initial inundation flow kinematics; the initial inundation flow speeds were evaluated based on the temporal differences in the propagating positions of the runup front without detailed information on the flow direction. The influence of the impediment from the constructed macro roughness elements on inundation flow propagation was evaluated solely by measuring the alongshore differences in the water front positions (e.g., relative delay or acceleration of the initial runup line) around the macro roughness building elements. More quantitative information for variations in the speed and direction of the runup flows is needed with regard to the temporal and spatial distributions of the initial inundation water front positions. Moreover, flow patterns around porous macro roughness elements such as multi-cylinder elements must be more complex and distinguished from those observed around the solid (e.g., non-porous) elements. Therefore, experimental investigations employing the discontinuous, patch-type coastal vegetation must be conducted to understand the effect of spatial variability in macro roughness resistance on the dynamic evolution of the runup flow patterns with tsunami-like wave conditions. For this reason, the present experiments investigated the initial flow patterns of tsunami-like waves to reveal more quantitative details of the flow direction and speed as well as the inundation depth during the wave runup on the macro roughness cylinder patch area.

II.1.6 Objectives and outline of this chapter

The present study employed video imagery techniques in order to experimentally investigate initial inundation flow patterns around multi-cylinder patch arrays synthesizing coastal forest patches. Inundation flows from tsunami runup waves are simulated by fully developed wave bores generated after offshore (i.e., farther away from the undisturbed water line at the shore) breaking of long waves. The discrete macro roughness from the patch-type vegetation is modeled by circular cylinder bundles representing initially emergent, rigid vegetation stems (e.g., trees). While maintaining consistency in stem density within a single patch, a larger scale inhomogeneity ($\sim L_a$) of macro roughness is produced through discontinuity (open gaps) between discrete vegetation patches arranged in staggered arrays. The present study focuses on evolutions of turbulent wave front velocities during initial passages through arrays of vegetation patches planted on the inundation zone behind a sloping beach.

Due to the instability of fluid composition and variability of the wave front lines during runup wave propagation over vegetated fields, measurements of wave surface using typical in-situ measurements are ineffective. Therefore, for measurement of turbulent wave surface velocities, the present study developed a "wave front tracing method" implementing non-intrusive video imagery techniques. The wave front tracing method detects wave front lines propagating over sequences of optic images and evaluates wave front speed based on evaluation of wave propagation directions. A great portion of the present study is allocated to discussion of the development and validation of the wave front tracing methodology.

Specifically, objectives of the present investigation are:

1) to present an optic methodology that continuously traces turbulent wave fronts and evaluates spatial evolutions of the runup velocities of inundating tsunami waves; and

2) to evaluate effects of different vegetation patch configurations on flow patterns of tsunami inundation flows during initial runup of turbulent wave bores.

Section 2.2 describes the experimental setup, section 2.3 describes the methodology applied for evaluations of wave front speeds, section 2.4 presents results from the wave front velocity evaluations with various setups of vegetation patch geometry, and section 2.5 offers discussion of the study's findings.

II.2 Experimental setup

II.2.1 General layout and bathymetry of the wave basin

Experiments were carried out in the Tsunami Wave Basin (TWB) at O. H. Hinsdale Wave Research Laboratory at Oregon State. This three-dimensional wave basin is 48.8 m long, 26.5 m wide, and 2.1 m deep. This is the same site where the study of tsunami wave kinematics by Baldock et al. (2009) and the study of tsunami inundation in the macro-roughness constructed environment by Rueben et al. (2011), Bridge (2011), Park et al. (2013) were conducted. Figure II-3 shows schematics for the wave basin layout and bathymetry across the tank. The bottom topography consisted of three idealized slopes: an offshore constant depth (0.9 m below a still water level, or SWL) of about 10 m extent from the wavemaker toward the coast, followed by a 1/15 slope and then by a milder 1/30 slope. The model vegetation patches were affixed on the onshore flat section extending further landward from the 1/30 mild slope. This topography reproduces in 1/50 scale the bathymetry of Canon Beach, Seaside, OR, on the Northwest coast of the US, which is closely aligned with the Cascadian Subduction Zone in the Pacific Ocean

(USGS, 2006). While the bathymetry of the wave basin was a choice of the coincided experiment of larger scope at TWB (Cox et al., 2008), the composite beach profile, with its initially steeper front leading to a milder slope and followed by a flat landward plain, is a typical characteristic of natural beaches (Rueben et al., 2011). Note that an origin of the tank coordinate system $\hat{O}$(X,Y,Z) is defined as X = 0 at the frontal surface of the wavemaker, Y = 0 at the alongshore center of the basin, and Z = 0 at the surface of SWL. A wooden panel sidewall was installed at Y = -5.43 m in order to block the flow from the side. The total water depth H is defined as $H = h + \zeta$: h is the distance from bottom surfaces to the SWL, positive upward (i.e., negative at the floor of the inland flat section above the SWL); and ζ is free surface fluctuation from SWL, positive upward. The vegetation patches were constructed on the area from X = 32.5 m to X = 42.2 m (a length L = 9.70 m) and from Y = -5.43 m to Y = -13.3 m (a width W = 7.87 m) for the present experimental study. The sidewall was extended farther offshore past the wave breaking point, thereby allowing for minimal influence of the blunt edge on inundation flow. The water level was closely monitored to maintain the 0.9-m offshore water depth. With this initial water depth, the waves generated by the wavemaker broke on the 1/30 slope before reaching the shoreline (X = 29.5 m) and approached the vegetated area with fully developed bores on the frontal face. The concrete bed was float-finished to maintain uniform and smooth roughness (a roughness height k_s = 0.1~0.3 mm) throughout the basin floor.

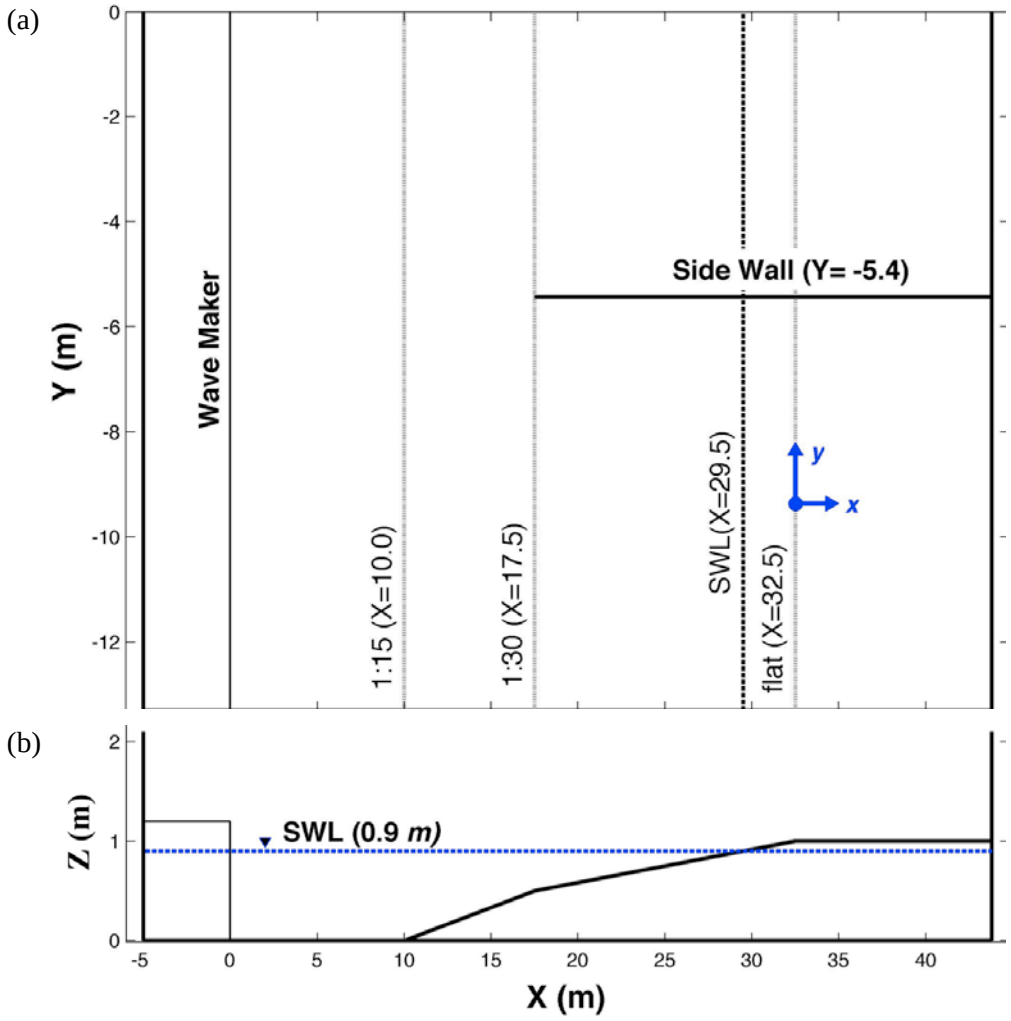

Figure II-3 Bathymetry and vegetated field layout in a three-dimensional tsunami wave basin. (a) plain view; (b) side view for a bottom profile. Axes are following a tank coordinate system.

II.2.2 Macro roughness patch configurations

In order to represent the coastal forests, the model macro-roughness forest elements were built with groups of circular cylinders. After the Indian Ocean tsunami in December 2004, active field research had been conducted on tsunami inundation sites along the coasts of Sri Lanka and Thailand. Among them, systematic field surveys and following numerical model validations by Tanaka and their research collaborators (e.g., Tanaka et al., 2007, 2009, 2011; Nandasena et al.,

2008; Thuy et al., 2010; Tanaka, 2011) have contributed to understanding and characterizing the representative coastal vegetation conditions that could efficiently counter tsunami destruction. In particular, they reported coastal vegetation characteristics that could improve the defensive functions of the coastal vegetation systems: higher stem densities; multi-row layers composed with alternate large and small species along the cross-shore direction; vertically double structures; and mixed species with complex horizontal and vertical structures due to the root and leaf. In order to characterize the representative vegetation densities and vegetation drags, Tanaka et al. (2007) employed the effective drags accounting for the vertical variations in the vegetation structures. Therefore, the cumulative drag resistances over rigid, emergent vegetation stands of a height l is modified (Nepf, 2004) as

$$\vec{F}^{*} \approx \frac{1}{2}\rho\alpha\beta(aC_D)\vec{U}|\vec{U}|l \quad . \tag{14}$$

Typically, the field values for the accumulated coefficient $\alpha\beta$ accounting for aerial structures of the stems were varied between 1.3–3.5 for the most commonly observed species (e.g., *C. equisetifolia, P. odoraratissimus*) during 3–5 m tsunamis (Tanaka, 2011). Mean spacing between close trees varied from 0 to 15 m where the higher spacing is required for the trees with a larger stem size ($d \approx 1$ m). Total drag increase with the stem density ad (defined in Eqn. 12) and sheltering effects due to the vegetation resistance was found effective when $ad \geq 0.03$ (Nepf, 2004).

In the present study, individual vegetation patches were constructed of commercial PVC cylinders with an outer diameter d = 2.70 cm and height l = 20.3 cm. The mean spacing between the adjacent cylinders was fixed consistently to be Δs = 18.9 cm, which satisfied the mean stem density $\alpha\beta ad$ = 0.02 ($\alpha\beta$ = 2 is assumed: a uniform aerial structure). This resembles the characteristic configuration of a representative tree species *P. odoraratissimus* (l = 8 m, $ad \approx 0.01$, $\alpha\beta \approx 1\sim4$) that have demonstrated effective resistances and survived against tsunami impacts (Tanaka et al., 2007). The cylinders were constructed on a staggered arrangement in order to provide effective vegetation resistances especially on the turbulent bore speeds (i.e., Takemura and Tanaka, 2007; Tanaka, 2011). Therefore, the multi-cylinder patches employed in the present experiments represent the roughness characteristics of typical coastal forests reported by various tsunami site surveys (i.e., Tanaka et al., 2007; Takemura and Tanaka, 2007; Tanaka, 2011).

For larger scale discontinuity in macro roughness, three distinct patch layouts are employed using varying patch diameters (D) and center-to-center distances between neighboring patches (ΔS). That is:

(i) Geometry1 (G1): six, "small" circular macro roughness patches of D =1.2 m with ΔS= 3.2 m;

(ii) Geometry 2 (G2): twelve, "small" circular macro roughness patches of D = 1.2 m with ΔS=2.2 m; and

(iii) Geometry 3 (G3): six, "large" circular macro roughness patches of D = 1.7 m with ΔS = 3.2 m.

The macro roughness patches were constructed on staggered arrays, and overall layout shows a symmetry with respect to the center (Y = -9.37 m) of the vegetated fields from Y = -5.43 m and Y = -13.3 m. Accordingly, a local coordinate system $O(x,y)$ is defined with respect to the vegetated fields as x = 0 at the beginning of the flat bottom vegetated field across the basin (X = 32.5 m) and y = 0 at the center of the symmetric field alongshore (Y = -9.37 m). Figure II-3 shows a definition of the local coordinate system.

Note that this present study intends to quantify local variability in speeds and directions of the bore front velocities and to investigate their correlations with the macro-roughness patch layouts. Therefore, while the single patch radius and number of employed patches were varying for distinct geometric configurations (e.g., G1~G3), the characteristic stem density within respective patches was kept constant at ad = 0.02. The ratio of the stem spacing to stem size $\Delta s/d$ = 7 (>>3) and ratios of the patch spacing to the patch size were, respectively, $\Delta S/D$ = 2.7 for G1, $\Delta S/D$ = 1.9 for G2, and $\Delta S/D$ = 1.8 for G3. These correspond to 9.1%, 18.4%, and 18.4% of planar area coverage by patches on the respective geometrical configurations. In the current staggered patch arrangements, 52%, or 20% and 23% of the alongshore widths perpendicular to the wave propagating direction, were left plainly open without porous patches for G1, G2, and G3, respectively. The present study assumed that the inhomogeneity in vegetation resistance against the incoming wave flows was induced dominantly by the large-scale ($\geq L_a = D$) discontinuity in the macro roughness between patches. Therefore it placed minimal attention on the stem scale variability of flow structures. Furthermore, the geographical scales of bottom profile and wave condition (which the next section will discuss) were determined according to the Froude similarity of the prototype beach conditions (Canon Beach, Seaside, OR). On the other hand, the configurations of individual stems and patch layouts were determined by the

typical characteristics of coastal forests based on literature reviews of various tsunami site surveys. Therefore, no similarity parameters were used to design the vegetation patch configurations. Figure II-4 shows the patch arrangements on the onshore flat section. The vegetation patch layouts are designed symmetric with respect to the centerline y = 0. The patch positions are referred to by the row (parallel to the shoreline) number ascending with x position. For example, P1 refers to the patches x = 1.5 m on three geometries. Table II-1 summarizes positions and names of patches according to the local coordinates and row numbers, respectively.

II.2.3 Instrumentation layout

For this study, a larger scale optic measurement was made by a down-looking web video camera mounted on the ceiling of TWB. Image recording was made to capture the surface flow structures during the initial phase of tsunami wave inundation. Figure II-4 shows the field of view (FOV) of the respective images that were cropped to focus on the vegetated fields on the landward flat section (see Figure II-3). The raw images from the video recordings were rectified in reference to a still water level (0.9 m). The images were recorded at an average frame rate of 15 Hz and the final image data, as input for the analysis of this present study, has a spatial resolution of 2 cm/pixel. Additionally, the supplementary in-situ measurements for the velocity and inundation depth were made using ADV (ADV3 and ADV4) and ultrasonic wave surface elevation gauges (WG5 and WG6), respectively. On each configuration, the co-located gauges were installed at four fixed points (marked in Figure II-4) to supplement the video image analysis.

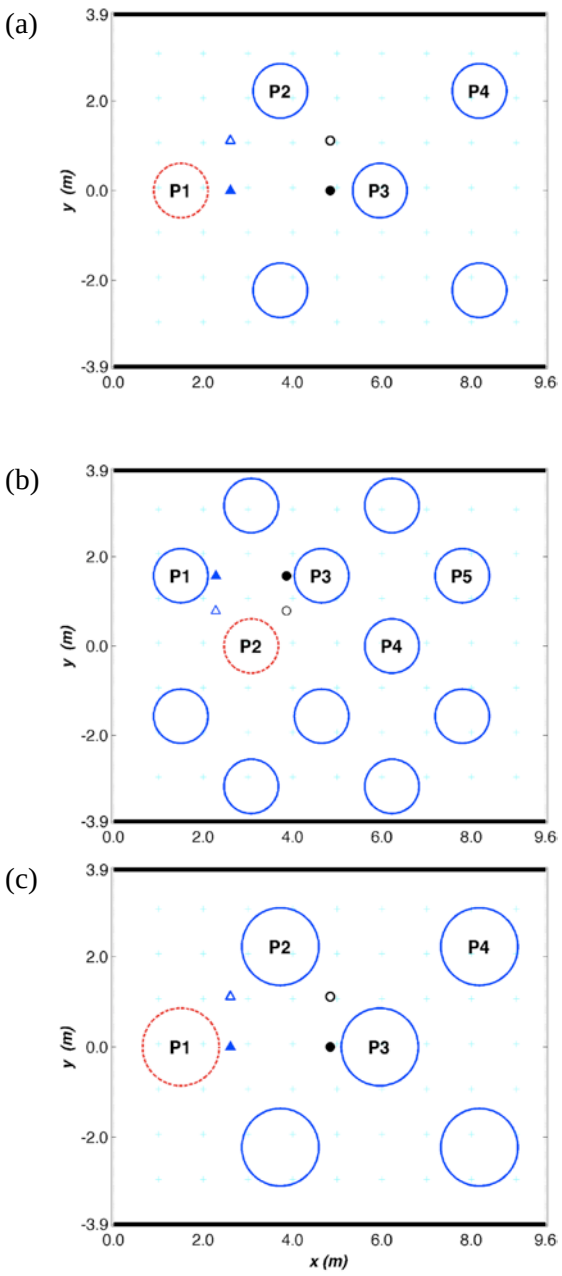

Figure II-4 Vegetation patch layouts. (a) G1 consisting of six, small patches; each patch has a diameter *D* = 1.2 m, (b) G2 consisting of twelve, small patches; each patch has a diameter *D* = 1.2 m, and (c) G3 consisting of six, large patches; each patch has a diameter *D* = 1.7 m. The measurements points of co-located ADV and WG are marked with: △, the measurement location A; ◯, the measurement location B (see Table II-2); 'hollow', measurements from ADV3 & WG5 along the channel, 'solid', measurements from ADV4 & WG6 along the patch. P1~P4 for G1 and G3 and P1~P5 defines the "row" numbers for patch arrangements. Reference patches are marked with dashed lines (red) for each configuration. The axis along both directions are defined according to the local coordinate system.

Table II-1. Vegetation patch arrangements. Reference patches are weighted with "bold" for each geometry.

Geometry	Rows	Locations	
		x (m)	*y* (m)
1,3	**P1**	**1.50**	**0.00**
1,3	P2	3.73	-2.22
1,3		3.73	2.23
1,3	P3	5.95	0.00
1,3	P5	8.18	-2.22
1,3		8.18	2.23
2	P1	1.50	1.58
2		1.50	-1.57
2		3.07	3.15
2	**P2**	**3.07**	**0.00**
2		3.07	-3.14
2	P3	4.65	1.58
2		4.65	-1.57
2		6.22	3.15
2	P4	6.22	0.00
2		6.22	-3.14
2	P5	7.80	1.58
2		7.80	-1.57

The locations of the co-located ADV-WG instruments and the physical locations of the vegetation patches are summarized in Table II-2 according to the local coordinate system. In order to preserve natural flow conditions, these point measurement instruments were installed only when the data collection for the video imagery was not being pursued. Both measurements collected data with 50 Hz of a regular sampling rate. For each geometry, the sensors for both ADV and WG were installed at four different measurement points (two different x and y locations, respectively). Figure II-4 shows the measurements points respective of different vegetation patch configurations, including that on a control field (i.e. no patch, plain fields).

Table II-2 Measurement locations for ADV and WG

ADV3A, WG5	1,3	2.61	1.08
ADV4A, WG6	1,3	2.61	-0.04
ADV3B, WG5	1,3	4.84	1.08
ADV4B, WG6	1,3	4.84	-0.04
ADV3C, WG5	2	2.29	1.08
ADV4C, WG6	2	2.29	-0.04
ADV3D, WG5	2	3.87	1.08
ADV4D, WG6	2	3.87	-0.04
ADV3A, WG5	n/a	2.61	1.08
ADV4A, WG6	n/a	2.61	-0.04
ADV3B, WG5	n/a	4.84	1.08
ADV4B, WG6	n/a	4.84	-0.04

II.2.4 Wave conditions

Tsunami-like long waves were generated by a piston-type wavemaker with a capacity of making 2.1 m maximum displacement with 2.0 m/s of maximum speed. In order to simulate turbulent inundation flows from breaking tsunami waves, the present study employed a single pulsed, stroke wave. An impulse signal for the wavemaker was constructed by an error function that forced the wavemaker to make the 2.0 m full stroke for duration of 7 seconds. Such a 7-s "full stroke" (hereafter, a "7s wave") resulted in a single crested, positive surge wave in which nominal distance to an elevated crest was 0.28 m from SWL near the wavemaker offshore. Figure II-5a shows time histories of a paddle displacement of the wavemaker and a resulting positive surge wave. Note that the present study employed the "full stroke" waves rather than the solitary waves that are often applied for hydraulic modeling of tsunami waves. The 7-s "full stroke" wave produced an elevation of the wave crest in which initial water depth was 7 cm above the onshore flat bottom. It resulted in a runup flow of about a 6-second-period (duration from the time the wave front enters the flat section at X = 32.5 m until it reaches the onshore

ending boundary at X = 42.2 m), according to the image recording from the web-camera. Madsen et al. (2008) discussed the geophysical length (time) scale required for offshore tsunami waves to develop into an undular bore on coastal surf zones and remarked that is unlikely to be replicated in typical laboratory-scale long wave simulations. Therefore they discredited implementing the solitary waves (Goring, 1978) for laboratory scale simulations of tsunami wave runup. Furthermore, they have emphasized that it would be misleading to focus on the short waves for which the impacting time scale is merely t^* = 10–15 s, whereas the time scale of flooding due to the following main tsunami is much longer, at t^* = 15–30 min. Appreciating the assertion raised by Madsen et al., the present study favored the stroke wave based on the error functions, as it can produce longer-period wave inundations compared to those produced from a solitary wave with the same wave height (Rueben et al., 2011). This "full stroke" wave readily renders adjustments for horizontal and vertical extents of long-wave inundations and the breaking points that largely affect inland flow structures. Furthermore, it should be noted that this study investigates the interactions between vegetated macro roughness and tsunami main inundation flow. Therefore, this study emphasizes and accounts for the contributions of broken wave impacts and consequential turbulent energy dissipation mechanisms as they promote variability in inundation flow patterns during the wave front runup. However, no attempt was made to evaluate the impacts of wave breaking solely or short waves resulting from long wave dispersion.

Figure II-5b shows the inundation water depth time histories at measurements locations A and B, respectively, from WG6. The 7s stroke produced a long wave propagating for about 50 seconds from its incipience until arrival of the wave front at the end of the vegetated flat section; the duration of runup and withdrawal over the vegetated landward flat section was nearly 15 seconds. These are respectively equivalent to 5.9 minutes of propagation and 1.8 minutes of initial inundation period at a prototype scale. Admittedly they are shorter than the time scale of the typical tsunami runup events (Madsen et al., 2008; also see Rueben et al., 2011). However, this study intends mainly to observe the initial impacts from the turbulent tsunami bore front rushing inland and focuses on the functionality of the beachfront vegetation roughness as a frontal defensive mechanism. Therefore, in spite of the smaller time scale, the present experimental setup seemed to provide a sufficiently long period (or distance) for the 7s wave to break at a desired position and to develop the turbulent bore structures in the frontal faces (Baldock et al., 2009; Rueben et al., 2011). Finally, the inundation water depth defined as the

highest crest level at the front, above the surface of the flat inland section floor, was initially ζ = 0.07 m at X = 35.1 m; that has been decreased to ζ = 0.05 m at X = 37.3 m (29% decrease over 2.2 m distance).

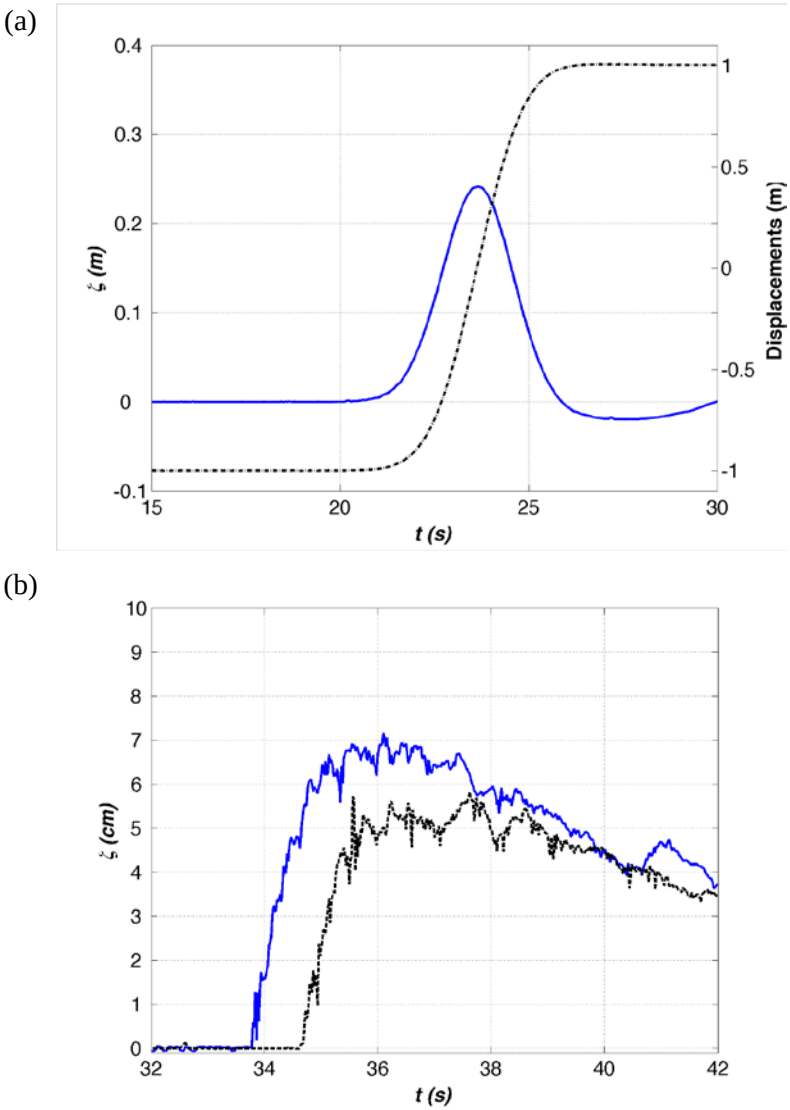

Figure II-5 Wave elevation time histories. (a) An initial shape of the 7s-wave on offshore near the wavemeker (solid) generated by the 2.0 m full stroke displacement of the wavemeker paddles (dashed); the wavemaker was forced by the input signal generated by the 7 second error function, (b) time histories of inundation water levels ζ from running up wave flows on the inland flat section; ζ are the inundation water depth above the bottom surface measured from WG6 (solid) and ADV4B (broken), respectively.

II.3 Methodology: development of a “wave front tracing method” for evaluation of wave frontal velocities

II.3.1 Development of wave front lines

Image processing

The raw images (RGB color models) were first rectified, cropped, and re-oriented (A. Ryan, personal communication). The resulting images are in a format displaying the wave propagation from left to right, defining a positive *x* direction. The field of view (FOV) of the resulting images is narrowly focused on the vegetation patch area within a virtual rectangle bounded by the northwest corner (X = 29.42 m, Y = -5.60 m) to the southeast corner (X = 42.20 m, Y = -13.22 m). This includes the entire area of the onshore flat section and a marginal area offshoreward on the 1/50 sloping beach. The spatial resolution of the pre-processed images was 2 cm/pixel, and the average frame rate of the image recording was 15 Hz. The input images were first selected to essentially capture the wave runup phases: the time between when the wave front first reached the flat inundation area until just before it reflected back from the shore boundary. This initial runup event normally occurred for about 6 seconds over approximately 40 frames from the first appearance of the wave front at X = 29.42 m. A MATLAB code script was written to automatically detect and mark a time stamp when the wave front first crossed the left boundary of FOV at X = 29.42 m (t = 0) and then to extract from the 40 frames.

Wave front detection

During interaction between the propagating wave front and the macro-roughness (either due to bottom friction or from vegetation patches), the water surface developed white water along the wave front. The air bubbles mixed beneath the water surface increase the reflection and scattering of light that, in turn, increases the dynamic intensity at a pixel point in the images. Consequently, the dynamic wave fronts running onto an initially dry (e.g., motionless) beach become traceable based on the gray scale intensity changes. On the other hand, there are some minute motions irrelevant to the dynamic intensity of wave fronts that hinder the accuracy of wave front detection. The causes for these minute motions are:

(1) background noise related to either image clarity or lighting wave frequency from natural or artificial lighting;

(2) uncontrollable bright spots on the basin floor (e.g., sunlight from a distant window);

(3) dynamic features (e.g., an uneven water surface, turbulent air plumes floating on the surface) of the main inundating flow behind the wave front that increase light scattering; and, most significantly

(4) the painted grid stripes on the floor that, when subtracted from each instantaneous image, result in exaggerations of the dynamic intensities due to subtle motions far from the wave fronts.

Accordingly, the process for detecting and developing the wave front lines was carried out by first isolating the dynamic features due to wave front kinematics from that of other sources. The background noise or clumps of light reflection are sources of errors (1 and 2) that clearly appear on the overall image; hence, they are readily quantifiable. That is, the errors due to the sources (1) and (2) could be removed by subtracting a mean image from the instantaneous images. The mean images were produced for each test by time-averaging of the first 15 frames of instantaneous images; therefore, the mean image represents a steady condition of the FOV for a test, such as brightness, background noise, and intensities on highlighted areas and grid marks on the basin floor. Consequentially, the image remaining after subtracting the mean image (namely, instant images) demonstrates only the dynamic features relevant to inundation.

Figure II-6 shows the instant images showing dynamic features at the 35^{th}, 50^{th}, and 65^{th} frames, respectively. Note that the images effectively denote the inundating water in motion, and substantial intensity gradients are observed across the frontal edges. Therefore, lines of wave frontal edges were detected based on the intensity variations that sharply increase across the wave front. As the intensity gradients are more vividly displayed when the images were converted to black and white, binary images, the conversion from gray scale images to binary images (Figure II-7) was performed using a MATLAB built-in function that calculates the threshold value for conversions based on the Otsu method (Otsu, 1979).

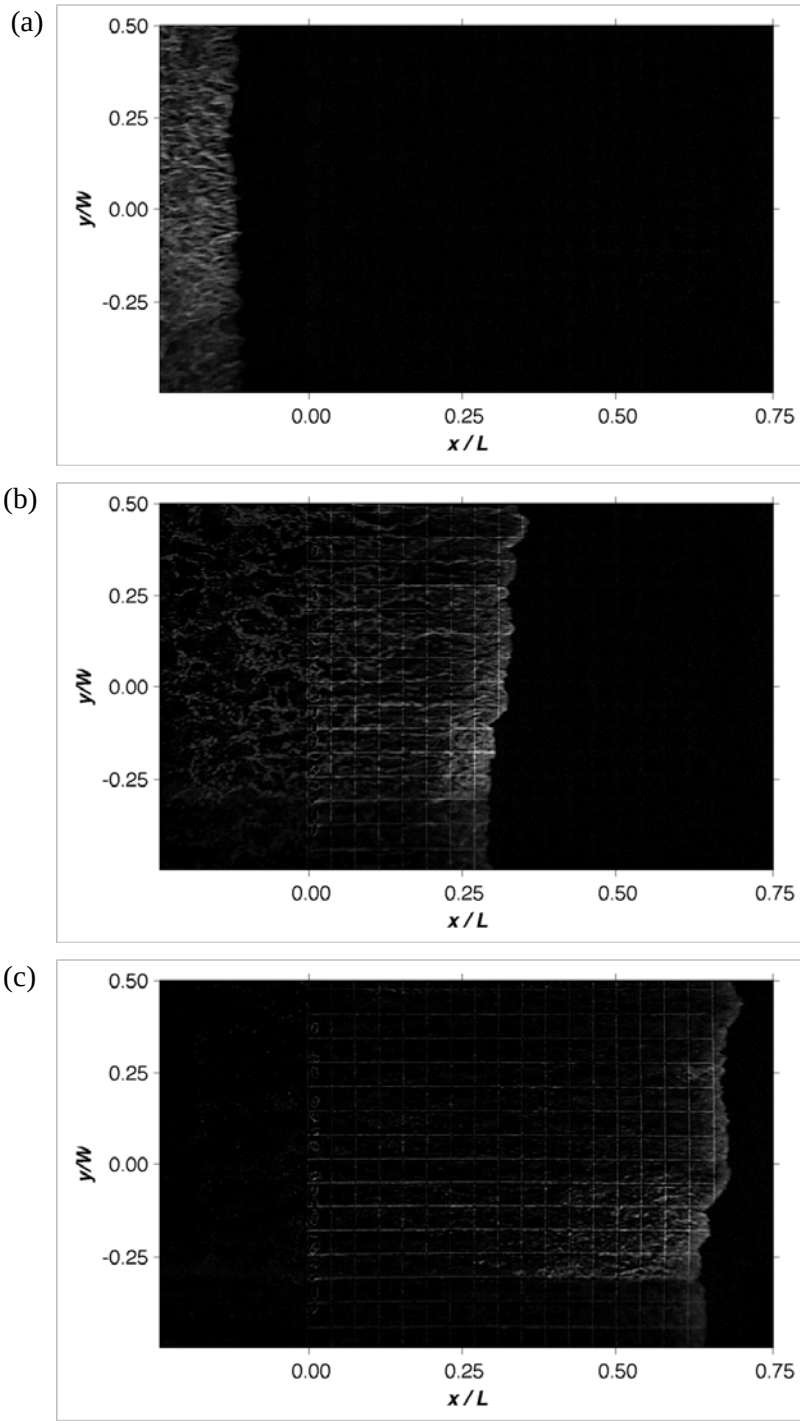

Figure II-6 Instant images displaying the wave front intensities. The instant images are obtained after subtracting the mean image from the raw images from (a) 35th, (b) 50th, and (c) 65th frames. The horizontal and vertical axes indicate x/L and y/W, respectively, where L is the length of FOV and W is the width of FOV.

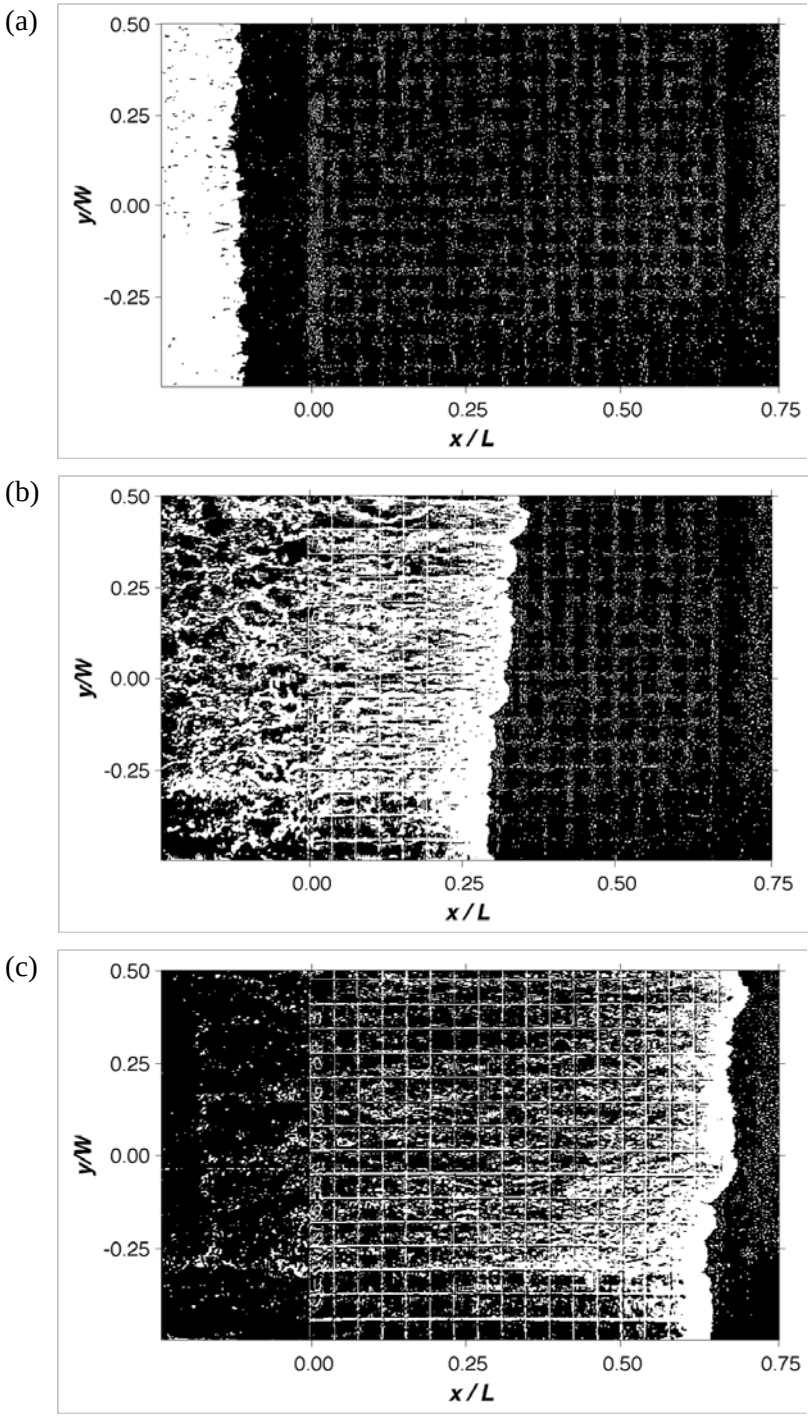

Figure II-7 Binary images obtained converted from the gray scale, instant images. Dynamic features on the wave surface are represented with a white color. (a) 35th, (b) 50th, and (c) 65th frames. The horizontal and vertical axes indicate x/L and y/W, respectively, where *L* is the length of FOV and *W* is the width of FOV.

Next, the binary images were further processed to get rid of the spurious spots that were irrelevant to the wave motion, thus could lead to unrealistically large deviation in the wave front positions at a time instant by employing masking images. First, the white spots in the dry regions detected prior to the wave front reached at the grid line positions (listed as source of error 4) were removed by applying dynamic black masking images that decreased in size (a cross-shore extension) as the wave propagated in time. That is, those white spots were covered by the dynamic black masking images (turning the white spots of value "1" into a value "0" in the binary files) and taken out of consideration during determinations of the wave front. On the other hand, the black spots behind the wave frontal edges (due to error source 3) were covered with white masking images, turning any black spots behind the wave front position (i.e., on the left side of the maximum x position detected as the wave front) into a value "1". As a result, the majority of spurious points deviating from the general frontal line were eliminated and the wave front positions could be continuously delineated.

However, rarely, the pixel intensities of the actual wave front were indiscernibly weak as the water depth became much shallower near the rear end of the flat section. The wave front positions determined through the previous processes were reexamined to check feasibility of the alongshore variations. That is, by examining the rates of changes in x_i between neighboring points in y (e.g., $y_{j-1} \sim y_{j+1}$, where j denotes a j^{th} point along the y axis), the points where the alongshore rate of variation d^2x_i/d^2y_j exceeded 3.5 times the standard deviation of d^2x_i/d^2y_j were removed and replaced based on linear interpolation (marked with circles in each plot in Figure II-8). Finally, the plots in Figure II-9 show examples of resulting wave front positions respectively from the 35^{th}, 50^{th}, and 65^{th} frames during wave propagation.

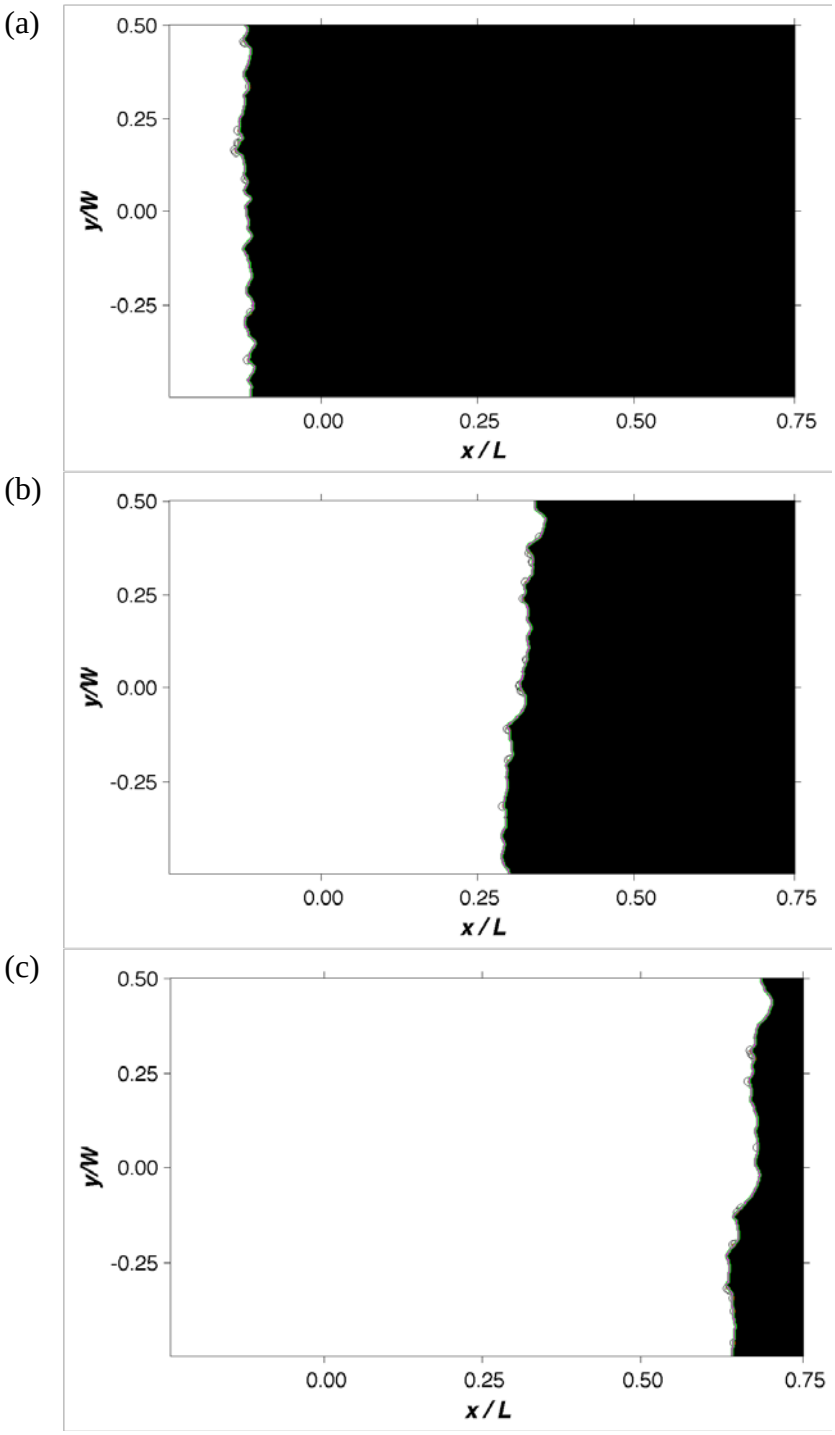

Figure II-8 Masking images delineating the water front positions. 'O' marks the wave front positions modified by a linear interpolation when d^2x/dy^2 exceeded the specified threshold limit. (a) 35th, (b) 50th, and (c) 65th frames. The horizontal and vertical axes indicate x/L and y/W, respectively, where *L* is the length of FOV and *W* is the width of FOV.

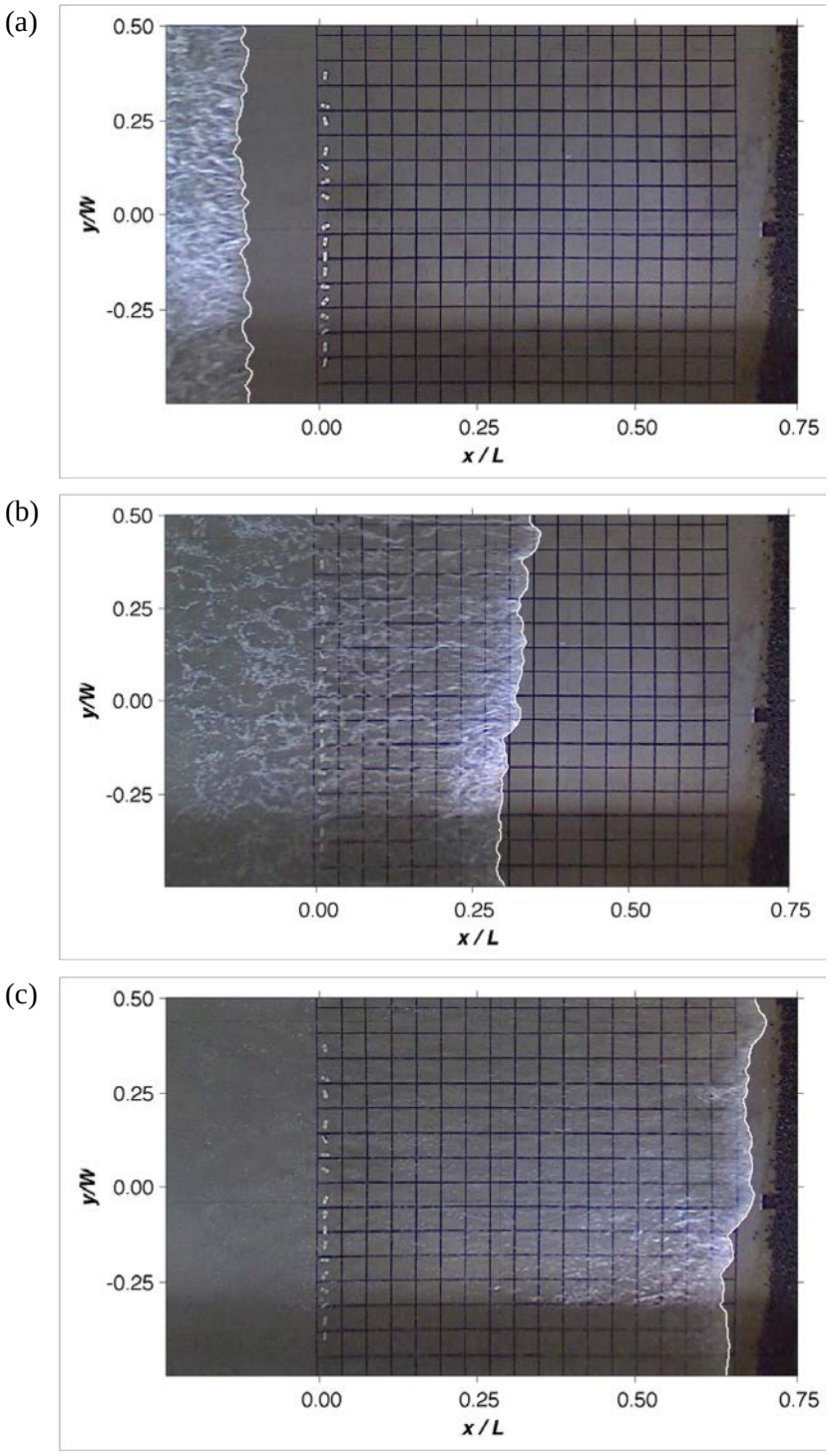

Figure II-9 Final wave front lines at the instantaneous wave front positions. (a) 35th, (b) 50th, and (c) 65th frames. The horizontal and vertical axes indicate x/L and y/W, respectively, where *L* is the length of FOV and *W* is the width of FOV.

II.3.2 Interpolations of wave front lines

Figure II-10a shows wave frontal positions derived from turbulent bore front locations from a single, arbitrarily selected test. In Figure II-10b, frontal lines from 5 repeated tests are plotted together to comparatively display the frontal positions appearing in about 40 frames (~ 6 seconds) during the wave runup.

While effectively depicting temporal distributions of wave fronts marching in time, it contains minute fluctuations along the lines of wave fronts. These minute fluctuations were identified as frequent oscillations in the x position up to $\partial x \approx 15$ pixels over fairly regular spatial intervals along the y direction of $\partial y \approx 25$ pixels, hence $\partial x / \partial y \approx 0.6$. It is unclear why those minute fluctuations occurred with $\partial y \approx 25$ pixels of spatial repeatability. However $\partial y \approx 25$ pixels are close to the distance between the grid stripes on the floor. Therefore, it is presumed that the painted grid stripes on the basin floor may have produced minute irregularity in the bottom friction that affected the propagations of the initially thin wave bore front. It is likely a realistic pattern being observed from the actual wave fronts—we are tracking the turbulent bore fronts. These minute fluctuations must result partially due to the turbulent nature of the wave frontal phase and also due to irregularity in the roughness of the bottom surface. However, such subtle variations often resulted in significant deviations in the slopes of the wave front that, consequently, led to miscalculations of the propagation velocities of the dominant inundation flows following just behind the turbulent wave front. On the other hand, such variations in the wave front velocities over the narrow y extent must be not the product of either momentum flux of the dominant inundation flow or the activities between the wave and macro roughness patches. Hence, small-scale fluctuations along the wave frontal lines were smoothed out by performing a kernel smoothing regression. The kernel smoothing regression assumes normal distributions of the data within subrogation areas (e.g., with respect to a mean position of wave fronts within the subrogation) and automatically computes kernel probability density functions and optimal bandwidths. The minute oscillations within a subrogation window (the window size of 25 by 25 pixels^2 ≈ 50 by 50 cm^2 was used) could be removed from the preliminary frontal lines and replaced with alternative points determined by the least square regression. The mean deviation of the preliminary wave frontal positions from the smoothed lines was 1.3 cm. Therefore, the resulting wave frontal lines shows the alongshore distributions of the wave front

excluding the small scale turbulent effects (e.g., due to the irregularity of the turbulent front face or non-uniformity of bottom surface).

On the other hand, the camera device used for present image recordings had irregular shooting rates (an average frame rate of 15 Hz). Consequently, the image data and the wave frontal lines derived from the images were obtained at irregular time intervals. Therefore, the information on the wave front positions from available time instances were interpolated in time and reproduced at a regular time interval of Δt = 0.05 *s*. As a result, the final wave frontal lines show temporal evolutions of initial wave propagations consistently for different tests.

Figure II-10c shows an example of the wave frontal lines after smoothing (thin, red lines) drawn over initially unsmoothed lines (thicker, yellow lines). Figure II-10d shows the finally determined wave frontal lines after interpolation (dashed).

It is worth noting that the mean positions of the wave front seem fairly uniform in the beginning until the wave reaches the flat sections (x<0). In the following area, the wave fronts tend to propagate faster at y > -0.1*W*, while becoming more smooth alongshore (less turbulent). The surface of the inundating flat section was finished with a fine cement coating for a smooth surface profile. In addition, the floor was maintained as a dry surface by wiping off the water flooding the inland flat section prior to each wave operation. In spite of this, admittedly there appeared inhomogeneity of the bottom surface roughness that resulted in relatively slower propagation of the flow on the lower portion (y < -0.1*W*) of the studied area. The maximum variation of wave front speeds due to different bottom surface conditions along the y axis was estimated approximately as $\partial x/\partial y = 0.4$, between -0.11*W* < y < -0.02*W* (-0.80 m < y < -0.15 m). The influence of the bottom inhomogeneity and temporal interpolations on velocity calculations will be discussed later in conjunction with the inundation velocity variability.

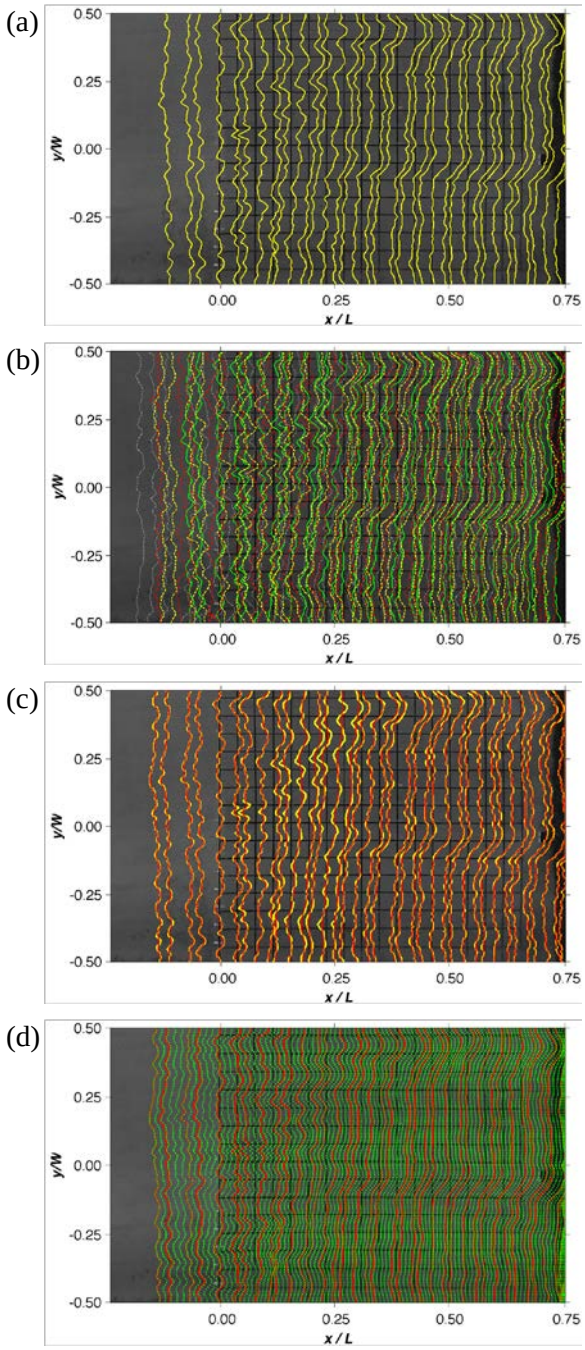

Figure II-10 Wave front lines. (a) An example of instantaneous wave frontal lines determined based on wave front positions appearing in images over 35 frames (~ 6 seconds), (b) instantaneous wave frontal lines from total 5 repeated runs, (c) wave frontal lines after smoothing, and (d) final wave front lines regularly interpolated with a time interval dt = 0.05 *s*. The horizontal and vertical axes indicate x/L and y/W, respectively, where *L* is the length of FOV and *W* is the width of FOV.

In summary, the wave front lines were determined with a regular time interval Δt = 0.05 *s* through the process of the wave front position detection, and regular deployment has resulted. The wave front positions were initially detected based on the turbulent wave front lines visible in the instantaneous raw images. However, it must be noted that the final wave front lines were obtained after the post-process that eliminated and smoothed out the minute fluctuations in the wave front positions that were presumed be the product of the turbulent frontal phase (e.g.., the spatial frequency rate $\partial x/\partial y \approx 0.6$). Therefore, the following procedures evaluating the wave front velocities are pursued based on the final wave front lines representing the initial water lines of the runup flow. Hence, the wave front velocities evaluated while tracing the wave front lines are assumed to be associated with the maximum inundation depth and variations in the patch scale flow velocities during the initial wave runup. Furthermore, these wave front lines determined during the process hereby described represent the spatial and temporal propagations of the wave front in terms of x, y, and t. Therefore, this present study defined the resulting wave front lines as a function of x, y, and t, denoted as the "*wave front function*" $\Omega = \Omega(x, y, t)$.

II.3.3 Wave frontal velocities based on the "wave front tracing" method

Principles of a "wave front tracing method"

As introduced earlier, this study focuses on the propagation of the initial inundation flow of long waves generated by a single pulsed, long wave breaking (e.g., infinite period, turbulent wave surfaces) over the inland macro-roughness vegetated area. In this section, the wave front velocities are evaluated based on the wave front function $\Omega = \Omega(x, y, t)$ determined during the long-wave runup on the inundation area behind the surf zone. That is, the mean streamlines along which the wave front propagates are calculated as lines orthogonal to the wave frontal slopes at various alongshore positions. Therefore, in the present two-dimensional, incompressible wave flow fields, the scalar wave front functions $\Omega = \Omega(x, y, t)$ are used to derive a normal directional vector $\vec{N}$ (Dean and Dalrymple, 1991) as

$$\vec{N} = \nabla\Omega = n\left|\nabla_h \Omega\right| \tag{15}$$

where, *n* is a normal unit vector perpendicular to the scalar wave front function Ω (positive outwards) and ∇_h is a horizontal gradient operator $\nabla_h = \frac{\partial}{\partial x} i + \frac{\partial}{\partial y} j$. Consequently, ∇_h,

hence $\vec{N}$, points to the direction of the greatest gradients of $\Omega = \Omega(x, y, t)$, which is the direction of wave propagation. Note that the x direction is positive toward the onshore normal and y direction is parallel to the alongshore. Accordingly, the wave propagation line $\vec{s}$ along which the initial wave front travels can be determined as

$$\vec{s} = s(x, y, t) = N_x i + N_y j = |N| \cos\theta i + |N| \sin\theta j \quad (16)$$

Here, θ is the incidence angle made between the wave propagation line and shore-normal (i.e., the right x direction) defined as $\theta = \cos^{-1}\left(N_y / N_x\right)$. Figure II-11 shows the definition schematics. Note that the present study assumes long waves of an infinite period (T ≈ ∞, $\sigma \approx 0$) approaching an initially quiescent, dry inundation zone. Thus, the contribution from the frequency dispersion to reduction of the wave propagating speed was unnecessary (e.g., no flow speed in a counter direction), hence omitted from consideration.

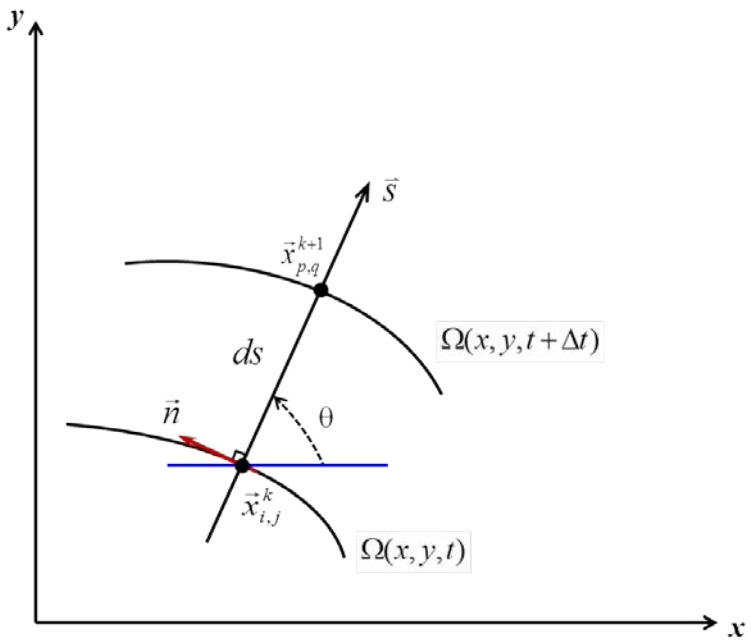

Figure II-11 Schematic diagram defining the wave front position Ω and wave propagation $\vec{s}$.

Finally, the wave phase speed C propagating along with the wave propagation line s and local velocity components u and v in respective x and y directions is calculated as

$$C = \frac{ds}{dt}, C\cos\theta = \frac{dx}{dt} = u, C = \frac{dy}{dt} = v \quad . \tag{17}$$

Figure II-12a shows an example of instantaneous wave front lines $\Omega(x, y, t)$ plotted at a time interval Δt = 0.05 *s* for about 35 time steps. Figure II-12b is a closeup view of Figure II-12a (boxed area) to demonstrate the procedures developing the wave front velocity fields. The wave propagation lines (solid lines) are determined by calculating the normal directional vector $\vec{N}$ orthogonal to the slopes of the wave fronts (broken lines) from any point along the wave front $\vec{x}_{i,j}^{k} = \Omega(x_i, y_j, t_k)$ at (x_i,y_j)—denoted with a triangle in Figure II-12b. The wave front slopes were determined by the least square fit line between three adjacent points in x and y, respectively, $x_{i-1} \sim x_{i+1}$ and $y_{i-1} \sim y_{i+1}$ at $t = t_k$. Here, the subscripts i and j are the location index for the selected positions in x and y, respectively, and subscripts k are the timing index denoting the start of the orthogonal line at t = t_k. The wave propagation line is then determined as an orthogonal line starting from $\vec{x}_{i,j}^{k}$ at the wave front and propagating with an angle θ with respect to shore-normal direction.

Next, the wave propagation line at t = t_k is extended to reach the next wave front line (i.e., wave front positions derived at t = t_{k+1}). The conjunction point $\vec{x}_{p,q}^{k+1}$ ('×' in Figure II-12b) where the orthogonal line from t = t_k penetrates to the wave frontal line at t = t_{k+1} is determined. Here, the subscripts p and q are indexes for x and y, respectively, along the wave front line determined at t = t_{k+1}. Finally, the wave propagating velocity $\vec{C}_{i,j}^{k} = (u_i, v_i)^k$ is calculated based on the Eqn. (17), where the passage of the wave front between the consecutive time steps during $dt \approx \Delta t$ is calculated as $|ds| \approx \vec{x}_{i,j}^{k} \vec{x}_{p,q}^{k+1} = \sqrt{\Delta x^2 + \Delta y^2}$. Accordingly, the wave front velocities were calculated based on Eqn. (17), which evaluated each velocity component as

$$u_{i,j}^{k} = \frac{\Delta s\cos\theta}{\Delta t}, v_{i,j}^{k} = \frac{\Delta s\sin\theta}{\Delta t} \quad . \tag{18}$$

The present method becomes advantageous by rendering full-field evaluations of the wave propagating velocities where the wave front function $\Omega(x, y, t)$ is defined. The following sections demonstrate and validate the present wave front tracing method.

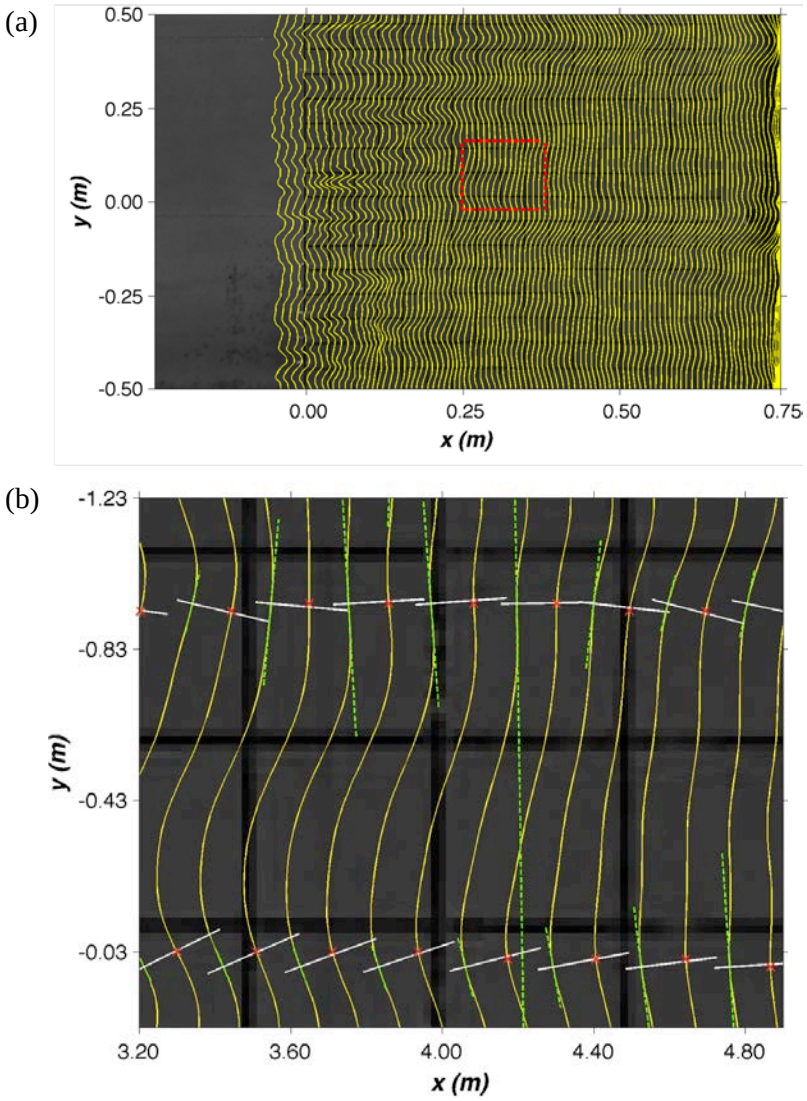

Figure II-12 Developments of wave front velocities using the "wave front tracing method". (a) An example of the instantaneous wave front lines defining the wave front function $\Omega(x,y,t)$; the frontal lines are evaluated at a regular time interval Δt = 0.05 *s* for about 35 time steps, (b) a close up view of (a) to demonstrate the propagating velocity evaluations by the wave front tracing method developments; wave propagating directions (solid) are orthogonal to the instant wave front slopes (broken) at $\vec{x}_{i,j}^{k}$; the orthogonal lines are extended from at $\vec{x}_{i,j}^{k}$ to the conjunction points $\vec{x}_{p,q}^{k+1}$ ('×') in the wave front points at the next time step. Note that both the wave front lines and orthogonal propagation lines are plotted at Δt = 0.10.

Validation: comparisons to the wave front velocities from analytical solutions

In order to demonstrate and validate the wave front tracing methodology, propagating velocities of idealized wave fronts are evaluated both analytically and by the wave front tracing method. First, propagating wave front lines were generated based on a cosine function as:

$$\Omega(x, y, t) = x - pt\left[\cos(\lambda y) - q\right] \quad (19)$$

Here,

- x is the wave front position in the propagating direction at the alongshore position y (e.g., x and y are both in centimeters) at time *t* (*s*);
- $\lambda = 2\pi/l_y$, where l_y is the alongshore extent of y; and
- *p, q,* and λ are arbitrary coefficients that are positive for the waves propagating from left to right in the images.

In this study, $0 \le y \le 400$ cm (l_y = 400 c*m*) , *p* = 16 c*m/s*, and *q* = 1.2 c*m*.

Figure II-13a shows the wave front lines determined from Eqn. (19) using a time interval Δt = 0.6 *s*, where the spatial difference between neighboring x and y nodal points (i.e., a distance between the closest velocity output positions) was both 1 cm (e.g., ∂y_i or ∂x_i = 1 c*m*/*pixel*). The wave front tracing method was applied to evaluate the wave front velocities based on the slopes of the wave front lines shown in the images. Figure II-13b is a close-up of Figure II-13a, showing the slopes of wave fronts (green) and the orthogonal lines (blue) indicating the direction of wave front propagation. The wave front lines started from $\vec{x}_{i,j}^{\,k}$ (' $\triangle$ ' in Figure II-13b) at a time step t = t^k and were extended toward the wave front lines determined at the next time step t = t^{k+1}. The conjunction points $\vec{x}_{p,q}^{\,k+1}$ (' $\times$ ' in Figure II-13b) among the wave front locations at t = t^{k+1} were selected as locations where the water front that started from $\vec{x}_{i,j}^{\,k}$ was reached after Δt = 0.6 s of traveling along the respective orthogonal lines. Finally, the wave front velocities were calculated based on Eqn. (18).

The resulting velocity vectors are presented in Figure II-13a at selected locations along y = 20 cm, 50 cm, 80 cm, 110 cm, 140 cm, 170 m, and 200 m. As the wave front function is defined in terms of x, y, and t by Eqn. (19), it renders explicit solutions for the wave front velocities based on Eqn. (15)-(18). Accordingly, the wave front velocities $\left\{n\frac{dy}{dx}\right\}_{anal}$ obtained by taking spatial derivatives of the function (19) were analytically calculated. Therefore, the comparisons

of $\left\{n\frac{dy}{dx}\right\}_{anal}$ to the rates of wave front propagations $\left\{n\frac{\Delta y}{\Delta x}\right\}_{s}$ evaluated by the wave front tracing method provide a means to estimate uncertainties in the velocities evaluated from the wave front tracing method.

Figure II-13c shows time series of the velocity ratio $\left\{n\frac{\Delta y}{\Delta x}\right\}_{s}\Big/\left\{n\frac{dy}{dx}\right\}_{anal}$ at selected locations along y = 20 cm, 50 cm, 80 cm, 110 cm, 140 cm, 170 cm, and 200 cm. Note the function defined by Eqn, (19) specified the wave front lines symmetric with respect to y = 200 cm. Therefore, the velocity ratios at the alongshore centerline y > 200 cm are identical to those at y < 200 cm, while the signs of *dy/dt* are opposite to their counterparts.

As shown in Figure II-13c, the velocity ratios remain within 3% of difference over 9 seconds (16 time steps) of propagation time. The accuracy of the velocities from the wave front tracing method are dependent on a pixel ratio that determines the number of node points used for depicting a unit length of the wave front line in the images. In Figure II-13, a length-to-pixel ratio (i.e., typically a resolution of image) of 1 cm/pix was employed. As a result, the standard deviation in the velocity ratio (Figure II-13c) was estimated as 2.7% for the overall time series. With an order one decrease in the pixel resolution (10 cm/pix), the standard deviation in velocity ratio increased to 7.5%, largely during early time steps t < 3 s. This is where the changes in the propagating direction were relatively small (Δs< 20 cm), hence requiring confined resolutions. Therefore, the wave front tracing method that estimated the wave front velocities based on the wave frontal positions detected from images with the pixel resolution of *O*(1 cm/pix) must allow approximately 3% of uncertainty. This could be interpreted as the error incurred while approximating the wave front direction according to the wave front positions represented in the images depicted with the pre-determined image resolution *O*(1 cm/pix).

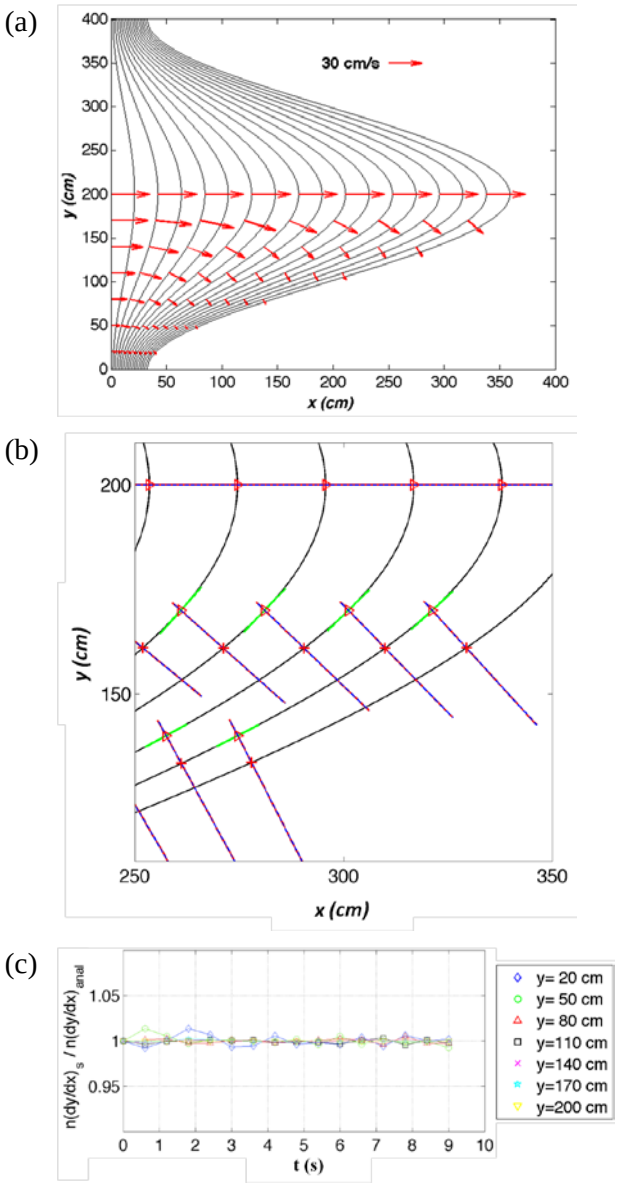

Figure II-13 Wave front velocities determined by a mathematical function. Wave front lines $\Omega(x,y,t)$ are generated by the cosine function defined as $\Omega(x,y,t) = x - pt\left[\cos(\lambda y) - q\right]$; 0≤y≤400 in centimeters, where *p* = 16 cm/s, *q* = 1.2 cm, λ = $2\pi/l_y$, where l_y = 400 cm with a time interval Δt = 0.6 s. (a) Velocity vectors at selected locations along y = 20 cm, 50 cm, 80 cm, 110 cm, 140 cm, 170 cm, and 200 cm; velocity vectors are plotted at every 2Δ = *1.2 s*, (b) a close-up of (a) showing the slopes of wave fronts (green) and orthogonal lines (blue) indicating directions of the wave front propagation, and (c) time series of the velocity ratio $\left\{n\frac{\Delta y}{\Delta x}\right\}_s \Big/ \left\{n\frac{dy}{dx}\right\}_{anal}$ over the wave propagation time *t* at the locations specified in (a).

Next, errors that may have occurred due to uncertainties in interpolated wave front positions were examined. Figure II-14 shows wave front lines interpolated from the position function defined in Figure II-13. The original wave front position function determined by a cosine function with a time interval $\Delta t = 0.6$ s is interpolated with shorter time intervals $\Delta t = 0.4$ s and $\Delta t = 0.2$ s for Figure II-14a and Figure II-14b, respectively.

Figure II-14b shows velocity vectors evaluated by tracing the wave propagation lines at selected locations along y = 20 cm, 50 cm, 80 cm, 110 cm, 140 cm, 170 cm, and 200 cm. For comparative displays, the velocity vectors obtained from different rates of interpolation are presented at time instances chosen regularly with 0.8 seconds of intervals in both figures in Figure II-14b. In spite of the different interpolation rates, temporal and spatial evolutions of wave front velocities at the same time instances are indistinguishably similar to one another (e.g., less than 1% difference for overall time series). In order to examine the accuracy of the interpolated wave front velocities from the wave front tracing method, the velocities based on the interpolated wave front lines are compared to those obtained by taking derivatives of the wave front position functions defined by (19), while employing the time intervals identical to the respective interpolation rates $\Delta t = 0.4$ *s* and $\Delta t = 0.2$ *s*.

Figure II-14c shows time series of the velocity ratio $\left\{n\frac{\Delta y}{\Delta x}\right\}_s \Big/ \left\{n\frac{dy}{dx}\right\}_{anal}$, evaluated based on the wave front lines determined with time intervals $\Delta t = 0.4$ *s* (left) and $\Delta t = 0.2$ *s* (right), respectively. The wave front tracing method applied for the interpolated wave front lines shows fairly accurate velocity estimations deviating less than 10% from the analytically calculated velocities. Therefore it is concluded that the uncertainties in positions of interpolated wave front lines could induce up to 10% deviation in the propagation velocities against those obtained by analytic calculations. The increased deviation was observed near y = 20 cm, where the distance between the consecutive wave front lines was very small as $\Delta s < 1$ cm (or $\Delta s < 1$ pixel) with $\Delta t = 0.2$ *s* interpolation. On the other hand, the increase in the velocity ratios along y = 20 cm started decreasing from $t \approx 4$ s when the mean displacements of the wave frontal lines became larger than 1 cm (~1 pixel with a 1 cm/pix resolution) between the consecutive time interval. It presumed that the over-interpolation must have produced slight variations in the wave front direction that could result in considerable errors in calculation of the wave front velocities that deviated up to 10% from the analytically calculated velocities. Such errors due to over-

interpolation could be reduced when the pixel resolution for the nodal points for x_i and y_i was more confined. That is, increasing the number of pixel points used to describe respective wave front positions at each time instant $\Omega(x, y, t)$ for the same spatial spans (l_y; hence, ∂y_i or ∂x_i < 1 c*m*/*pixel*) reduced the deviation in the wave front velocities. However, a factor one increase in pixel resolutions resulted in significant increases in computational time while achieving merely 3% improvement in the velocity ratio. Note that this is the accuracy anticipated from the wave front velocities evaluated with the wave front lines obtained at a time interval Δt = 0.6 *s* (with no interpretation) with the original pixel resolution of 1 *cm/pixel*. Furthermore, in practice, the pixel resolution for the data images is determined during the image collection, for example, depending on the capacity of the camera, thus it is a pre-determined parameter.

Therefore, this comparative error estimation concludes that with the considered pixel resolution (an order of 1 c*m*/*pixel*), the wave front tracing method can provide satisfactorily accurate estimations for propagating wave front velocities with less than 3% of standard error. The interpolated wave front positions can be used to obtain equivalently accurate wave front velocity information. However, when over-interpolated for mean displacement of the wave front positions between the consecutive time steps that are smaller than the pixel resolution (e.g., ∂y_i or ∂x_i < 1 c*m*/*pixel*), the range of errors can actually increase. In this case, the present study evaluated that the interpolated wave front velocities could deviate up to 10% from the analytically calculated wave front velocities.

Further examinations were conducted to find the optimal rate of temporal interpolations with respect to the original function generated with a time interval Δt_o = *0.6 s*. The standard errors in the velocity ratio $\left\{n\frac{\Delta y}{\Delta x}\right\}_s \Big/ \left\{n\frac{dy}{dx}\right\}_{anal}$ were evaluated with interpolated wave front lines obtained at varying interpolation time intervals of Δt = *0.1 s*, *0.2 s*, *0.3 s*, *0.4 s*, and *0.5 s*, respectively. Results indicated that the interpolation rate $\Delta t/\Delta t_o \geq 0.5$ (with Δt =*0.3 s*, *0.4 s*, *0.5 s*) gave optimal velocity evaluations, maintaining standard errors in the velocity ratio within 5%. Mean displacements of the consecutive interpolated wave front lines were about 10 pixels $\leq \Delta s \leq$ 20 pixels.

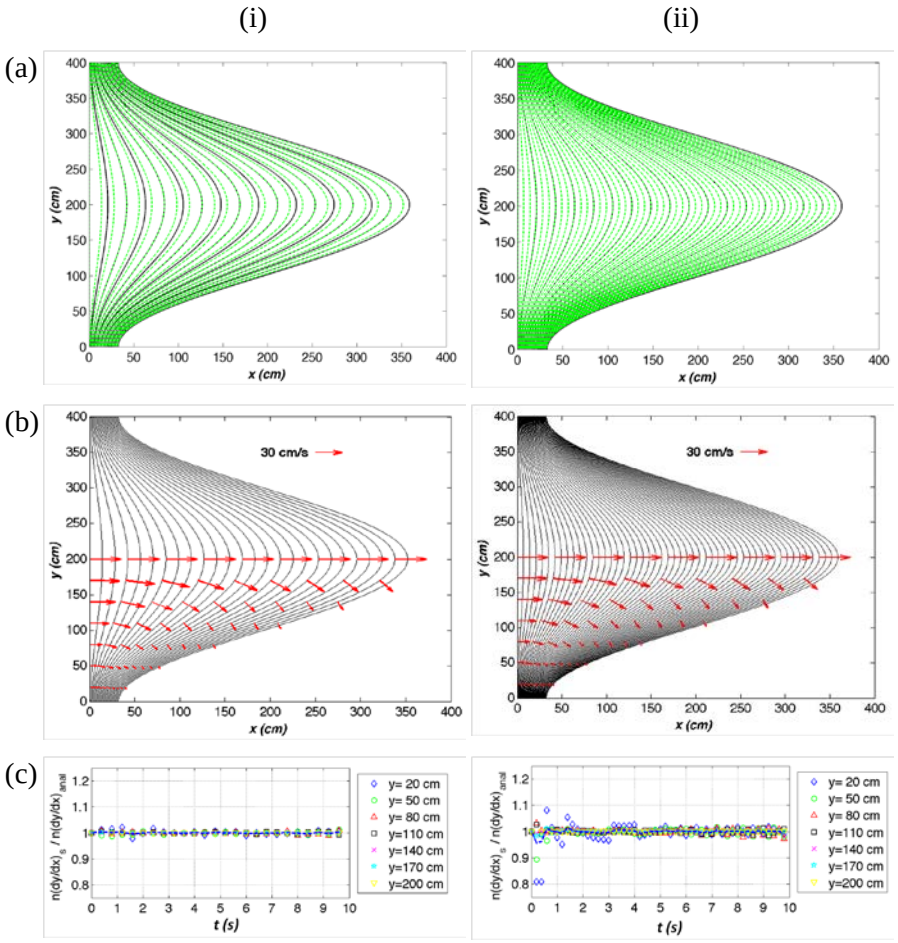

Figure II-14 Wave front velocities based on interpolated wave front lines. The original Wave front lines determined by a cosine function determined with Δt = 0.6 *s* (solid lines) in Figure II-13 interpolated with (ii) Δt = 0.4 *s* and (ii) Δt = 0.2 *s*. (a) Interpolated wave front lines (broken lines), (b) wave front velocities evaluated by the wave front tracing method based on the interpolated wave front lines; The velocity vectors are selectively presented with a constant time intervals of 1.2 s both in (i) and (ii), and (c) time series of the velocity ratio $\left\{n\frac{\Delta y}{\Delta x}\right\}_s \Big/ \left\{n\frac{dy}{dx}\right\}_{anal}$ at selected locations along y = 20 cm, 50 cm, 80 cm, 110 cm, 140 cm, 170 cm, and 200 cm (see the legend in Figure II-13 for marks).

On the other hand, the wave front positions between the consecutive raw images obtained with irregular time intervals ($\Delta t \approx 0.1$ s) indicated that the wave front propagated with the mean displacement equivalent to 100 pixels $\leq \Delta x \leq$ 150 pixels per second (Δt = 1 s). This could be approximated as the mean displacement ranging for 5 pixels $\leq \Delta x \leq$ 7.5 pixels per Δt = 0.05 s.

Therefore, in order to maintain the mean pixel distances between the consecutive front lines (e.g., time steps) within ranges that would result in 5% of standard errors in the velocity ratio, the wave front lines were interpolated with a time interval Δt = 0.05 s ($\Delta t/\ \Delta t_o \approx 0.5$) in the following analysis, prior to the velocity calculations. As a result, the interpolated wave front lines are reproduced with the mean displacement between consecutive time steps of 7.5 cm on average. Accordingly, wave front velocities evaluated based on the interpolated wave front positions are believed to give optimal accuracy in the velocity calculation, within 5% of standard error in the velocity ratio. In the next section, the wave front velocities evaluated by the wave front tracing method are compared for validation to those from the ADV measurements.

Validation: comparison to direct, ADV measurements

For validation, the wave front velocities for x and y components were evaluated by the wave front tracing method along y = 0 m and y = 1.2 m, corresponding to the measurement points A and B of ADV4 and ADV3, respectively. The velocity results were compared to the velocity time series measured from ADV3 and ADV4 (see Table II-2 for measurement locations). Overall velocity variations in the u velocities from the wave front tracing method demonstrated similar patterns to those observed from the u velocity measurements from ADV instruments. However, the time histories of u and v velocities from the ADV measurements showed severe scattering and discontinuation in the u and v velocity time histories between t = 34.0 s and t = 34.5 s from ADV3A and between t = 34.0 s and t = 35.5 s from ADV4A, respectively, when the wave front arrived at the sensor locations. Such significant velocity fluctuations were also observed from the velocity time histories obtained from the wave front tracing method. This must be indications of strong turbulence effects in the wave front. Comparison of the wave frontal velocities to those from the both ADV3 and ADV4 showed considerable deviation in u velocities, especially at measurement point A in the front. On the other hand, a significant portion of the velocity information appeared to be missing in the ADV records during the early passage of the turbulent wave frontal flows. This demonstrates a possibility that the point-measurement technique could lack capacity for measuring the turbulent, air-water mixed flow in the front. On the other hand, the wave front velocity records showed that the u velocity converged to U = 2.0 m/s approximately when it passed ADV measurement positions A and B. This convergent velocity U is maintained until the wave front reaches the end of the flat section. The alongshore v velocity

records show even wider variability, while remaining within a relatively smaller velocity range of ± 0.5 m/s.

II.3.4 Summary of this section

This section introduced the "wave front tracing method," evaluating wave front velocities based on the wave front function $\Omega = \Omega(x, y, t)$ determined during the long-wave runup on the inland plane inundation field. The method uses the post-processed wave front lines obtained after smoothing out the minute fluctuations in the wave front positions as input wave front function. Thus, the wave front functions are assumed to represent the initial inundation water lines associated with the dominant runup flow. In the following procedures, wave front velocities were calculated based on the wave front slopes by assuming the wave front propagated along the orthogonal direction to the wave front position. The comparative validation studies suggested that the wave front velocities from the "wave front tracing method" would result in at most 10% of mean deviation from the analytically calculated velocities for the image data capturing the wave propagation with resolutions $\geq$ 1 cm/pix. Furthermore, when the raw wave front positions were interpolated, it suggested that the interpolation rate $\Delta t / \Delta t_o \geq 0.5$ would provide optimal velocity evaluations, maintaining standard error in the velocity ratio within 5%.

The following section presents the wave front velocities calculated based on the interpolated wave front positions on various vegetation patch configurations introduced in II.2.2. The wave front velocities were calculated based on the raw image data collected with a pre-determined pixel resolution of 2 cm/pix. The wave front position functions, originally obtained at irregular time intervals, were interpolated with a regular time interval Δt = 0.05 s (Δt / $\Delta t_o \approx 0.5$). Accordingly, the result wave front velocities are believed to provide the velocity calculation within 5% of standard error in the velocity ratio.

II.4 Results

II.4.1 Effects of the variations in macro-roughness due to varying patch size

The wave front tracing method is applied to investigate effects of large-scale discontinuities in vegetation roughness on structures of initial inundation wave flows. Figure II-15 shows temporal evolutions of wave front positions (Figure II-15a) and running-up wave velocity structures (Figure II-15b) on the vegetated fields. Comparisons are made between the vegetation patch configuration G1 (D = 1.2 m, $\Delta S/D$ = 2.7) and G3 (D = 1.7 m, $\Delta S/D$ = 1.8).

Note that these correspond to 9.1% and 18.4% of planar area coverage by patches with G1 and G3, respectively.

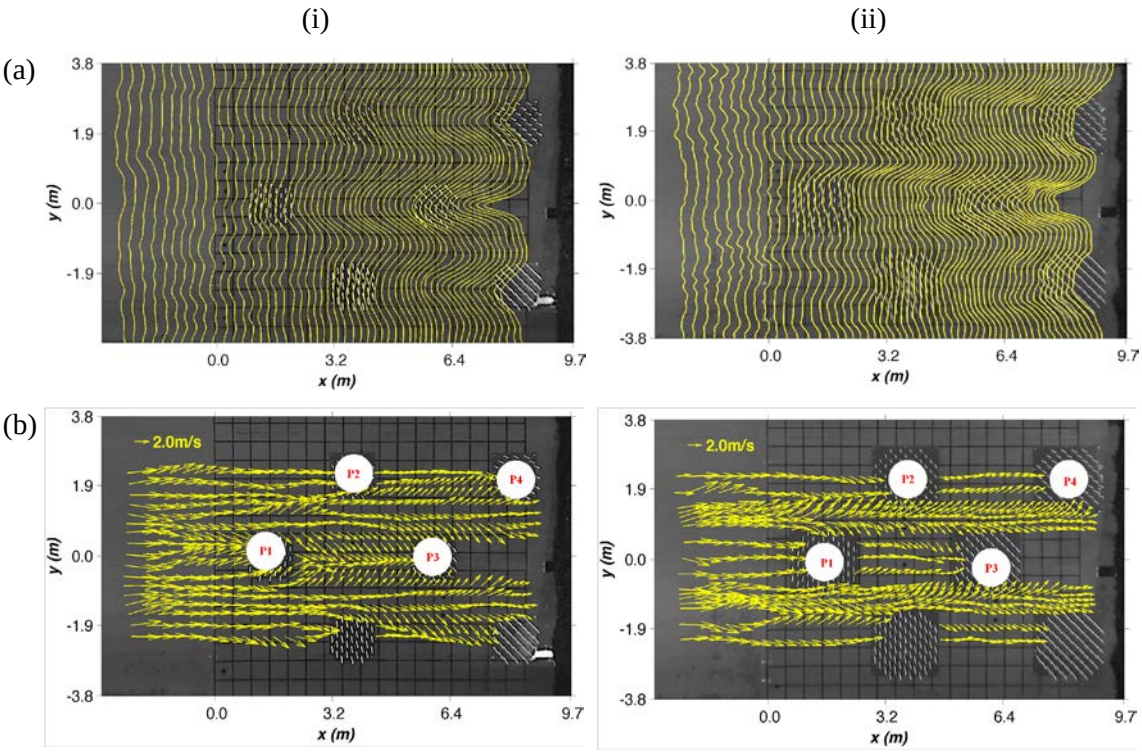

Figure II-15 Temporal evolutions and velocity structures of running up wave fronts propagating on (i) G1 and (ii) G3. (a) Wave front positions evaluated with Δt = 0.05 s time interval during wave running up phases, (b) wave front velocity maps at 17 selected locations in y specified at y = 0, ±0.30 m, ±1.92 m, ±2.22 m (centers and semi-centers of the vegetation patches in the center), y = ±0.60 m, ±1.36 m, ±1.62 m (sidelines of patches in the center), and y = ±1.10, ±0.84 m (channels on either side of the patches near the center); velocity vectors are plotted at alternative wave front positions of (a) with 2Δt = 0.10 s time interval.

The wave front positions are evaluated with a regular time interval Δt = 0.05 and x and y locations are specified according to the local coordinate system defining the beginning of the onshore flat section in the vegetated region as x = 0 (e.g., the start of the grid on the bottom) and the alongshore center of the vegetated region as y = 0 (both in meters). Figure II-15b shows velocity vectors evaluated by the wave front tracing method, based on the wave front positions

(Figure II-15a) during wave runup. While full-field velocity information is available, Figure II-15b presents velocity vectors essentially along the selected 17 locations in y specified at y = 0, ± 0.30 m, ± 1.92 m, ± 2.22 m (centers and semi-centers of the vegetation patches in the center), y = ± 0.60 m, ± 1.36 m, ± 1.62 m (sidelines of patches in the center), and y = ± 1.10, ± 0.84 m (channels on either side of the patches in the center).

In order to characterize the complex flow-patch vegetation interactions demonstrated by the velocity structures in Figure II-15, spatial variations of x and y velocity components are quantified and plotted against temporal positions in x of wave fronts. Figure II-16 shows spatial variations of u and v along the fixed y locations y = +1.1 m ("□," blue; a center of the channel), y = + 0.6 m ("O," red; outer boundary of the patch), and y = 0 m ("◊," black; a center of a patch).

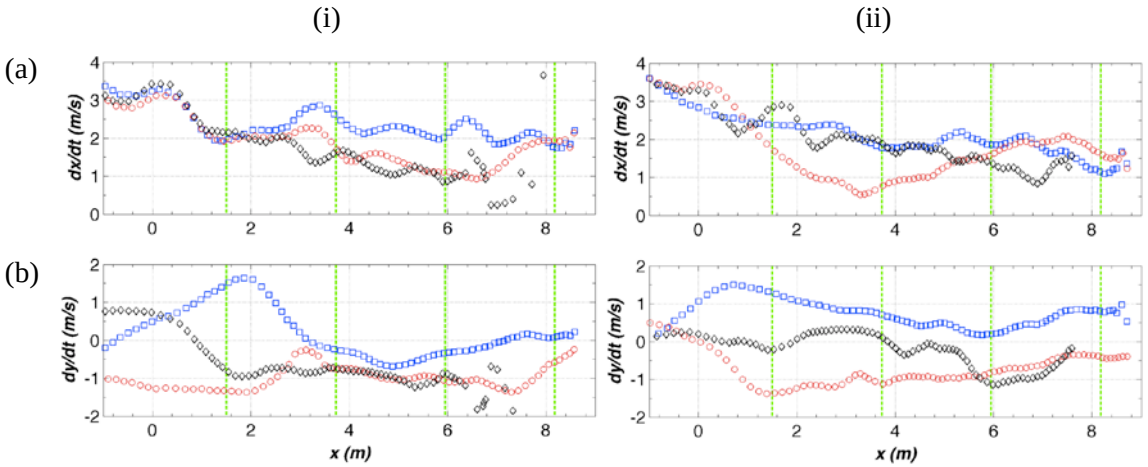

Figure II-16 Spatial variations of u and v along the fixed y locations against wave front positions in x on G1 (i) and G3 (ii). (a) u velocities, (b) v velocities. '◊', y = 0 m (black; a center of patch); 'O', y = +0.6 m (red, outer boundary of the patch); '□', y = +1.1 m (blue, a center of the channel).

Overall, u velocities in front of the first patch located at x = 1.5 m (i.e., will be referred to as a first patch or a reference patch) show rapid decreases from approximately a half-diameter ahead of the first frontal edge (P1, see Figure II-15) on both G1 and G3 (Figure II-16a). After passing through the P1, u velocities behind the first patch on G1 start decreasing somewhat

monotonously as the wave front passes the staggered patch arrays between the P2 (x = 3.7 m) and P3 (x = 6.0 m) rows. However, the decrease in u velocities behind the P1 on G3 is much slower. As expected, the highest velocities in the x direction are observed from flows through the open gaps between discrete patches (e.g., y = 1.1 m).

Within the x direction extent between the patches in the second and fourth rows (i.e., between P2 and P4), the u velocities along the channel maintain fairly constant speeds. The lowest u velocities are observed in the flows tangential to the side boundaries of the first patch along y = 0.6 m. Decreases in u velocities are most prominent at y = 0.6 m with G3 where u velocities on the (upper) side of the P1 tend to remain near the lowest speeds of u ≈ 0.5 m/s until the wave front passes through the following staggered patch region (P2 ~ P3). This can be related to variations of the y direction velocities in Figure II-16b. That is, the spatial variations of the x and y velocity components show that v velocities along the line y = 1.1 m start increasing when the wave fronts approached the first patch (P1), a distance of ~ D/2 prior to the patch front, with both G1 and G3. However, with G1, the v velocities continuously increase in flow through the opening until the wave front passes through the P1. As the wave front enters the staggered patch arrays surrounded by P2 and P3, v velocity starts decreasing. When the wave front position reaches near x = 3.7 m, next to the center of P2, the direction of v in the channelized opening reverses toward the alongshore center of P1 with G1. However, the v velocities along the line y = 1.0 m with G3 show rather gradual decreases until the wave front passes through the patches in row P3. Hereafter, the flow increases again and is redirected toward the relatively wider open spaces between the patches in the third and fourth rows. The v velocities behind the center of the first patch on G3 remain nearly zero with slow gradients between ± 0.35 m/s while the wave front passes across the staggered patch arrays.

It is interesting to notice that the relatively the small patch array with relatively wider open gaps $\Delta S / D$ = 2.7 of G1 appears to be more effective in redirecting the shore-normal incoming wave flows toward nearby channels at the frontal part of the vegetated area. This results in considerably rapid decreases in the x direction flows behind. On the other hand, the larger patches with $\Delta S / D$ = 1.8 of G3 are observed as effective in suppressing the alongshore variability in flow behind the frontal patches. Consequently, differences in u velocities between the flows along the center of the opening and those along the centerline of the patch are observed as insignificant while the wave front passes between P1 and P3 . This may be because the large

patches of G3 are effective in holding the flow within the patches and keeping the flow along the openings from invading in to the patches from sides.

The alongshore variability, that is the changes in direction and speed of the v velocity component, is examined in regard to patch size and alongshore openings between patches. Figure II-17 shows the v velocity variations along the y directions at selected locations in x = 2.60 m (a, behind P1), 3.73 m (b, x locations of P2), 4.85 m (c, in front of P3), and 5.95 m (d, x locations of the patches in the third row). Individual plots in Figure II-17 contain *v* velocities from 17 alongshore locations in which y locations are identical to where the velocity vectors are evaluated in Figure II-16b. Furthermore, as the flow fields are assumed symmetric with respect to the center of the vegetated fields (y = 0 or P1), the velocity points on the upper half section above y = 0 are flipped to their corresponding symmetric points on the lower half section. Thus, the velocity vectors from the same distances away from y = 0 could be plotted together on the same plain.

As discussed earlier, the wave front velocity records showed that u velocity of the wave front of the "7-s full stroke wave" were commonly converged to U = 2.0 m/s when it reached approximately x = 3.7 m on the plain flat section with no patch geometry. The propagating velocities of the inundation flow in the vegetated area must vary depending on the initial wave conditions as well as the macro roughness effects from the vegetation. Here, the velocities in Figure II-17 are normalized by the convergence velocity U = 2.0 m/s with an attempt to measure the variability in the inundation flow relative to the convergent velocity that the inundation flow velocity would have reached on the fixed initial wave condition (see the discussion in section II.1.1). Hence, the scaled velocity must essentially measure the dynamic responses of the vegetated flow velocities against the macro roughness effects from vegetation patches in different configurations. In addition, patch layouts G1 and G3 consistently show symmetric configurations with respect to the centerlines of the center-most patches (e.g., P1 in Figure II-16). Moreover, the velocity structures of the wave front also show distinctive patterns that are symmetric with respect to the centerline of the reference patch P1 (e.g., Figure II-16Figure II-16b). The variability in the v velocity became more significant across the outer boundary of each patch (i.e., $y \geq \pm D/2$). Therefore, the y position denoting the y directional distances of each velocity point from the center of the reference patches (e.g., P1) on each patch layout are scaled by the patch radius $R = D/2$ for both G1 (a left column in Figure II-17) and G3 (a right column in Figure II-17).

The alongshore velocity evolutions shown in Figure II-17 demonstrate evident planar circulation patterns that are observed during wave propagation across the vegetation arrays on both G1 and G3. That is, as the wave front has passed P1, the differences in the propagation speeds of flows surrounding P1 induced vortex-like structures where flows tend to circulate inward toward the center of a patch P1. However, relatively strong cross-shore directional flows along the channel and patch obstacles P2 intervened in further development of inward directional (e.g., positive on the right side of P1) flows, resulting in discontinuity in the v velocity evolutions. The discontinuity point is observed to be at the center of the channels near $y = \pm 1.25R$ (Figure II-17a and Figure II-17b). Especially as the wave front passes by the next patch P2, flow on the other side of the channel develops another inward motion toward the respective center of patches in the row P2. Therefore, v became opposite in the y direction against the flow around P1. Consequently, the flow farther away from a center slows, and eventually overall alongshore direction flows form a symmetrical structure with respect to the center of the channel at $y \approx \pm 1.2R$ (Figure II-17c and Figure II-17d).

It is interesting to notice that the wave front velocity fields around G1 and G3 exhibit identical planar velocity structures in spite of differences in size of employed patches. According to Figure II-17, the speed of v velocities varies slightly more within $v = \pm 0.3U$ with G1, whereas the variation is within $v = \pm 0.2U$ with G3. However, the differences between *v* velocities on G1 and G3 at the corresponding moment seem insignificant. This may indicate that developments of planar flow patterns at the present length scale, especially the rates of accelerations and decelerations of alongshore flows, are controlled dominantly by the channel arrangements or, in other words, the distances between discrete patches.

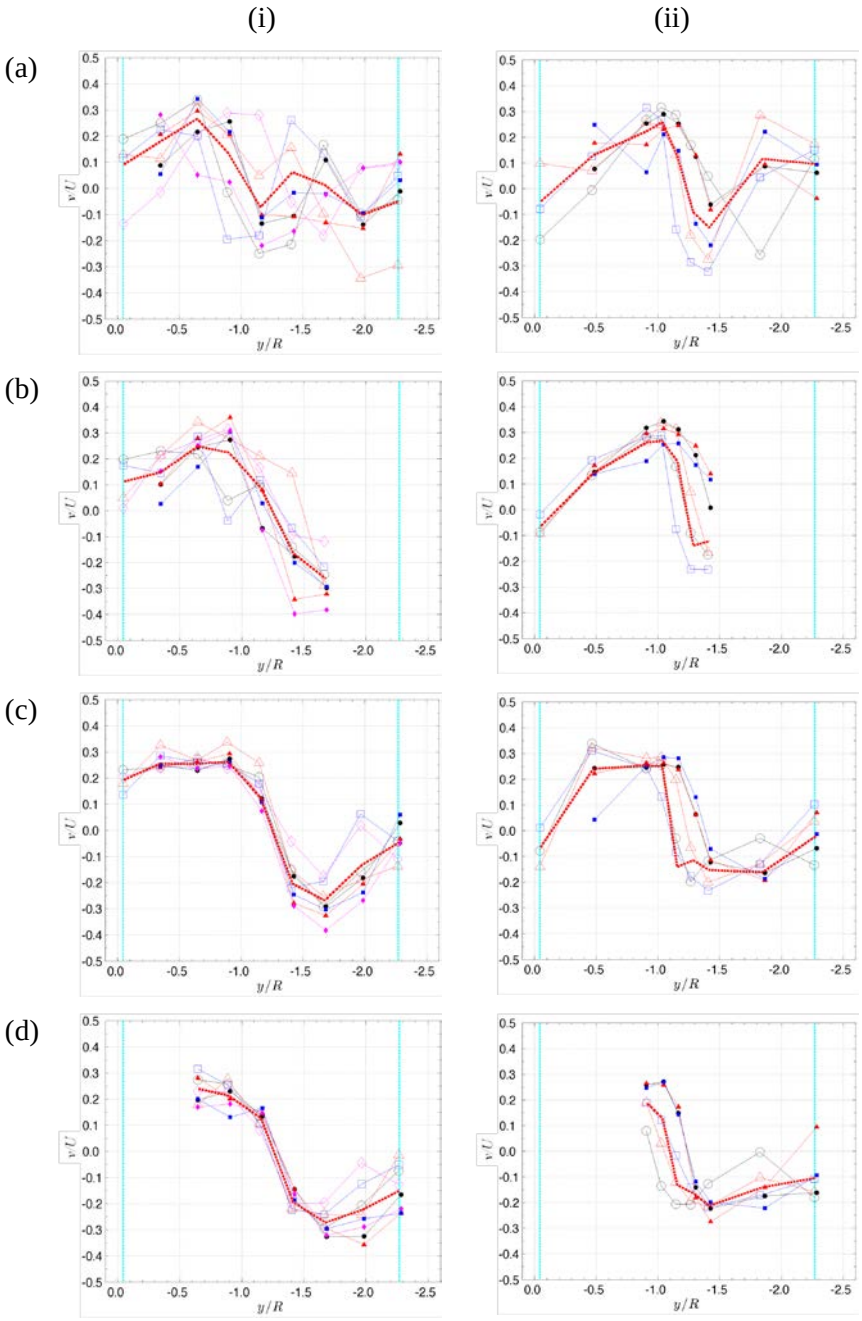

Figure II-17 Evolutions of the alongshore velocities during wave propagations across the vegetated arrays on both G1 (i) and G3 (ii). The alongshore distributions of *v* velocity components are obtained from the velocity vectors in Figure II-16b at selected cross-shore location at (a) x = 2.60 m, (b) x = 3.73 m, (c) x = 4.85 m, and (d) x = 5.95 m. *v* velocities are scaled by the convergence velocity *U* = 2.0 m/s and the y directional distances from the center of P1 are scaled by patch radius *R* = *D*/2 respectively for G1 and G3.

II.4.2 Effects of varying spacing between macro-roughness patches of constant size

The effects of vegetation patch arrangements are investigated with G2 (D = 1.2 m, $\Delta S/D$ = 1.9), a patch layout that consists of 12 densely spaced small patches identical to the patch size used for G1 (D = 1.2 m, $\Delta S/D$ = 2.7). Note that these correspond to 9.1% and 18.4% of planar area coverage by patches with G1 and G2, respectively. Figure II-18 shows temporal evolutions of wave front positions (Figure II-18a) and velocity structures of running-up wave front (Figure II-18b) around the vegetation patches. While the wave front positions are evaluated on overall fields, the front lines are presented limitedly up to the frontal edges of the patches in the fourth row, where velocity information is comparable to that of G1. The wave front interactions with multiple patches on G2 produced complex planar oscillations in the front lines corresponding to the appearances of the respective patches and channels along the y direction. These oscillations resulted in wave front lines from different time instances condensed in close proximity to each other when plotted together. The velocity field in Figure II-18b shows the wave frontal flow evolutions along 9 selected locations in y specified at y = 0, ± 1.57 m, (centers of the vegetation patches in the center), y = ± 0.60 m, ± 0.97 m (sidelines of patches in the center), and y = ± 0.78 m (centers of channels on either side of the patches in the center).

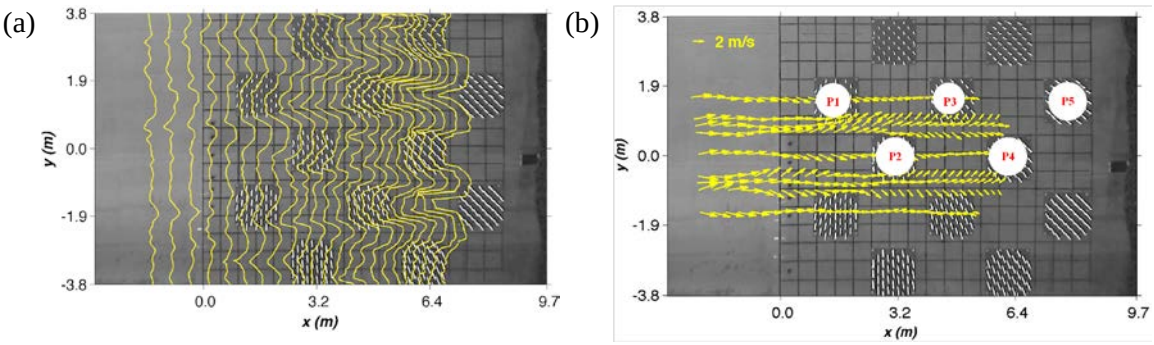

Figure II-18 Temporal evolutions and velocity structures of running up wave fronts propagating on G2. (a) Wave front positions evaluated with $4\Delta t$ = 0.20 *s* time interval during wave running up phases, (b) wave front velocity maps at 9 locations in y specified at y = 0, ±1.57 m, (centers of the vegetation patches in the center), y = ±0.60 m, ±0.97 m (sidelines of patches in the center), and y = ±0.78 m (centers of channels on either side of the patches in the center); velocity vectors are plotted at alternative wave front positions of (a) with $2\Delta t$ = 0.10 s time interval.

Frequent obstructions of multiple patches induced repeating deceleration and acceleration cycles of the front flow velocities in the x direction. This displays as multiple humps in the spatial distributions of u velocities in Figure II-19a. Also note that the u velocities along the channel, center, and sideline of each patch maintain notably similar patterns that converged to a relatively steady velocity slightly lower than the convergence velocity U = 2 m/s previously observed on inundation flows over a no-patch, flat section.

On the other hand, variability of the v velocities becomes eminent about a half-diameter ahead of the patches in the first row (i.e., P1 in Figure 2b), similarly observed with G1 and G3. However, Figure II-18b and spatial distributions in v in Figure II-19b both show that fluid along the channel tends to be conveyed toward the center of nearby patches and the alongshore directions remain same after x = 2.0 m until the front line reaches the relatively wide opening area in between two patches in P5 at the end. This is somewhat similar to what is observed from the channel flow on G3. The alongshore flow next to the patch sideline near y = + D/2 initially shows patterns similar to those observed from the channel flows in front of P1 of G1 and G3. That is, the flow tends to diverge away from the P1. However, in G2, the divergence is blocked by P1. Hence the diverging flow is rapidly redirected in the opposite direction, toward the center of P2 at y = 0.

The flows along the sidelines of the patches (i.e., P2) persistently direct the wave fluids toward the center during passage of the wave front through the following multiple patches. On the other hand, the v velocities along the center of P2 (e.g., y = 0) show continuous oscillation within v = ± 0.8 m/s with respect to the v = 0 m/s. Meanwhile, the flow is oriented mainly to the right orthogonal to the shoreline. Especially, it is noticed that v velocity oscillations along y = 0 occur with a frequency equivalent to the rate of patch appearance across the vegetated fields. Therefore, densely spaced multiple patches must be effective in redirecting the fluids channelized along the openings between patches toward the center area of neighboring patches. Consequently, the propagating speed over the alongshore extent of the flow field becomes fairly constant in x direction while the wave front line distribution shows patch scale oscillations at a frequency length scale equivalent to the size of a unit patch. As the wave front passes the patches in the frontal row, the wave propagating speed reached and stayed consistently near U = 2 /m in both channels and patch areas.

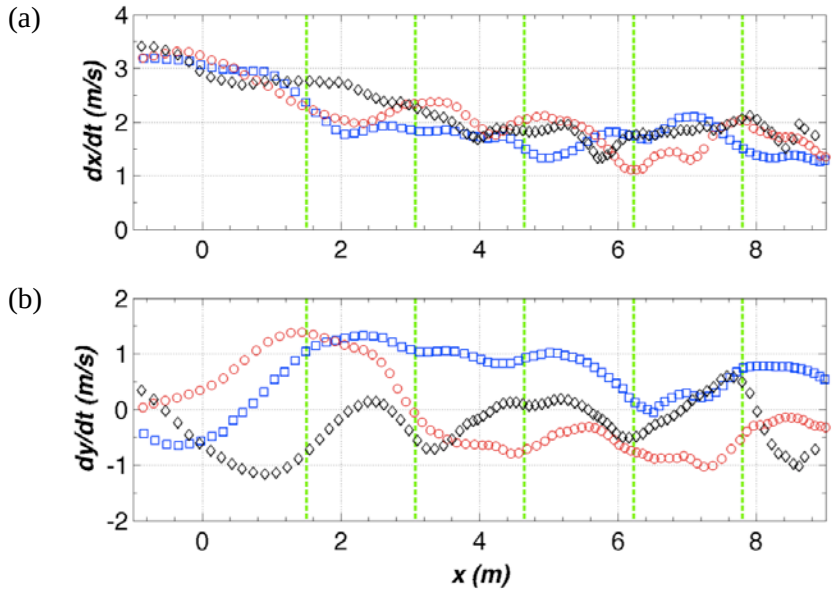

Figure II-19 Spatial variations of u and v along the fixed y locations against wave front positions in x on G2. (a) u velocities, (b) v velocities with wave propagations over x. '◊', y = 0 m (black; a center of patch); 'O', y = +0.6 m (red, outer boundary of the patch); '□', y = +1.1 m (blue, a center of the channel).

II.5 Discussion and future study

As indicated earlier, the rate of decrease in the u velocity across the patch P1 centerline was somewhat slower with G3 than it was with G1. With G3, the u velocity behind the P1decreased to u = 1.8 m/s (90% of U) at P2 and 1.5 m/s (75% of U) in front of P3. The configuration of large patches with narrower open spaces in G3 is observed as effective in suppressing the alongshore variability in flow behind the frontal patches. Correspondingly, the reduction in u velocities of the flows along the opening are observed as insignificant when compared to the u velocities along the centerline of the neighboring patch. This may be due to the large patches providing a longer extent of resistance from the sides, holding the flow within the patch for a longer duration. Furthermore, such holding-up effects from G3 must keep the flow within the patch relatively saturated, therefore preventing the initial flow along the narrow opening from leaving toward the sides. Therefore, it is presumed that the large patches must induce a large inundation depth in the flow along the opening.

The patch layout of G2 consisting of 12 densely spaced small patches identical to the patch size used for G1 has shown effectiveness in promoting flow exchange in the alongshore direction. Frequent obstructions of multiple patches induced repeating deceleration and acceleration cycles of the front flow velocities in the x direction. In response, the intervened fluid initially propagating along the patch area was redirected toward the open spaces between patches. Therefore, the large number of patches are observed as promoting fluid transport to the alongshore direction. Consequently, the propagating speed in x direction becomes fairly uniform alongshore when the wave front has reached the back of the vegetated field. The u velocities reached convergence velocities as the wave front passed through the patch arrays in the frontal lines and remain fairly constant to U = 2 m/s to the end of the wave runup.

It is interesting to note that both the ADV measurements and wave front tracing method have shown the wave velocities in the propagating x direction converging to $U = 2m/s$ once the wave front propagates further $x > 0.3L$ (L is the cross-shore directional extent of the inland inundation area). However, the convergent velocity U measured from the present wave front tracing method was much higher than the celerity of the gravity wave $\sqrt{gh} = \sqrt{g\zeta}$ = 0.9 m/s. Here ζ = 0.08 m is a water depth measured from the ultrasonic wave gauges co-located next to ADV3 and ADV4 (see Figure II-4). Yeh (1991) has reported that the propagation speed of the wave bore front developed from the fully breaking tsunami wave eventually reached a constant velocity that could be predicted from the initial conditions of offshore water depth. In the present study, the convergent velocity is observed as U = 2 m/s. Moreover, this convergent velocity is assumed as a characteristic wave front velocity that could be generated by the "full-stroke," 7-second waves employed for generating the inundation flow from the tsunami-like long waves in the present experimental conditions.

Similarity of the alongshore velocity structures between flows in G1 and G3 may indicate that developments of planar flow patterns, especially the rates of acceleration and deceleration of alongshore flows, are controlled dominantly by channel arrangements or distances between discrete patches at the present characteristic scale. On the other hand, it needs to be emphasized that the reversal of the flow direction observed with patch layout G3 has occurred within much narrower gaps between large patches. Therefore, such rapid variation in the alongshore flow orientation must involve significant shear stress around the outer boundaries of distinct patches, where discontinuity in macro roughness becomes prominent. Furthermore, effective

channelization of flows in the narrow opening between large patches must induce greater inundation depth.

Figure II-20 shows the time histories of the wave surface elevations at measurement locations A and B along the channel and patch, respectively. Compared to that on G1, significant increases are observed in water depth along the channel in G3 (Figure II-20b). Also it is seen that the water depth in the channel of G3 is approximately a factor one larger than the water depth behind the patch P1 of G3 at corresponding x locations (Figure II-20,ii). The variation in the water depth along the patch centerline in the water depth between the P1 and P3 (Figure II-20b) shows insignificant differences in the initial inundation depth between the flows on G1 and G3. However, the large patches on G3 resulted in significant delays in the arrival of the maximum inundation flow at measurement location B ahead of P3. Note that the depth of this delay flow could be much as much as a factor three higher than the water depth that arrived earlier along the channel around t = 36 s. Therefore, distinct variations in the inundation flow depth in the corresponding locations between G1 and G2, and also within G3, confirm the effectiveness of the large patch from G3 in promoting water channelization along the opening and in delaying the arrival of water behind the macro-roughness patch area. On the other hand, the patch configuration on G1 is proved as effective in delivering the inundation flows with relatively uniform distributions alongshore.

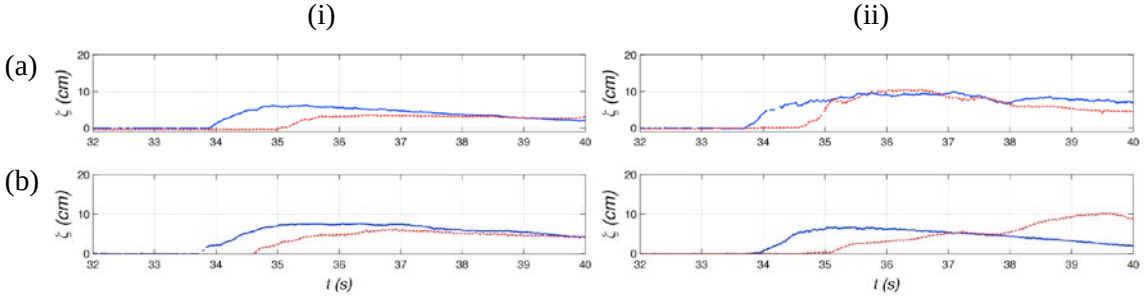

Figure II-20 Variations in the wave surface elevations around the G1 and G2. Measurements were made from the ultra sonic wave gauges (a) WG5 along the channel opening between P1 and P2 in Figure 2, and (b) WG6 along the centerline between P1 and P3. Comparisons are made between the inundation flow depth on (i) G1 and (ii) G3. Difference line styles indicate the varying measurements locations: 'solid', A; 'broken' (red), B

Hence, even the flow velocity along the channels between large patches reached about the same order of magnitude as what was observed in the channel flow with small patch layout. When multiplied to the vegetated water depth *H*, momentum force $F_H = \rho \Delta u H^2 or \rho \Delta v H^2$ of the fluid along the narrow gaps can be significantly impacting. However, the vegetation patch roughness produces complex flow structures where, for instance, a slight detention of the flow in one location can result in significantly increased momentum influx at the other side of the macro-roughness vegetation setup. Therefore, vegetated flow dynamics requires continuing study and systematic investigation.

II.6 Summary of findings and conclusions

The comparison of velocity information obtained by the wave front tracing method with that of the ADV instruments shows that wave front tracing methods could effectively evaluate turbulent wave flow velocities. Overall velocity variations in the u velocities from the wave front tracing method demonstrated similar patterns to those observed from the u velocity measurements with ADV instruments. Therefore, it is concluded that the velocities obtained from the wave front tracing method effectively measure the temporal and spatial variations of propagating velocities of wave fronts.

On the other hand, significant data dropouts were observed with the ADV measurements while the wave front velocities were continuously presented at the corresponding moments. Furthermore, measured velocities from the ADVs tended to be lower and become available at slightly later timing than when wave frontal velocities are measured at the equivalent moments. Therefore, it is presumed that the velocity measurements from the ADV instruments must be representing the flow velocities following the turbulent, air-water mixed flows in the front of the runup waves.

The wave front tracing method was employed to investigate the initial flow patterns of vegetated flows during the long-wave runup. Three distinctive configurations for patch layouts that vary either in characteristic patch radius or in center-to-center spacing between patches were employed. In sum, a patch layout employed for G1 appears to be effective in reducing the u velocities along the channel: the wave front velocities along the centerlines of the reference patch consistently decreased to u = 1.7 m/s (85% of a convergence velocity U = 2m/s) behind the patch P1 and 0.9 m/s (45% of U) further behind, in front of patch P3 at x = 6 m. However, in the channel, u velocities hardly reduced below the convergence velocity. On the other hand, the

patch layout employed for G2 is observed as rather effective in uniformly reducing the u velocities alongshore.

In the context of examining the effects of the opening space between multiple porous patches, it is recommended to investigate patch spacing that could effectively balance fluid conveyance and flow-moment force reductions. This may be achieved, for example, by employing different arrangements of macro-roughness patches while maintaining the size of the unit patch and keeping numbers of employed patches constant. Furthermore, the influence of patch size on reduction and increase of flow speeds around individual patches need to be examined in greater detail. This may be achieved by employing the current configurations for the patch layouts while allowing variability in stem spacing within a patch.

This present research has investigated the tsunami inundation response to spatial variability in onshore bottom characteristics, including the effect of bottom discontinuity due to presence of coastal vegetation. The observed spatial variations in velocities and depth of long-wave inundation flow suggest that large-scale discontinuity of coastal vegetation will significantly alter tsunami inundation patterns and consequential hydraulic impacts on coastal buildings and infrastructure. Quantitative descriptions of spatial variability of the long-wave inundation patterns accounting for the inland bottom complexity will provide a means to improve predictions of tsunami inundation extents and initial wave impacts on the coastal environments. Therefore, use of findings in this present study can be extended for more accurate tsunami warning, better evacuation planning, and improved risk analysis. Furthermore, the present method of analysis, evaluating tsunami inundation flow response to varying discontinuous roughness characteristics, can be applied for other extreme long-wave problems where interaction of wave runup flow with onshore macro-roughness structures. Examples include coral reefs and buildings on the beachfront, which can promote flow channelization and change the hydraulic loads on coastal structures.

This material is based upon work supported by the National Science Foundation under Grant Numbers (CMMI-0936595 and CMMI-1206271). Any opinions, findings, and conclusions or recommendations expressed in this material are those of the author(s) and do not necessarily reflect the views of the National Science Foundation.

CHAPTER III

KINEMATICS AND DYNAMICS OF LARGE-SCALE, THREE-DIMENSIONAL GREEN WATER WAVES ON OFFSHORE STRUCTURES

III.1 Introduction

III.1.1 Background of dynamic impacts of extreme waves on ocean structures

Interaction with extreme waves is one of the major concerns in the design of coastal and ocean structures. When intensified under severe weather conditions and by extreme geophysical forces such as hurricanes and earthquakes, ocean waves increase in height and can reach above the lower decks of those structures. Waves breaking and subsequently generatingthe "green water impingement" are the extreme events that can exert tremendous impact loads on marine facilities and equipment. Numerous studies have reported structural damage caused by extreme waves (e.g., Leonhardsen et al., 2001; Xu and Barltrop, 2008; Xu et al., 2008). Some also have reported damage caused by secondary loads from collapsing air pockets trapped underneath free surfaces during the deformation of overturning waves (Chang et al., 2011; Bullock et al., 2001). The aerated overtopping flow generated after the wave impingement tends to develop turbulent bores that induce increased shear frictions and sudden turbulent energy releases on structural surfaces (Cox and Cooker, 1999; Pedrozo-Acuna et al., 2008).

Out of necessity, early studies of extreme waves focused on predicting wave elevations over the deck clearance level (Forristall 2000; Kriebel and Dawson, 1993; Mori et al., 2002; Haver and Andersen, 2000; Greco et al., 2001) and on coastal structures in shallow water regions (Franco and Franco, 1999) in proximity of breaking waves. Some studies have adopted the statistical approach of developing probability models estimating the rate, volume (height), and velocities of green water overflows. Ochi and Tsai (1984) have developed a statistical prediction method for impact pressures from breaking deep water waves on cylindrical structures. Hamoudi and Varyani (1998) evaluated the probability and occurrence rate of deck wetness as functions of Froude number, significant wave height, and impact load. Stansberg (2000) and Stansberg and Nielsen (2001) have evaluated the exceedance probability of extreme waves over the deck based on the laboratory observation of the random wave evolutions and runup heights on cylinders. Cox and Scott (2001) have conducted systematic wave simulations

through a small-scale laboratory experiment and developed the likelihood prediction of waves overtopping the deck structure. They presented an empirical model equation that linked the overtopping flow volume rate to the incipient wave conditions. Mori and Cox (2003) developed the simplified, statistical model that predicted the maximum volume and rate of overtopping flows over the fixed deck based on the probability distribution of the wave crest measurement. They presented the formulation for the maximum horizontal velocities of deck overflow assuming a linear sinusoidal wave in deep water. However, the formula was limited by employing the constant incoming wave velocity u_{max} qualitatively estimated by assuming the velocity changes during wave collapse on the deck front were not significant.

Numerous investigations have focused on impact dynamics of the green water waves on offshore moored and floating units (e.g., Buchner, 1995; Leonhardsen et al., 2001; Faltinsen et al., 2002; Xu et al., 2008). Buchner (1995) performed a series of laboratory experiments to investigate the impact load and green water occurrence on floating production storage and offloading (FPSO) units. . Buchner also discussed the effect of wave height, wave period, and current velocities that need to be considered when designing FPSOs. .

Hamoudi and Varyani (1998) used load cells to measure the impact loads on the deck of a model vessel by implementing the load cell measurement. Based on the load cell data, they developed a probability method for evaluating deck wetness and a simplified model evaluating structurally significant impact forces. However, they assumed no direct relation between wave celerity and flow velocity after overtopping, thus used the relative flow velocity that is the sum of the forward speed of the vessel and the wave velocity. They concluded that the probability of deck wetness is determined mainly by the freeboard ratio to the length of the vessel in a fixed sea condition.

Buchner et al. (2004) investigated the impact of offshore steep-fronted rogue waves on the bow front of FPSO models. The study recorded structural responses and motions of the model vessel relative to the sea surface motion, and pressures imposed by evolving irregular waves. They reported that the magnitude of the impact on the bow front was dominated by the local wave steepness, while the maximum impact pressures were measured near the crest of the impinging waves. Furthermore, they showed that peak wave impacts occurred at the same moment as the maximum vertical velocity of the free surface , and therefore the authors suggested using that as an input parameter for a prediction model. Furthermore, they concluded

that second order wave theory had given a reasonable prediction for wave height, although it was unable to reproduce the asymmetry commonly observed in nonlinear waves.

Xu et al. (2008) performed laboratory experiments to investigate dynamic responses of an FPSO vessel and the impact load on a bow. To simulate extreme waves, they developed the "constrained random waves" that statistically evaluated both average shapes of the highest wave and wave front steepness at a fixed sea-state based on linear random wave theory. Observation of the measured pressures on the bow front indicated that the magnitude of the average pressure is affected largely by the measurement area rather than by the shape of the prone area. Furthermore, based on comparison to the field measurement with the prototype FPSO (Schiehallion FPSO; Xu and Barltrop, 2008), the effect of air entrapped during flow aerations due to increased compressibility produced significant variations in structural responses when the laboratory model scale was less than half the full-scale geometry.

III.1.2 Review research on kinematics of air-water mixed flows

Due to the complexity of breaking wave phases, green water wave research focusing on kinematic aspects of impacting waves has been conducted experimentally by employing available measurement techniques such as Acoustic Doppler Velocimetry (ADV), Laser Doppler Velocimetry (LDV), and Particle Image Velocimetry (PIV). In ocean engineering research, ADV and LDV have been frequently applied to directly measure the wave water velocities at fixed measurement locations. Typically, the point measurement techniques are applied to measure flow velocities and turbulence structures continuously at fixed locations (i.e. Cox and Shin, 2003; Mori and Cox, 2003). However, they often lack spatial resolutions, and hence require extra measures to select adequate measurement points in order to avoid costly repetitions. Moreover, for reliable measurements, the fluid volume has to maintain contact with sensors. However, strong turbulence and air bubble mixtures under breaking wave surfaces easily interfere with velocity data collections during violent wave evolutions. In addition, *in-situ* measurement instruments often have intrusive sensors which disturb natural flow patterns; hence, the collected data may fail in reflecting realistic flow features (Chan, 1994).

Development of high performance cameras has allowed for more active investigations of extreme wave kinematics employing non-intrusive imaging techniques. Snapshot images are now used to visualize evolutions of surface shapes and to evaluate phase velocities from propagating wave surfaces (e.g. Chan, 1994; Hattori et al., 1994; Bredmose et al., 2003).

Futhremore, non-intrusive velocity measurement techniques such as particle image velocimetry (PIV) and laser Doppler velocimetry (LDV) that evaluate displacements of seeding particles traveling with wave flows have become more widely used. Because they capture wider ranges of flow fields simultaneously, the particle image techniques became more widely used for evaluating dynamic wave velocity fields with enhancements in temporal and spatial resolutions of measurement points (e.g., Ting and Kirby, 1994, 1995; Chan, 1994; Hull and Müller, 2002; Lugni et al., 2006 and 2010; Pedrozo-Acuña et al., 2008; Bredmose et al., 2010).

However, these methodologies have exhibited some limitations when applied to violent, multiphase flows such as those produced during wave breaking because seeding particles are untraceable or absent in the air-water interfaces. Some applications of the "shadowgraphy" method (e.g., Hassan et al., 1998) have shown applicability for violent multiphase flow measurements. However, the individual bubbles in the air-water mixtures are unidentifiable and therefore hard to correlate between images. On the other hand, Ryu et al. (2005) developed a bubble image velocimetry (BIV) technique that treats the air bubbles contained in gas-liquid mixtures as seeding particles. The BIV traces textures of shadow graphs of air bubbles in multiphase fluids and calculates their displacements between consecutive images for evaluating aerated flow velocities. The BIV technique was later applied in measurements of green water flows on two-dimensional structures (Ryu et al., 2007a, 2007b; Ryu and Chang, 2008) and three-dimensional structures (Chang et al., 2011; Ariyarathne et al., 2012), wave breaking on a sloping beach (Pedrozo-Acuña et al., 2011; Rivillas-Ospina et al., 2012), and open channel aerated flows (Lin et al., 2008; Lin et al., 2012). The BIV technique has been proven successful in measuring velocities in highly aerated flows and violent impacts between liquids and structures.

III.1.3 Breaking wave mechanics and air entrapment effects

The impact mechanism of the breaking ocean wave is a highly localized process: the magnitude and degree of the impulsiveness of the impact pressure vary significantly in both space and time, mainly due to the rapidly evolving wave surface shape (Chan and Melville, 1988; Oumeraci et al. 1993; Chan, 1994). In particular, ocean waves experiencing wave-wave and wave-structure interactions develop nonlinear increases in wave height until they break, due to reaching steepness limits or impingements on offshore structures. The overturning surfaces of breaking waves enclose an aerated gap between the interfaces of a wave crest and trough and often trap sizable air bubbles. The entrapped air influences various dynamic properties,

including surface tension and fluid compressibility during wave-structure interactions, gas transfer rates against dynamic impacts, total energy dissipation, etc. When the entrapped air is released immediately due to the dynamics of progressive waves, subdivided air bubbles promote the turbulent dispersion of breaking waves that consequently contribute to the phase mixing, buoyancy, and energy dissipation as well as a discontinuity in the free surface. Blenkinsopp and Chaplin (2011) have provided an excellent review of the physical process affected by air entrapment on breaking waves as well as an integrated discussion on the findings from numerous, relevant studies.

Due to the difficulty in formulating the boundary conditions of the water-air interface, the investigations of temporal variation of the void fraction for the two-phase flow of breaking waves have been conducted often through laboratory and field measurement (i.e., Blenkinsopp and Chaplin (2007 and 2011; Cox and Shin, 2003; Wood et al., 2000; Bird et al., 1998; Lim et al., 2008; Chanson et al., 2006; Papanicolau and Raichlen, 1988; Bonmarin, 1989; Kalvoda et al., 2003). There exist diverse perspectives about the wave parameters (i.e., chemical, biological, and physical properties of the waves) influential to the formation and evolution of air entrapment. The impacts of violent breaking waves were commonly investigated while considering distributions of entrapped air, focusing on the influence of size, shape and density of air bubbles (e.g., Lamarre and Melivlle, 1992 and 1994; Hattori et al., 1994; Cox and Shin, 2003;).

Improved visualization techniques have enabled observation of evolutions of breaking waves and formations of air entrapment during wave impacting. Consequently, more studies have focused on a temporal variation of volume ratio between entrapped air and water during the wave breaking process. Bullock et al. (2001) carried out laboratory experiments with both seawater and freshwater to compare effects of aeration on wave impact pressure with regards to various ranges of Reynolds numbers. They reported that the freshwater tended to form larger bubbles that coalesce more easily. The air bubbles in seawater were found to remain more persistently over several wave periods, providing more cushioning between the impacting wave and the structure. The entrapped air pocket or a cloud of air bubbles became compressed within a confined area during the wave impingement onto the steep-front structures, forming the lens-shaped thin air pocket. Wood et al. (2000) developed a theoretical model to predict the plunging waves' impact on a vertical structure that accounts for the compressibility of such constrained air and the consequent "bounce back" responses of the water body during the wave impact by extending the pressure-impulse theory model (Cooker and Peregrine, 1995). They concluded that

the “bounce back” model gave the optimal prediction of the impulse impact when the air pocket length was less than the depth of the water.

Various investigations have been conducted to determine the relationship between wave impact and air entrapment (i.e., Blackmore and Hewson, 1984; Hattori et al., 1994; Azarmsa et al., 1996; Bullock et al., 2001 and 2007;). It is generally accepted that a certain degree of aeration due to small bubbles tends to cushion direct impacts on solid structures. However, the entrapped air pocket or a cloud of air bubbles tends to be compressed within a confined area during wave interactions with steep-fronted structures. The importance of the compressibility of such entrapped air and the consequent “bounce back” (Wood et al. 2000) responses have been highlighted by many researchers through investigation into the impact pressure of plunging waves (e.g., Mikelis et al., 1984; Amenio and Rocca, 1996; Andruessi et al., 1999; Ibrahim et al., 2001; Cox and Shin, 2003; Rhee, 2005; and Chen, 2011).

III.1.4 Influences of air entrapments on laboratory scale wave dynamics

Studying the characteristics of flow aeration during wave breaking is important due to its effect on dynamic properties such as impact pressure, viscosity, and surface tension. These effects are unlikely to be simultaneously achieved in accordance with the Froude scaling law in hydraulic model tests (Kobus and Koschitzky, 1991). Generally speaking, freshwater wave impact pressures are often overestimated by about 10% when designed in the laboratory according to the Froude similarity (about 10%, Bullock et al., 2001) because those tests fail to reproduce the effect of entrapped air and its compressibility presented in prototypical seawater (i.e. Cuomo et al., 2010; Chansen, 2004; Blacksmore and Hewson, 1984). However, more discrete verification is required since there are two major mechanisms of plunging waves that affect the air entrapment: vortex rotation of the overturning crest that results in relatively large bubbles or an air pocket; and wave impact and lifting that results in smaller bubble plumes and splashing jets (Dane and Stokes, 2002; Blenkinsopp and Chaplin, 2011). Until breaking, the wave is predominantly influenced by gravity and inertia, thus the formation of relatively large bubbles may be controlled predominantly by impacting wave velocities (Ledesma, 2004). In fact, there are a number of studies dealing with the adequacy of the scaling laws for the bubbly flow test that were often considered in hydraulic modeling (i.e. Bullock et al., 2001; Couriel et al., 1998; Oguz et al., 1995; Prosperetti and Oguz, 1997). These studies reported that application of the conventional Froude law led to no obvious overestimation of the impact pressure within

the data range and that the effects of surface tension and fluid viscosity were negligible under strong wave impacts. However, once the wave is broken, the confined air bubbles undergo air-water-structure interactions including the compression and breakup of a large pocket and dispersion, coalescence, and rise of smaller bubbles. During this process, the air entrapment has significant effects on the dynamics of the turbulent flow, and as a consequence produces the "scale effect" on the laboratory scale experiment when the characteristics of such air bubbles were insufficiently revived.

Several studies have highlighted the "scale effect" caused by the flow aeration due to wave impact. For example, Bullock et al. (2001) compared experimental and field measurements of the ambient void fraction, a fraction of the air volume which remains in the overall volume of the fluid after the wave impact, in both freshwater and seawater. They reported that, during the laboratory-scale breaking wave simulation, the ambient void ratio of seawater was observed to be about an order of magnitude greater than that of freshwater as well as 2-3 times higher in field measurements even under smaller waves. A similar tendency –accumulation of the air plumes over repeated wave periods–was also observed by Blenkinsopp and Chaplin (2007 and 2011). Blacksmore and Hewson (1984) performed field measurements of wave impact pressures on a seawall and compared them to those estimated using a semi-empirical equation derived from laboratory experiments. They reported poor correlations, concluding that air entrapment, wave steepness, celerity, and period were the dominant factors affecting the prediction of the impact pressure in any scale. Oguz et al., (1995) and Prosperetti and Oguz (1997) have reported that the volumetric fraction of the air was dependent on the jet or impact wave velocities. Deane and Stokes (1999 and 2002) have found that the sizes of the bubbles produced by the laboratory and ocean breaking waves, respectively, compare well to each other. Additionally, Kobus and Koschitzky (1991) have suggested that, due to the similar bubble sizes, the rise velocities of the bubbles in the laboratory and ocean wave breakers were consistent.

III.1.5 Objectives and outlines of this chapter

Overall, there is consensus that the evolution of the wave surface and accompanying dynamic impacts of breaking waves result from strongly time-dependent, nonlinear wave-wave and wave-structure interactions that are hard to predict. The broken wave produces violent, multiphase flow where entrapped air plays a significant role in wave dynamics. However, model tests often fail to simulate the effects of such air entrapments; hence, the measurement results

are in need of a reasonable interpretation in order to account for the "scale effect" prior to general use. On the other hand, previous studies that found the similarity bubble size distribution and in impact velocities of the bubbly flow between the laboratory and ocean measures are important because they imply the importance of bubbly flow kinematics during impact. Furthermore, laboratory scale experiments that measure impact velocities of aerated wave flows might be used to predict ocean waves' impact velocities after breaking. Moreover, velocities of impacting wave/water jet , once obtained, can be used to model breaking waves as well as interpret the dynamic properties of the impacting waves obtained from either laboratory or ocean scale measurement.

In this context, the present study used laboratory experiments to measure green water velocities and dynamic impacts of extreme ocean waves on a fixed deck structure in a deep ocean environment. The experiments were conducted in a large-scale ocean wave basin to simulate extreme ocean waves impinging on an offshore structure. The measurements for the overtopping green water velocities and impact pressures were made during wave impingements on a deck representing an offshore platform structure. The timely evolutions of the wave surface elevations across the basin were also observed. Using data obtained from these experiments, this study aims to:

(1) evaluate full-field velocity structures of green water waves over offshore structures,
(2) measure dynamic pressures of extreme ocean waves associated with present large-scale wave simulations, and
(3) examine correlations between wave kinematic energy and dynamic impact pressures.

The information from this study will be discussed in comparison to the results from the smaller scale laboratory experiments of Ryu (2006) and Ariyarathne et al. (2012). Through comparisons with smaller scale experiments with equivalent model layouts and initial wave conditions, this study provides physical insights for the scaling effects of dynamic and kinematic responses of laboratory scale violent waves. Ultimately, this study anticipates quantitative estimations for potential wave impacts on offshore structures associated with both kinematic and dynamic characteristics of extreme ocean waves.

In this chapter, section 3.2 describes the experimental setup, wave conditions simulating breaking ocean waves, and principles of measurement methods employed for velocity and pressure measurements. Section 3.3 provides the results and discussion on the kinematic information obtained from the BIV velocity measurements for overtopping green water waves

above a fixed deck structure. Section 3.4 provides the results and discussion on green water wave impacts based on measurements of dynamic pressures. The effect of a large scale measurement setup on the magnitude and rise time of impact pressures is also discussed. In Section 3.5 the correlation between the kinematic and dynamic properties of green water waves are investigated. Section 3.6 gives a discussion about the influence of the laboratory scaling needed to be considered for the interpretation and application of the experimental results. Section 3.6 is a summary and discussion for future studies.

III.2 Experimental method

The experiment was conducted in the deep ocean basin in the Offshore Technology Research Center (OTRC) at Texas A&M University. The wave basin is 45.7 m long, 30.5 m wide, and 5.8 m deep. The flap type wavemaker consists of 48 individually controlled paddles capable of generating a variety of wave conditions such as unidirectional and multidirectional regular and irregular (random) waves, long- and short-crested waves, and focused waves. Progressively expanded metal panels were installed on the opposite end of the basin to absorb wave energy and reduce wave reflection. A desktop computer used to transmit the programmed forcing signal for the wavemaker concurrently sent a step-shaped trigger signal to a data acquisition board connected to a second computer equipped with the NI-DAQmx driver and NI LabVIEW SignalExpress software. The time histories of the DC voltage output signal from six water surface elevation gauges, two pressures sensors, and one void ratio measurement were simultaneously collected through the data acquisition device. The data acquisition (DAQ; National Instruments, USB-6259 BNC) device collected up to 16 incoming analog signals with an aggregate maximum sampling rate of 1MS/s and provided the 8 analog input/output channels and two analog programmable function input (APFI) lines enabling the control by a trigger signal. The DAQ module was controlled by a second computer equipped with the NI-DAQmx driver and NI LabVIEW SignalExpress software and the self-architected LabView virtual interactive program was run to synchronize the initiation of the analog data log and to generate the trigger signal for the high speed camera with respect to the motion of the wavemaker.

A cuboid structure was built with Plexiglas to mimic the deck of an offshore platform and mounted on the offshore front of the mobile bridge spanning the basin. A square, self-illuminating LED panel was framed and sealed inside the Plexiglas structure for lighting effects as required for velocity measurement (discussed below). The LED panel has a luminous

emission of 2500 lx and is 0.65 m in length and width. Finally, the dimensions of the deck structure were 0.74 m by 0.74 m in length and width, and 0.10 m in thickness. The free board height was 0.26 m in the experiment. Figure III-1 shows the sketch of the model structure and the layout of the measurement points for wave elevation gauges, pressure sensors, and a probe for the void ratio (details discussed in next section). Note that the origin of the coordinate system (x,y,z) = (0,0,0) is fixed at the leading front, along the centerline, and on the surface of the deck. The offshore side edge of the deck (x = 0) is located about 20.9 m from the front face of the wavemaker across the basin (in x-direction), while the surface of the still water level (SWL) is at z = -0.26 m. Figure III-1 shows the position of the LED installation with respect to the deep ocean basin and SWL and illustrates the coordinate system used in this study.

III.2.1 Wave elevation measurement

The extreme waves were generated by the wave focusing technique. In this method, the wavemaker produces a train of waves of varying amplitudes and frequencies from 0.7 Hz to 1.3 Hz. The waves were generated so that short waves were followed by long waves; thus, the longer, more rapidly propagating waves generated later caught the slowly evolving shorter waves from behind. As a result, the waves superimpose and form a group of extreme waves consisting of a smaller number of steepened waves with greater amplitudes. Figure III-2(i) shows the mean displacement of the wavemaker by averaging 20 repetitions of the input signal used to generate the waves. The motion of the wavemaker has shown to be highly repeatable during wave generation. The temporal average of the standard deviation (i.e., average of the standard deviation at each time instance over about 40 seconds) of about 0.03cm during more than 20 repetitions. The wave group continues to increase height (or steepness) and break at a desired location. With some trial and error, the LED panel was positioned in close proximity behind the breaking point along the wave propagation. Wave propagation recordings from a digital hand camera confirmed that the extreme waves impacted the front face of the LED structure while breaking, hence the presence of the LED in the path of the breaking wave induced strong overtopping of the plunging breaker on the deck surface.

(a)

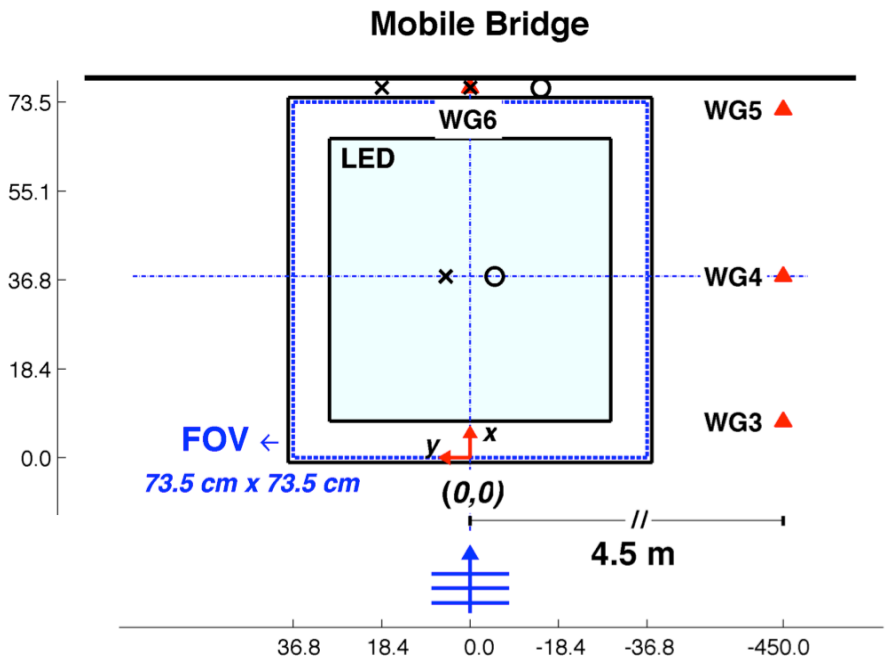

(b)

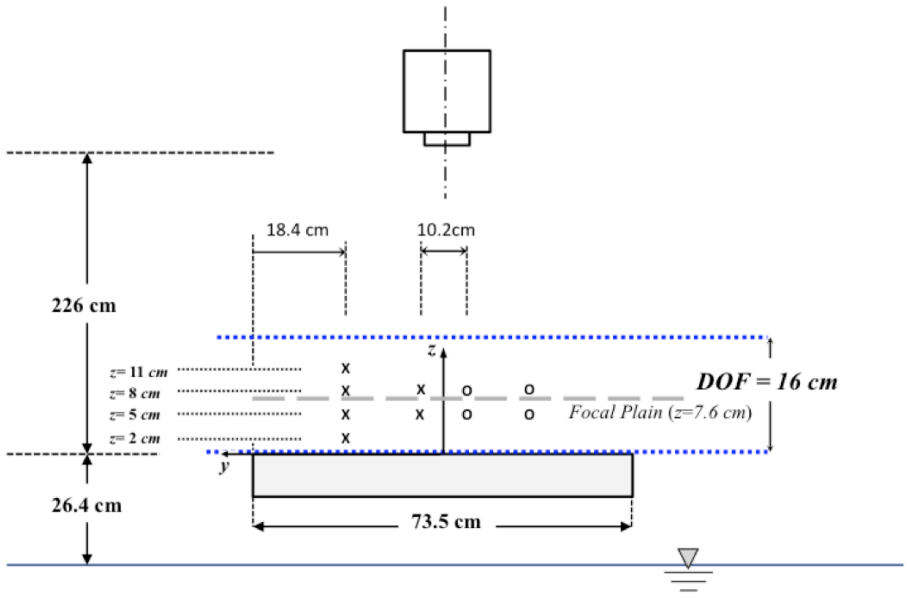

Figure III-1 Experimental setup. LED structure and layout of point-measurement gauges: (a) a plane view with measurement locations on horizontal plane for ×, pressure sensors; ▲, wave elevation probes; ○, FOR probes. Broken thick square delimits the FOV for BIV images, and (b) a vertical arrangement observed from the wavemaker. Dotted lines above the surface of LED denote the DOF with respect to the camera focal plane (a flat-dashed line).

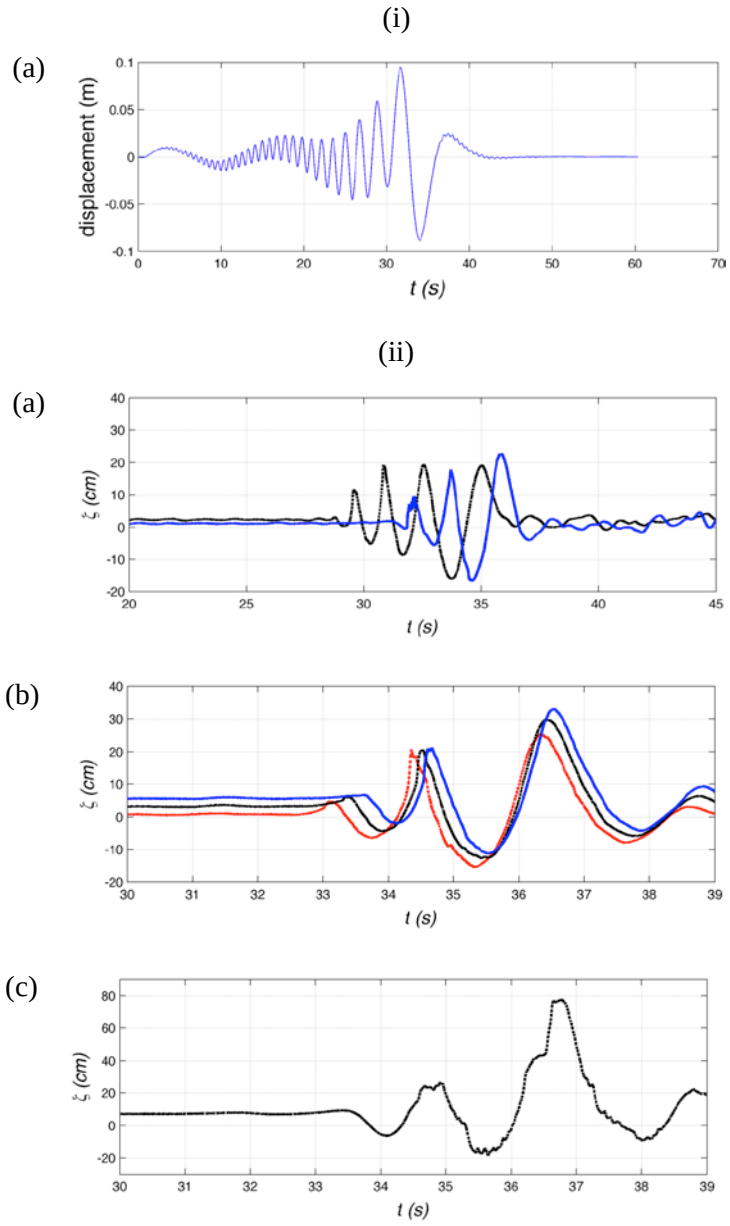

Figure III-2 Evolution of free surface elevation.(i) Displacement of a wavemaker flap during wave generation, (ii) instantaneous free surface elevations of focusing waves without the structure, and (iii) zoom-up of a mean free surface elevation near the mid-point of LED deck at WG04 (dotted) and calculated standard deviation (solid). (a) Incipient waves near wavemaker at WG01 (dashed) and WG02 (solid), (b) breaking waves surface evolution measured at 4.5 m aside from a structure aligned with the front edge, mid-point, and rear edge of the LED deck at WG03 (dashed-dot, red), WG04 (dashed, black), and WG05 (solid, blue), respectively, and (iii) overtopping wave flow above the LED deck. Arrow in (c) indicates a target wave and red dots shows the variation in wave surface elevations during the breaking process over repeated wave simulations. Note that vertical axes are scaled differently on each plot for better visualization.

(iii)

(a)

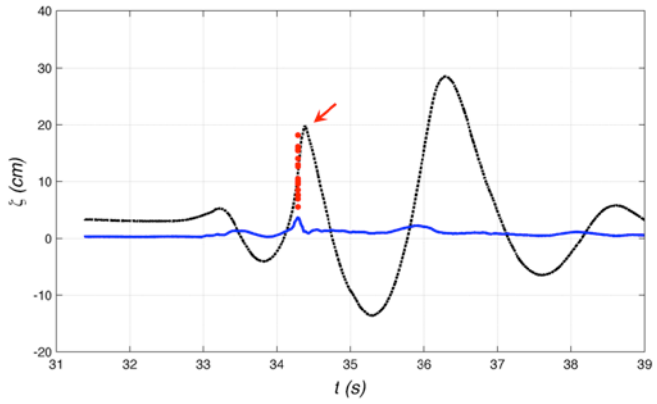

Figure III-2 Continued.

Double-wired, capacitance type wave elevation gauges were used to monitor and record the evolution of the wave surface elevations at six different locations along the wave propagation. The recordings of the wave elevations were started simultaneously 15 seconds after the initiation of the motion of the wavemaker. The time series of the analog output signals from the respective wave gauges were sent to the DAQ in volts and logged at a sampling rate of 10 kHz for 50 seconds. The calibration curves for the individual wave gauges were obtained upon installation and used for the conversion of output from volts to other units (i.e., cm)..

A minimum 20 minutes rest time was allowed between consecutive wave operations in order for the water surface to return to a quiescent state. The motion of the water surface was closely monitored and testing resumed when the standard deviation of the water surface displacement diminished to within a threshold limit of 1 cm.

Figure III-2 shows the evolution of free surface elevations of an instantaneous wave measured at various locations along the wave crossing direction, 4.5 m next to (in y direction) the deck structure. Table III-1 summarizes the locations of the respective measurements. The measurement points near the LED frame are also marked in Figure III-1a. Figure III-2a shows development of the focusing waves from the offshore gauges WG01 and WG02 where the wave surface continues evolving and superimposing. Consequently, the overlapped waves form a wave train consisting of two significant waves when it reached and broke near the LED deck (Figure III-2b). Figure III-2b shows a prominent turbulence and increased sharpness in a crest

of the first significant wave at WG03 (red, dotted line). This indicates that the wave is undergoing a breaking process within the area between WG03 and WG04. Review of video records has confirmed that a single wave-breaking event took place by the first significant wave (i.e., the first peak) near the location of WG03 and continued reforming at WG04 and so on. Furthermore, it is interesting to compare wave surface elevation at WG05 to the inundation depth of the overtopping flow above the surface of the LED frame recorded at WG06 (Figure III-2d): The vertical extent of the over flow becomes about twice as large as the surface elevation of the surrounding extreme waves, implying a significantly focused impact during the wave impingement.

This study investigates green water kinematics on the breaking overflow induced by the first impingement of an extreme wave, and specifically targetsthe first overtopping wave induced by the impingement of the violent breaking wave (indicated with an arrow in Figure III-2e). Overall, more than fifty waves were created during the entire experiment. Wave surface records from respective wave gauges have confirmed that the waves generated by the wave focusing technique produced accurately reproducible extreme waves.

The wave characteristics of the target wave were determined based on observation from WG04 aligned with the mid-point of the LED frame across the basin (Figure III-1a). This is based on the wave formation observed from WG03 through WG05 that showed more continuous evolution in the surface elevation after breaking, while the wave elevation at WG06 has shown to be intermittently large and affected by the presence of the LED frame. Furthermore, the fact that the WG04 was installed in close proximity to the pressure and void ratio measurement points and the mid-point of the velocity measurement field (details in section III.3 and III.4) also benefitted comparative investigation of the results.

The target wave has wave parameters, estimated based on zero up-crossing of the averaged free surface time-series record at WG04, as follows: wave period T =1.68 s, wave height H = 0.24 m, wave number k = 1.43 rad/m, phase speed C = 2.62 m/s, and wave steepness kA = 0.17 where the wave amplitude A is defined as H/2. The evaluation of the characteristic wave properties was based on the phase averaged surface elevation over 15 repeated wave elevation time series. Figure III-2e shows the time series of the mean (solid) and the standard deviation (dashed) of the wave surface elevation, respectively. Overall, the deviation in the surface elevation of the individual waves was shown to be fairly subtle with a standard deviation of 0.9 cm from its mean elevation, while the maximum deviation of 3.7 cm occurred during

overtopping of the target wave (i.e., the rise to the first peak surge). It may be worth mentioning that the deviation in the surface elevation at the occurrence of both peaks were as low as the standard error of 0.9 cm, indicating the maximum impact of the produced waves was reproducible. The largest deviation must be attributed by the increase in the turbulence level and irregularity in formation of the wave surface shape during the wave breaking process.

Table III-1 Measurement locations

Measurements	Distance from wavemaker (m)	Positions x (cm)	y (cm)	z (cm)
WG01	15.28	-564	450	-
WG02	18.28	-264	450	-
WG03	20.99	7.5	450	-
WG04	21.29	37.5	450	-
WG05	21.64	72.0	450	-
WG06	21.65	73.5	0	-
PM2 – PM11	21.29	36.8	5.1	2,5,8,11
PC2 – PC11	21.65	73.5	0	2,5,8,11
PS2 – PS11	21.65	73.5	18.4	2,5,8,11
VS5, VS8	21.65	73.5	-18.4	5,8
VM5, VM8	21.28	36.8	-5.1	5,8

III.2.2 Velocity measurements

The present study employed the BIV technique to investigate green water kinematics during wave impingement on a deck-shape structure. BIV images were taken using a high-speed camera (Vision Research, Phantom 5.1) equipped with a Nikon 50 mm micro focal lens. The output

images have 1024 x 1024 pixels of resolution that covered 0.74×0.74 m^2 of a field of view (FOV, Figure III-1a) on an LED deck surface. The images were obtained at a sampling rate of 1000 fps 2 second periods, focusing on the moment when the first overtopping occurred. In highly aerated regions, the bubbles clog together producing dark shadow plumes on BIV images. In order to brighten and increase gradients in textures, a second light (a 600 W regular light bulb) was installed alongside the camera tilted to face down toward the surface of the LED deck.

The BIV technique traces air bubbles as seeding particles without using a laser light sheet. Hence, the measurement planes at the air-water interfaces appear sharp and focused as determined by adjusting a depth of field (DOF). The objects (i.e., air bubbles and water droplets in this case) within the DOF carry predominant weight, against those outside the DOF, in the displacement correlation process for velocity determination. The DOF is controlled by adjusting the camera aperture and the distance to the focal point on the objects from a lens front surface. The DOF varies between the farthest limit S and the nearest limit R, defined as $S = lf^2/(f^2 - N_c l C_c)$ and $R = lf^2/(f^2 + N_c l C_c)$, according to the approximation presented in Ray (2002). Here, l is the distance between the camera and the focal plane, f_c is the camera focal length, C_c is a circle of confusion of a lens, and N_c is an f-number for a camera aperture. The objects outside the DOF appear blurry and have no effect on correlations in the displacement of moving particles captured by two consecutive images (Ryu et al., 2005). Accordingly, the uncertainty in position of the observed objects, or air bubbles, on a BIV image is one half the thickness of the DOF. Therefore, the error in the computed displacements of a particle due to the uncertainty in its position within the DOF can be estimated as $\varepsilon = D/2l$. In other words, the error decreases with distance and with sharper (i.e., narrower) adjustment of the DOF. More details about the principles of the BIV technique and discussions of error estimation can be found in Ryu et al. (2005).

In the present study, the camera was installed 2.26 m above the deck structure focusing down on a horizontal plane at z = 7.6 cm from the deck surface. Hence, with l = 2184 mm, f = 50 mm, C_c = 0.03 mm, and N = 1.4, DOF is D = 0.16 m and the subsequent error is approximately 3.7%. Figure III-1b shows the layout of the BIV system and the DOF image measurements. In the present study, a total of 18 sets of quality BIV images have been obtained and analyzed for instantaneous velocity calculations.

Raw images were first inverted in order to make the bubble area bright (high gray scale values) . Two inverted images of every other frame in sequence of the original BIV records were

selected and stitched together to generate a single frame, coupled image. Hence, the displacement cross correlations were made within a coupled single image with a sampling rate of 2 ms^{-1}. Commercial software from La Vision, Inc. (*Davis 5.2*) was used to analyze BIV images and obtain particle displacement vectors. An adaptive multi-pass algorithm was employed with decreasing window sizes of initially 64×64 pixels and finally 32×32 pixels. The adjacent windows were shifted with 50% overlaps for every passage. By reemploying the displacement calculated from the first pass to the second pass, the signal to noise ratio was improved, reducing the chance of errors in correlation. Finally, the numeric results from the displacement correlations were used as input (i.e., raw data) for instantaneous velocity calculations and subsequent post processing to evaluate green water kinematics. The BIV performs well only with sufficiently aerated flow fields containing a fair amount of air bubbles to trace. Therefore, the velocity results presented in this study and during the following discussion focus mainly on the wave impingement moments when the flow became a highly turbulent air-water mixture. This is also when the flow field become violent and the kinematic energy of the overtopping waves became critically important.

III.2.3 Pressure measurements

Pressure measurements were taken on two different vertical planes on the cross sections (xz-plane) orthogonal to the wave propagation direction above the deck surface. The first is located at a mid-point of the x directional extent of the deck along the centerline, hence located at $x = L/2$ and $y = 0$. The pressure measurements on this plane were named PMz, where *z* indicates the position of each gauge above the surface. The second measurement plane is located at the rearof the deck at x = *L*. On this plane pressure measurements were taken at two separate locations in y: y=0 (on a centerline) and y = L/4 (on a semi-centerline). Those gauges were named PCz and PSz, respectively. For each plane, four measurement points were selected along the vertical z direction with 3 *cm* spacing between neighboring locations starting from 2 *cm* above the surface: $z = 2$ *cm*, 5 *cm*, 8 *cm*, and 11 *cm*. Based on the observation of the wave elevations in time (Figure III-2), the maximum inundation depth during the overtopping period of a target wave was estimated to be approximately 16 *cm* above the deck surface. Therefore, the pressure sensor deployments must have provided sufficient coverage over the vertical extent within the wave inundation depth. Each pressure sensor had a head size of 1 cm in diameter. During the measurements, a pair of sensors, 3 *cm* apart from each other, were mounted together on a thin

aluminum beam of 2.5 cm in width and 0.8 cm in thickness, facing toward the incoming waves. The pressure sensors were initially kept dry at each wave run and measured the wave impact pressures coming perpendicularly to the surface of the sensor head. Therefore, the pressure measurements are believed to measure impact pressures, primarily due to wave flows propagating along a positive x direction at the height of the sensors.

Pressure measurements were made using two piezo-resistive pressure sensors (Kistler type 4053A1) that measure pressure relative to the surrounding atmosphere . The pressure sensors have a natural frequency above 15 kHz and a capable pressure limit of 1 bar ($\approx 100kPa$). Pressure measurements were taken at a sampling rate of 10 kHz. Before installation, each pressure sensor was calibrated by measuring the voltage outputs reading hydrostatic pressures under a water column of varying head depths from zero to 105 cm. The resulting calibration curves have shown linear relations between the voltage signal and calculated water head pressure in *Pa* unit. Hence, the calibration curve for pressure sensors was determined to be $P = 10.18I - 0.50$ for sensor 1 and $P = 16.20I + 1.92$ for sensor 2. Here, *I* is a signal output in *Volt* and P is equivalent hydrostatic pressure under water in *kPA.* The standard error in either gauge was 0.02 kPa per volt.

The pressure data was collected with a minimum of 5 repetitions (up to 13 repetitions) at individual measurement points. The number of collections was based on Ariyarathne et al. (2012), who investigated the green water impact pressure on a deck structure using the same pressure sensors: Ariyarathne et al. (2012) observed that the pressure time history from averaging over five repetitions were almost identical to those from the average of 10 repetitions. The mean pressure time series was also found successfully capturing the pressure peak. Therefore, the pressure timeseries was repeatedly collected at least 5 times per location for this study.

III.3 Green water wave kinematics

III.3.1 Velocity structures of overtopping waves: instantaneous velocity fields

The instantaneous velocity fields obtained from analysis of BIV images over repeated tests were first examined in order to understand overall flow patterns of overtopping green water waves on the structure. As observed from the wave elevation records in Figure III-2, evolutions of the focusing waves have shown close similarity in shape between repeated wave simulations. However, the shape of the wave front and evolution of the flow structures of the overtopping

waves have shown substantial variance between the wave operations, depending on the breaker conditions during the wave impingement. For example, Figure III-3 presents sequences of instantaneous velocity fields normalized by the phase speed of *C* and flow structures obtained from the BIV analysis. The flow fields presented in each column of Figure III-3 demonstrate distinct shapes and propagation patterns of the overtopping wave flow above the deck surface. The BIV images are listed from top to bottom to show the evolution of flow structures at various time instances during the passage of overtopping wave fronts since it reached the frontal edge of the deck at t = 0.00 s (not presented).

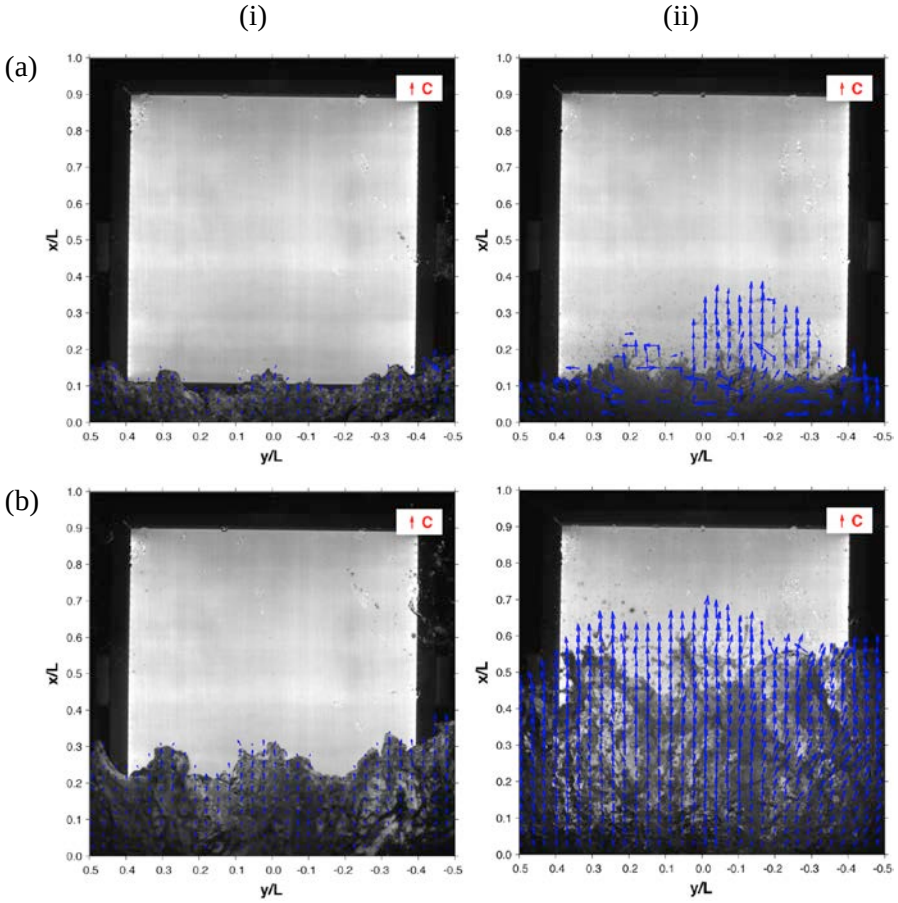

Figure III-3 Typical frontal shapes and velocity distributions of overtopping wave flows. Instantaneous velocity fields due to waves (i) breaking on deck surface during overtopping and (ii) breaking on front face of deck in advance of overtopping, respectively. t = (a) 0.06 s, (b) 0.14 s, (c) 0.22 s, (d) 0.30 s, and (e) 0.38 s. Background images arbitrarily selected from instantaneous tests.

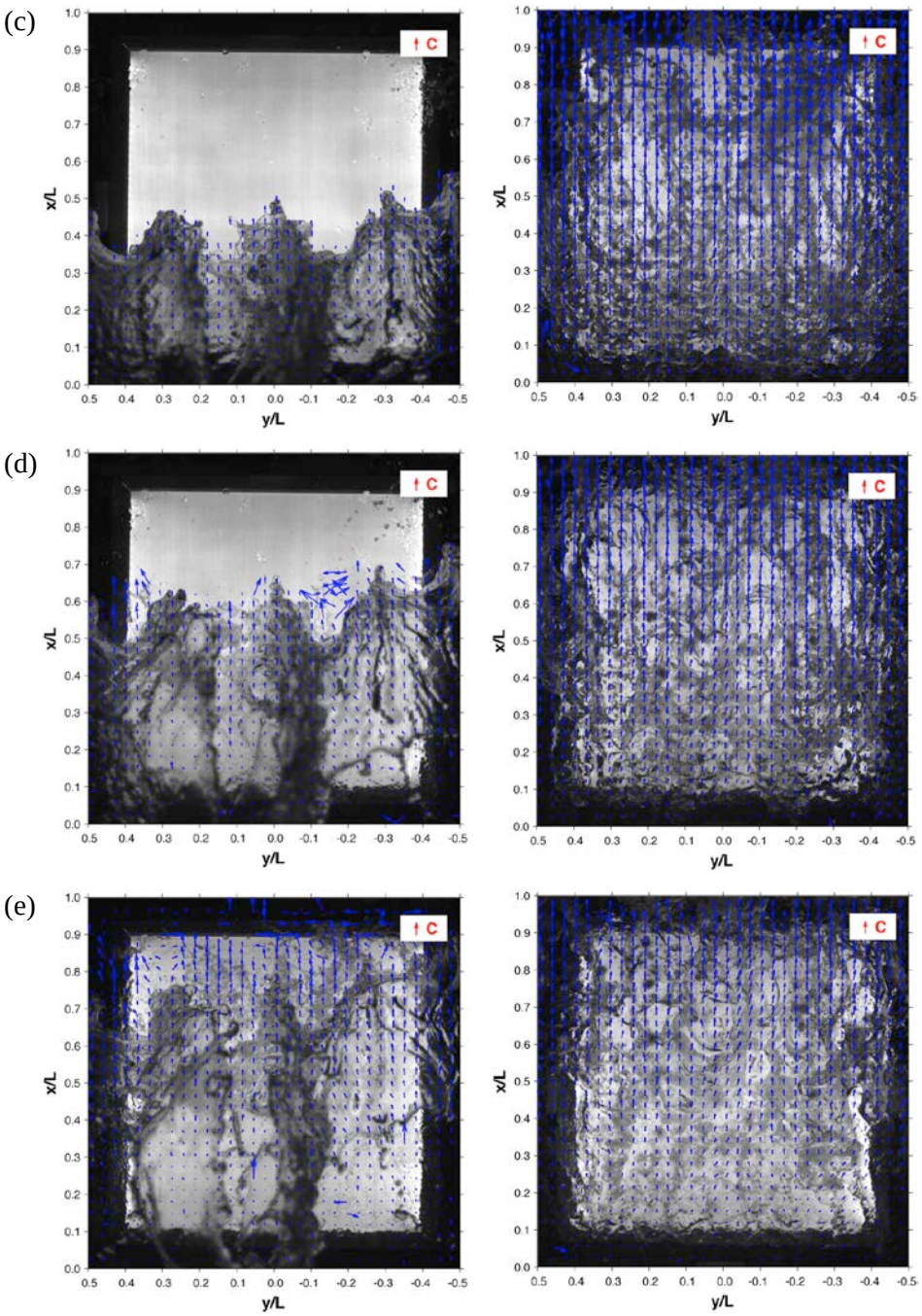

Figure III-3 Continued.

When the wave reached the structure before breaking and plunged on a surface of the deck, the speed of the overtopping wave increased gradually in a predominantly x direction (type 1;

left column in Figure III-3). In this case, the wave developed a leading front whose positions distributed continuously but with significant gradient along the orthogonal y direction. It was also observed that the flow tends to propagate faster along the centerline and semi-centerlines, respectively, until the flow speed in front has reached close to *C* and undergone the plunging breaking on a rear portion of the deck surface (Figure III-3d and Figure III-3e, left). Once it breaks, the flow structures near the leading front became turbulent and flow speeds quickly increased in the front. However, by this time, the velocities of the rear inundation flow decreased significantly, presumably due to the decreased momentum flux of incoming waves. On the other hand, in a case when waves first impinged on the frontal edge of the structure in advance of rushing to the deck surface, the overtopping flow formed splashing jets from breaking waves (Figure III-3b in a right column). The broken jet flows propagated rapidly and leading positions of the initial overflow varied widely between tests depending on the flow orientation after wave impingement. Note that the splashing wave front reached the rear edge of the deck at t=0.22 s after the initiation of the wave impingement (t = 0 s), while the slower waves shown in the left columns of Figure III-3 barely passed 0.5*L* in x direction at that same moment. This comparison further implies the influence of wave impingement conditions on both the temporal and special evolution of velocity fields and the duration over which the momentum flux of overtopping waves impacts the structure.

III.3.2 Mean flow field by BIV

The evolutions of impacting green water waves were quantitatively evaluated by investigating the temporal and spatial distributions of mean flow velocities. In order to calculate the mean velocities, 18 sets of instantaneous velocities obtained from 18 measurements were carefully synchronized by defining the time t=0 as a moment when the wave front crossed the front edge of the deck structure (i.e., x = 0 in figure 1). When phase- averaged, the mean velocity fields calculated from the raw instantaneous velocity data contained erroneous vectors scattered in irrelevant regions to the realistic flow field. Two sources of errors were presumed to produce erroneous vectors in the mean velocity computations: scattering due to either the background noise in the BIV images or gradients in lighting outside the illuminated LED area, near the boundary of the frame; or randomly produced droplets from outside the FOV and irrelevant to the target waves. In order to get rid of spurious error vectors, masking images were manually produced for individual BIV measurements based on both the flow field shown in each

instantaneous BIV image and velocity distribution at selected times based on the raw velocity data. Subsequently, the erroneous vectors present in the raw instantaneous velocity fields were masked and filtered instantaneous velocity data was obtained at every 0.02 s from the moment of t=0 to t=0.30s when the wave fronts reached the rear edge of the deck. On the other hand, the masking images were produced carefully so as not to remove the splashing jet generated during the wave breaking, as it is a characteristic of impacting green water flow.

As discussed earlier, the breaking wave front largely increases the randomness in the propagation velocities of splashing water and wave impingement conditions affect the evolution of velocity fields behind the overtopping wave flow. Examinations of BIV images from 18 repeated measurements show that 14 waves have breaking front shapes that produced splashing jets over the deck surface at the beginning of the run-up process. Therefore, some instantaneous velocity fields of slowly proceeding deck impingements did not contain velocity vectors for the rear portion of the deck surface for about the first 0.20*s*, while the splashing jet flow reached the end point of the deck and developed violent velocity fields at the same moment.

The effect of the initial shapes and wave impingement conditions on developments of the following green water velocity fields is demonstrated in Figure III-3 by comparing the formation of the velocity fields shown in the respective columns at the corresponding time . This means that the evaluation of mean velocities needs to also account for the number of flows present at a certain location at a moment of interest during early stages of flow run-up. Therefore, the mean velocities were calculated by averaging the number of instantaneous vector components present at a location of interest (i.e., inundated flow field on the surface on the deck) at corresponding times over repeated velocity measurements.

Furthermore, a threshold limit was given for the minimum number of velocity vector components required for evaluating a mean flow velocity at a given point. In this way, some spurious errors that are rarely shown in overall instantaneous velocity fields could be removed. After trial and error, the threshold limit N was determined as N = 12 (70 percent of the total number of repetitions), hence the mean velocity fields were obtained by taking the average of at least 12 instantaneous velocity values present in each time and location. The phase-averaged mean velocities are calculated as:

$$\begin{aligned} &\frac{1}{n}\sum_{l=1}^{n} u_k^l = U_k \qquad \textit{if and only if } n \geq 12, \textit{ and} \\ &0 \ (\textit{no value}) \qquad \textit{elsewhere} \end{aligned} \tag{20}$$

Here, u_k^l is the k-component velocity at l^{th} instantaneous velocity measurements, n is the total number of repetitions (realizations) accounted for the averaged velocity calculations, and U_k is the phase-averaged mean velocity. The effect of the minimum amount of data used for averaging the computed mean velocity fields is discussed further in section III.3.4.

Figure III-4 shows evolutions of mean velocity fields normalized by the phase speed of *C*. The mean velocities were plotted on arbitrarily selected background images from one of 18 repetitions. The time t=0 was defined as the moment when the wave front reached the front edge of the deck at x = 0. The mean velocity values shown in the velocity maps are the average of a minimum of 12 instant velocity realizations. Note that the mean velocity fields presented in Figure III-4 are direct results from the averaging process: no smoothing or filtering was done, thus preserving the nature of the breaking wave flow, such as irregularities and randomness in velocity distributions along the leading front of breaking waves.

In addition, Figure III-5 provides quantitative descriptions of the flow structure and spatial variation in mean velocities over the run-up periods observed in Figure III-4. The evolution of the flow structures during wave overtopping is mostly determined by variation in the x direction velocity component U. Therefore, the local variability of the mean velocity fields of U at times corresponding to the velocity map in Figure III-4 is investigated and presented in each plot in Figure III-5. In order to evaluate the local mean flow, the flow field within FOV was first divided into 10 horizontal (y direction) and cross directional (x direction) sections . The individual local windows are 7×7 cm^2 in and contain up to 6×6 velocity points. The local mean velocities were calculated by averaging the mean velocity vectors contained in the local window in time. The local mean velocities presented in Figure III-5 were scaled by *C* and plotted against the center positions of each local window with respect to *y/L*.

In Figure III-4a, the wave front appears within the FOV of the horizontal surface of the deck. During this moment, the wave rushed upward and its wave front crossed the leading edge of the deck. The velocities in the propagating direction (i.e., in x direction) gradually increase from initially below 0.5*C* near the lead edge of the deck up to about 1.0*C* in the wave front at t = 0.06 (Figure III-4b). This indicates that the upward motion of the overtopping flows have become transient to horizontal flows within this flow regime. The positions of the wave front maintain relatively uniform distribution along the orthogonal y direction. During the passage of the wave front over the second third extent of the deck in x direction ($0.3L < x < 0.7L$), more significant variation in propagation velocities U can be observed along the wave crossing direction in

Figure III-4c ~ Figure III-4e. The wave front velocities rapidly increase from around 1.0*C* at t=0.04 to 1.4*C* when the wave front passes x = 0.5*L* *t* = 0.14 *s* (Figure III-5c).

The orientations of velocity vectors commonly become a positive x even in a turbulent wave front. This may imply that the x direction component of the overtopping flow would produce dominant effects during wave impacts on a vertical plane above the deck surface. On the other hand, the flow velocities on the front portion of the deck at x<0.3*L* tend to maintain constant velocities until t=0.10s and then gradually decrease while the wave front continues propagating. Flow velocity behind the wave front tends to decrease from *U*=0.7C at *x* =0.2*L* to *U*=0.6*C* at x =0.2L toward 0.4*C* at *x* = 0.1*L* close to the front edge (Figure III-5b). It is also interesting to note that the increases in propagation speed of frontal velocities start earlier from the flows near the center of the deck width (y = 0) from t = 0s to t = 0.06s. As a result, a protruded leading front develops along the centerlines of the deck at x = 0.5*L*. However, the speed of the frontal velocities near center points begin to stop increasing at *U* = 1.4*C* at around *t*=0.06s (Figure III-4c and Figure III-5b). Meanwhile, the flow alongside the centerline continues increasing up to 1.4*C* until a majority of the wave front reaches the rear (*x*=L) of the deck surface at *t*=0.22s (Figure III-4f and Figure III-5f). Consequently, the propagating speed of the frontal flow along the semi-centerlines ($y = \pm 0.25L$) exceeds that of previous leading front velocities along the centerlines at between *t*=0.14*s* and *t*=0.18*s* (Figure III-4d and 4e). As a result, the wave frontal distribution over the deck span becomes widely uniform when the wave front is aligned close to x=0.65*L* (Figure III-4d).

In Figure III-4e, flow velocities alongside the centerlines exceed the front-most centerline velocities and reach the end of the deck earlier. Once the wave overflow reaches the end point of the deck (Figure III-4f), the flow field maintains a uniform decrease in speed, while the flow direction is dominantly oriented toward positive x direction (Figure III-4f and Figure III-4g). The overall flow speed including the wave front velocity also decreases, especially right after the wave front reaches *x*=*L* (as demonstrated in Figure III-5f – 5h). Such seemingly steady flow structures start changing about 0.08 seconds after the flow speed in x direction decreases substantially, mainly due to the weakened influx flow, and inundation outflow above the deck starts departing from the deck surface toward the side of the structure (Figure III-4h).

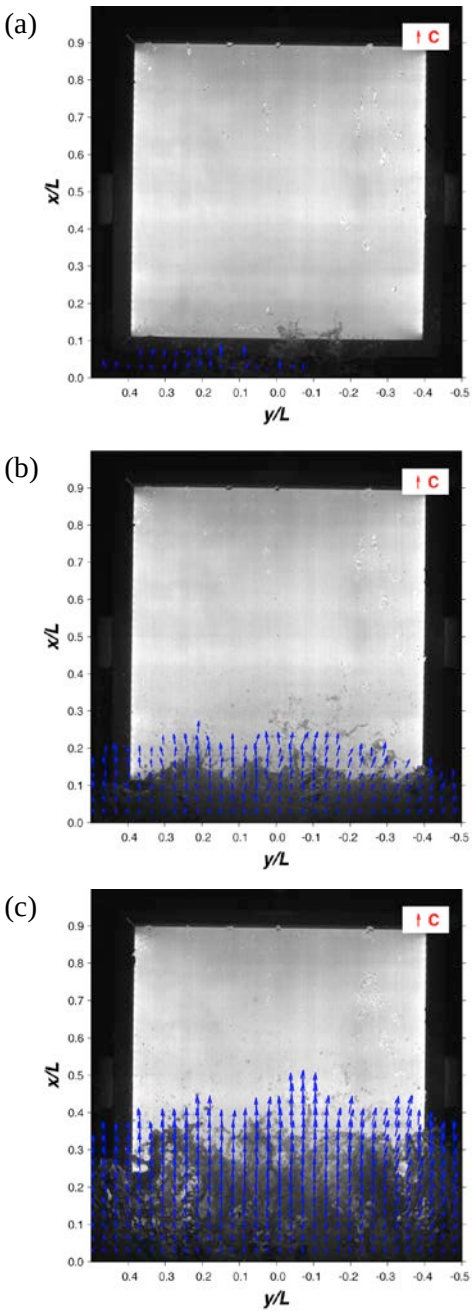

Figure III-4 Mean velocity fields on a horizontal plane over the deck surface. *t* = (a) 0.02 s, (b) 0.06 s, (c) 0.10 s, (d) 0.14 s, (e) 0.18 s, (f) 0.22 s, (g) 0.26 s, (h) 0.30 s.

(d)

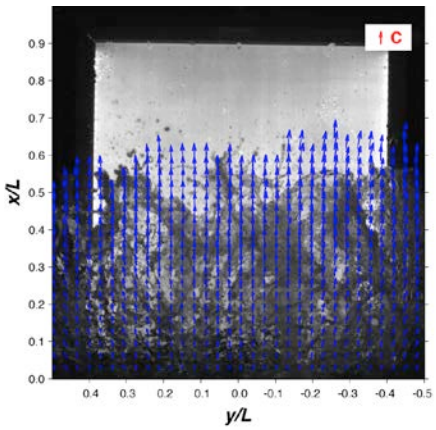

(e)

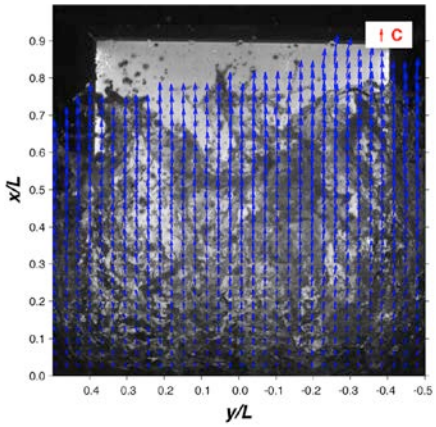

(f)

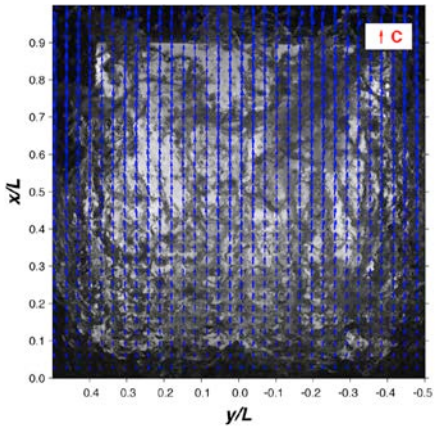

Figure III-4 Continued

(g)

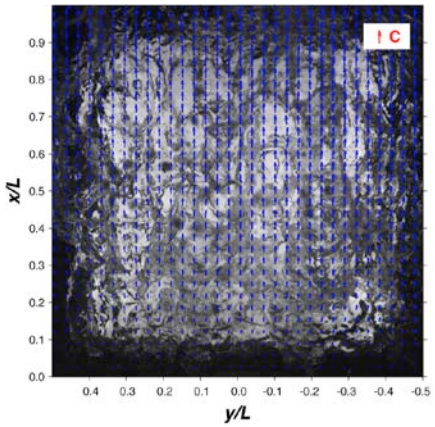

(h)

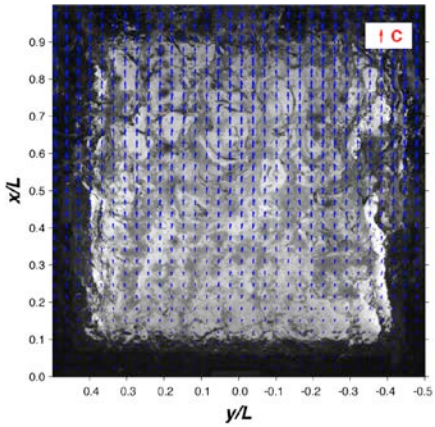

Figure III-4 Continued

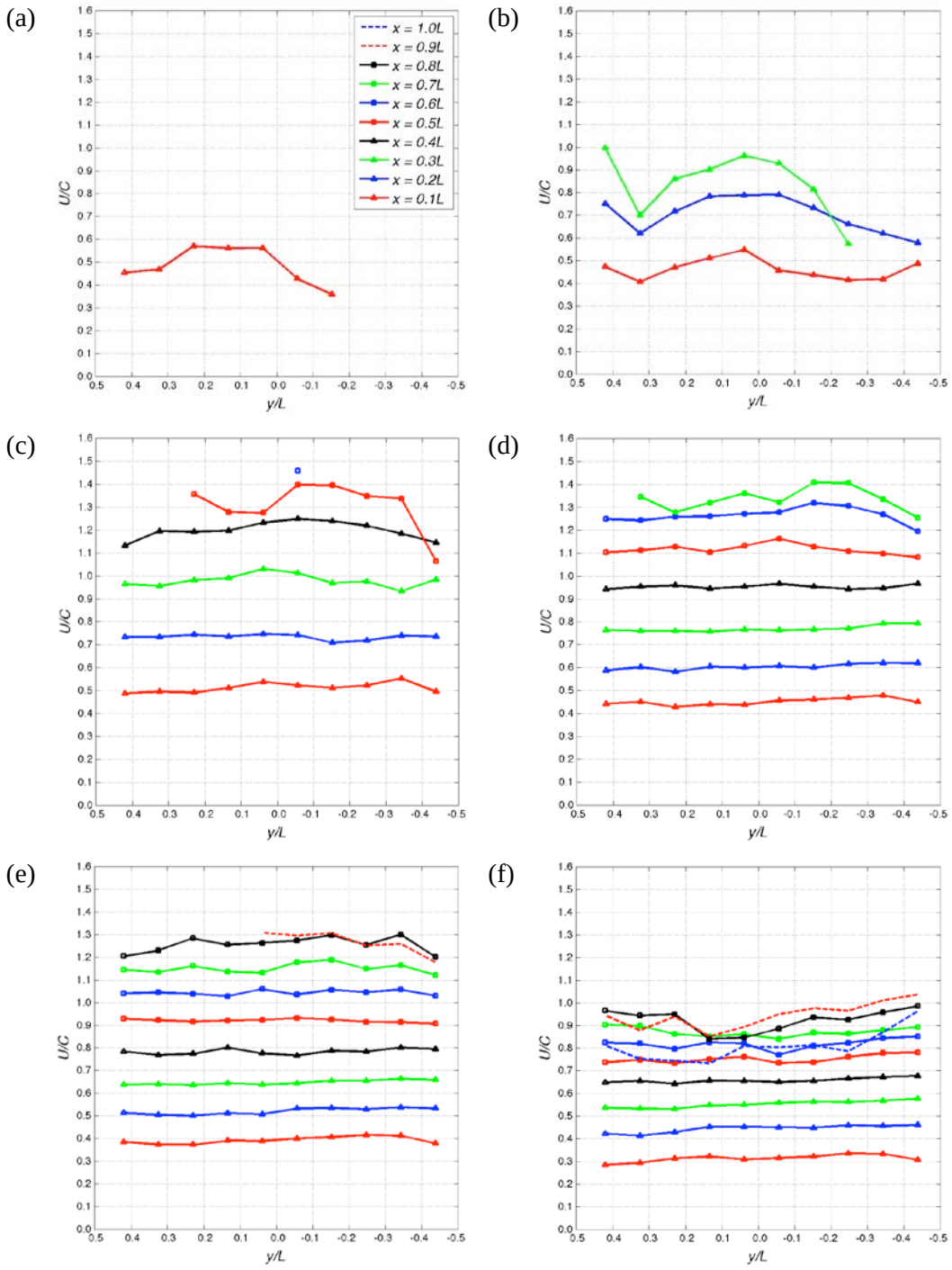

Figure III-5 Spatial distributions of locally averaged x direction velocity. The local mean velocities are obtained by average x-direction mean velocities observed within 7×7 cm^2 local windows. The upper limits of respective local windows are at x = 0.1L, x = 0.2L, x = 0.3L, x = 0.4L, x = 0.5L, x = 0.6L, x = 0.7L, x = 0.8L, x = 0.9, x = 1.0L. t = (a) 0.02 s, (b) 0.06 s, (c) 0.10 s, (d) 0.14 s, (e) 0.18 s, (f) 0.22 s, (g) 0.26 s, (h) 0.30 s.

(g) 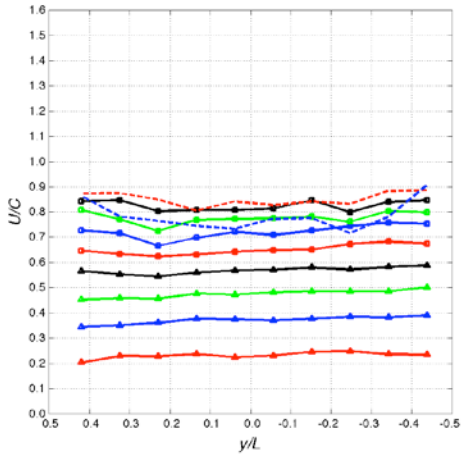

(h) 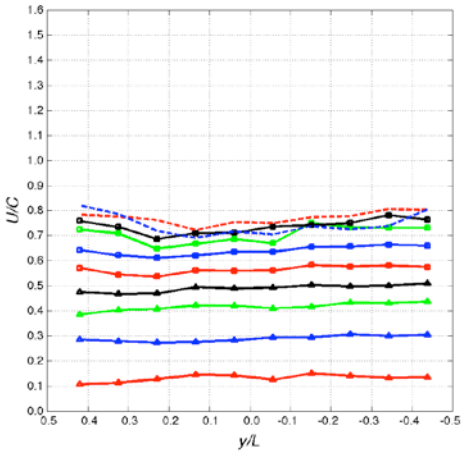

Figure III-5 Continued

In sum, the spatial variability of the mean flow structures is most significant in a wave front during early stages of the wave run-up as observed in both the instantaneous BIV images and computed mean flow velocity maps. The wave overtopping flow propagates with a protruding wave front near the center of the deck span that increases its speed in the x direction until it passes about half the x direction extent of the deck (x = 0.5*L*, Figure III-5a -5b). Increases in propagating speed cease from the center flow near y=0 (Figure III-5c) when it reaches its local maximum speed of 1.4*C*. Meanwhile, the flows alongside the semi-centerlines increase further until they pass the protruded wave front near the center and reached the local maximum velocity 1.4*C* just after passing $x = 0.7L$. Consequently, the distribution of maximum velocities of the mean flow along the y direction becomes fairly uniform with a slightly pronounced front face along $y = \pm 0.25L$ near the end of the deck (Figure III-5d-5e). Once the frontal flow of the overtopping wave has passed the back edge and starts leaving the deck surface, the flow velocity begins to decrease. The decrease in velocity starts immediately after the outflow of the green water waves starts. The decrease in velocity is abrupt in the flow aligned near the back edge of the deck within $x>0.7L$ (Figure III-5f -5h). Note that the distribution of maximum velocities of the mean flow along the y direction corresponds to the average line of the wave front position until $x<0.7L$. Presumably, such rapid recession must be because the mostly horizontal momentum of wave overflow on the deck surface is being converted to downward, vertical momentum as the flow exits the deck. Similar patterns have been observed from the green water velocity evaluations from smaller-scale experiments of a two-dimensional study by

Ryu et al. (2007b) and a three-dimensional study by Chang et al. (2011). Once the primary front of the overtopping wave passes the end of the structure, the x component velocities, and hence the propagating speed of following inundation flows, gradually decreases to less than 1C after 0.22 s since the initiation of the overtopping event.

III.3.3 Evolution of averaged local flow and cross-sectional maximum velocities

The rate of local variation in mean flow structure and its dependence on the extent to which the wave front has passed are characterized by analyzing the temporal and spatial evolution of flow velocities across the dominant x direction. The variability of cross-sectional flow velocities produces timing dependent kinematic impact on a vertical plane orthogonal to the flow direction. Therefore, variations of the maximum flow velocity U_C are investigated along the wave crossing direction with regard to the position and speed of the wave front. Figure III-6 shows maximum U velocities measured at various locations distributed regularly across the deck ($0 < x < L$). The maximum cross sectional velocity U_C is defined as a maximum value of the x direction velocity U within a row dividing the x direction extent of the deck surface into 10 parallel windows of 0.1L in depth. Note that the ending points of each line indicate locations of the wave front at respective time instances. The cross sectional velocity is a maximum of U_C=1.58C (4.08 *m/s*) at x=0.65L in front of the flow. At that moment, the flow velocities are highest in the front-most area. On the other hand, overall flow velocities tend to decrease over time with higher rates of decrease during the early overtopping period (when t<0.16 s): rates of velocity increase over space decay with time. Most significant velocity drops are observed in the wave fronts once they pass the highest velocity point (x = 0.65L) until they reach the end of the deck surface at x = 1.0L. Such velocity drops are not observed for the cross-sectional velocities of the low speed flows dominating after the primary frontal flow of overtopping waves exits the deck surface area. In fact, they seem to never reach maximum within the extent of the longitudinal length of the deck.

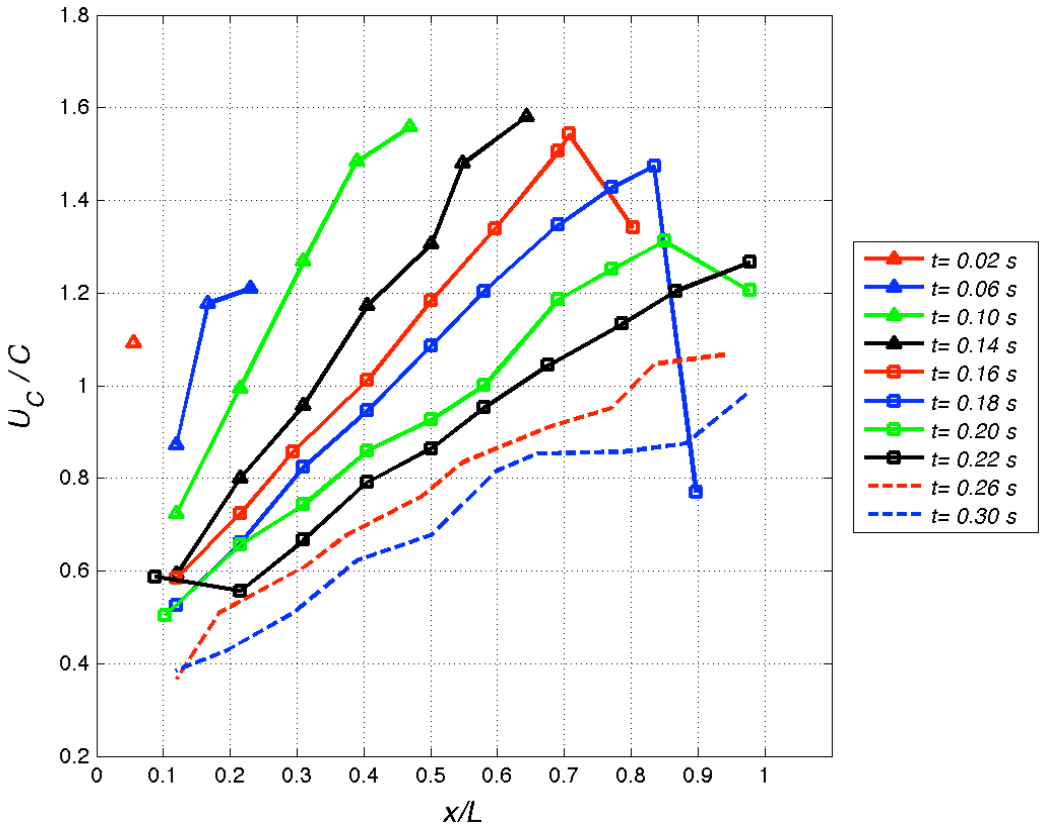

Figure III-6 Maximum cross sectional velocities U_C. U_C is a maximum x direction velocity measured within respective row windows spanning total width of the deck surface. Individual rows have 0.1*L* in depth. Each line in the plot is computed every 0.04 *second* corresponding to the velocity maps in Figure II-4. Exceptions are for additional plots at t = 0.16 s and 0.20 *s*. The upper limits of respective local windows are at $x = 0.1L$, $x = 0.2L$, $x = 0.3L$, $x = 0.4L$, $x = 0.5L$, $x = 0.6L$, $x = 0.7L$, $x = 0.8L$, $x = 0.9$, $x = 1.0L$.

Temporal variation in the maximum cross sectional velocities, and hence the maximum x direction velocity in time U_M, are investigated. In Figure III-7, the maximum cross sectional velocities are plotted with respect to duration since t = 0 when the wave front first crosses the front edge of the deck. Figure III-7 also shows the locations of both the wave front and maximum velocity points at respective time instances where the information was available. The velocities and locations are scaled by *C* and *L*, respectively. The time t is normalized by a wave period *T* for comparison with the wave characteristics. Clearly, the maximum velocity occurs at $t = 0.08T$ (0.14 *s*) with $U_M = 1.58C$. This is when the wave front is about to pass the line $x = 0.65L$ and start decreasing velocity. The comparison of the positions of the wave front to that of the

maximum velocity locations shows that maximum flow speed occurs in frontal flows in the initial stages of the overtopping period. However, the delay of the flow speed in the front takes place from about t = 0.1*T*. Accordingly, there is a hump in the timeseries of the maximum velocities at t = 0.13*T*, indicating that the flow that reaches the rear edge first (U_M = 1.3*C*) would not be the maximum velocity over the field: in fact, those with higher speed may arrive slightly later at about 0.01*T*(0.02 *s*), as presumed by the increased maximum flow speed at t = 0.15*T*.

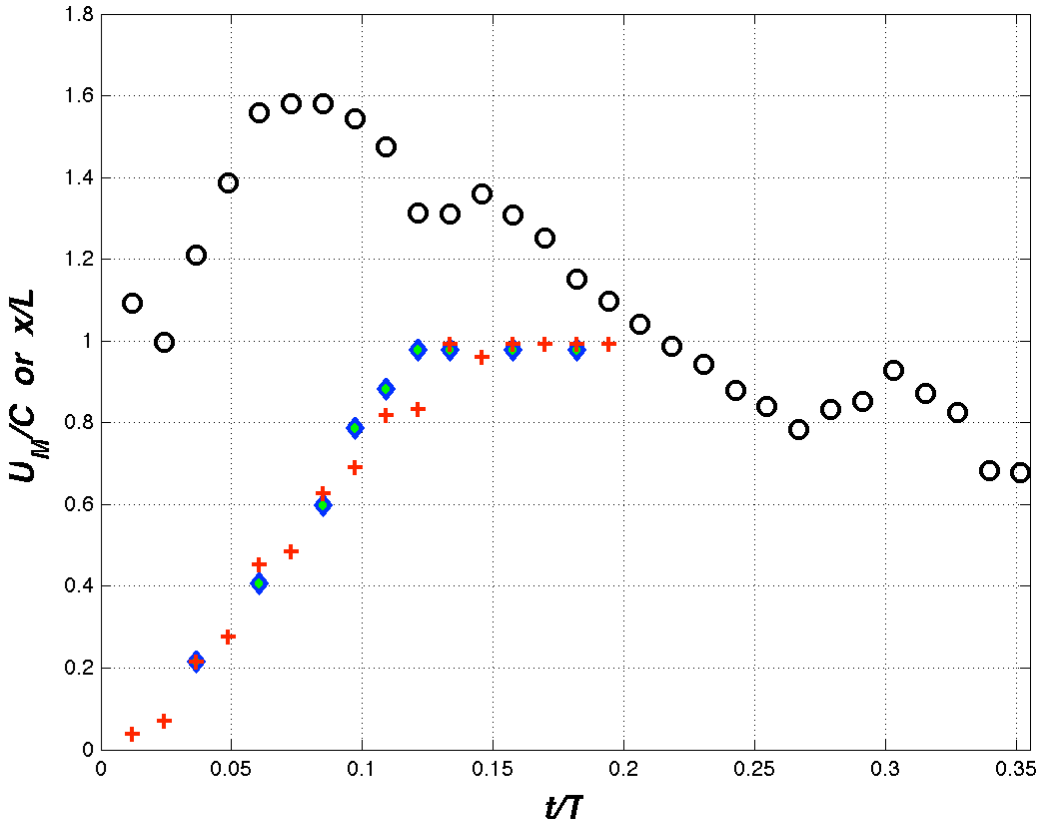

Figure III-7 Temporal variations in maximum cross sectional velocities. ○: Maximum cross sectional velocities in time, ◆: locations of the wave front, and +: locations of U_M. U_M are calculated with 20 *ms* time interval.

Ryu (2006) has proposed a prediction model for U_C accounting for a nonlinear profile of cross sectional horizontal velocities in time and space, defined as:

$$\frac{U_C}{U_M} + b\frac{t}{T} = a\left(\frac{x}{Ct}\right)^n \tag{21}$$

The scaled parameters $\mathbf{U_C/U_M}$, $\mathbf{x/Ct}$, and t/T were introduced as measures for the cross sectional horizontal velocities, the downstream extent of the wave propagation, and the overtopping period. Here, a, b, and n are empirical coefficients determining a fitting curve for a similarity profile for U_C. Based on the observed variation in $\mathbf{U_C/U_M}$ and $\mathbf{x/Ct}$ in time, the model accounts for the nonlinear relationship of horizontal flow velocities with time and space (i.e., location) during the wave overtopping period. Figure III-8 shows the similarity profile obtained from data presented in Figure III-6. The values for the empirical coefficients for the curve fit are a = 0.83, b = -0.32, and n = 0.58 and the R-square value is 0.77. The fitted data is from the horizontal velocity profile shown in Figure III-6 obtained from a moment when the green water wave started run-up at $t = 0$ until the wave front passed the rear edge of the deck at $t = 0.13T$. Compared against the linear regression (a dashed line), overall data is surprisingly well fitted along the curve, indicating a strong nonlinear relationship between two scaled parameters. The most prominent outliers are those obtained either at the early stage of the wave run-up ($t \le 0.04T$) or later when the wave front has arrived at the far edge of the deck ($t \approx 0.10T$). They are both when the momentum exchange takes place between the dominant horizontal propagating flow and either upward entering flow or downward exiting flow. Therefore, it is concluded that there is a strong nonlinear relationship between overtopping wave velocities, time, and wave front positions and that this relationship is prominent when the flow velocities are developed predominantly in a wave crossing direction.

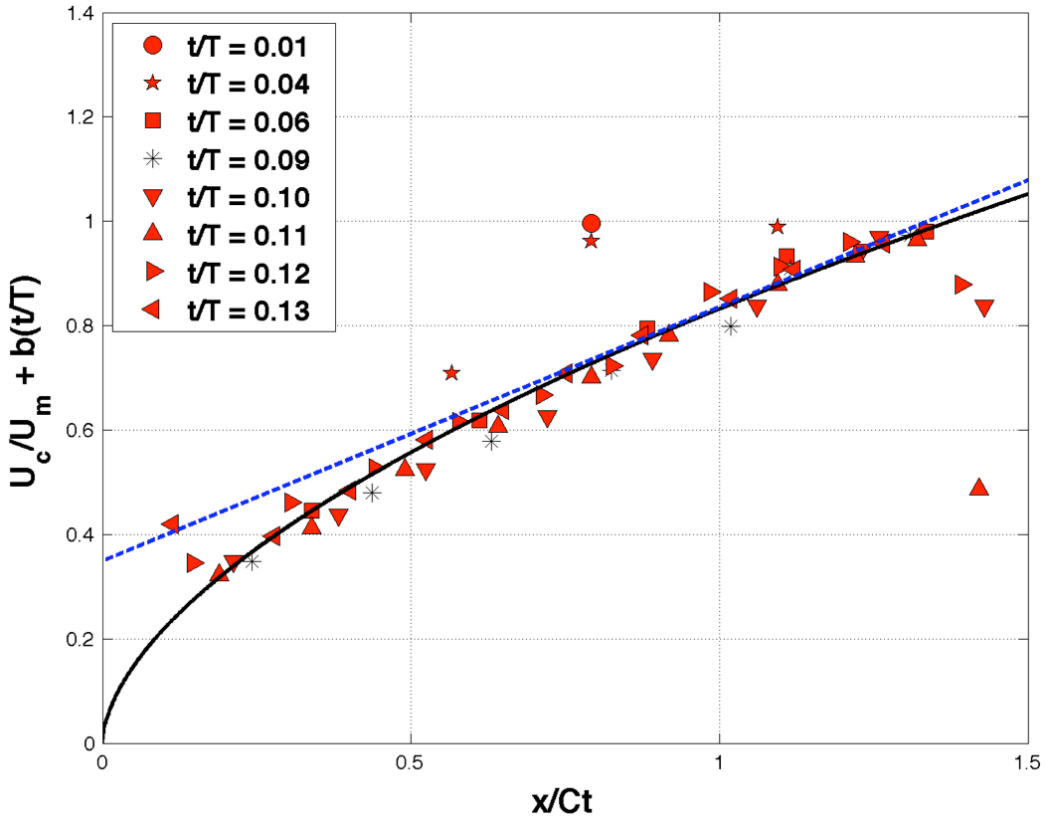

Figure III-8 Similarity profile. Nondimensional velocity, time, and distance values were obtained from the data presented in Figure III-6. Marker shape varies depending on t/T values. Solid line is the fitting curve based on least square regression and the dashed line is a linear fit by least square regression.

III.3.4 Discussions: effects of large scale experimental conditions on flow kinematics

As discussed earlier, significant increases in vertical motions of exit flows near the rear edge of the deck must be attributed to the velocity drops in the wave front. Ryu (2006) has also noted the velocity drop phenomena from his green water velocity measurements on both long and short decks (i.e., L = 25 *cm* versus L = *37 cm*). In their study, the velocity drops took place earlier (i.e., after a shorter downstream propagation) over the short deck, while the velocity structures further ahead of the rear edge have shown to be similar between both flow regimes. Ryu further noted that the flow tended to develop more dominant horizontal motions over a longer deck surface, resulting in slightly higher cross sectional flow speed U at the end. Thus, it was

suggested that investigation on the velocity structure of rapidly varying green water flow needed to be conducted with a structure providing a sufficient longitudinal extent for fully developed flow field. In this study, the characteristic phase speed of the simulated wave is 1.3 times higher than that employed by Ryu (2006). Based on the Froude scaling law, the deck length equivalent to the longer deck employed by Ryu is approximately 60 cm in the present large-scale experiment. The length of the deck surface used in this study is 75 *cm*, based Ryu's (2006) conclusions. The deck structure used in this experimental setup should provide a sufficient longitudinal extent for the green water wave fieldto develop its characteristic structure.

The velocity drop phenomenon has been observed for about 25% of the total longitudinal extent of the deck *L*. This is much higher than what was reported (i.e., 5%, or 3 *cm*) from the long deck experiment in a two-dimensional setup by Ryu (2006). In fact, it is closer to the ratio resulting from their short deck test (reported as 25%, or7 *cm*). Furthermore, the maximum horizontal velocity observed in the present study is 1.6*C* (4.13 *m/s*), higher than the 1.2*C* (2.40 *m/s*) observed by Ryu (2006) from the flow over the long deck. On the other hand, Aryiarathne (2011) has conducted experimental investigations for measurements of green water flow velocities over a deck structure equivalent to Ryu's model scale but in a three-dimensional setup. Green water velocities generated by both deck- and wall-impinging waves were observed. They reports a maximum horizontal velocity of 1.2C in the case of wall impingement , and 1.4*C* in the case of deck impingement. The green water waves observed in the present study have a Froude number value of F_r = 2.66 ($U_{\max}/\sqrt{gH}$); higher, but comparable to F_r = 1.57 and F_r = 2.19 observed by Ryu (2006) and by Aryiarathne (2011), respectively. The Reynolds number evaluated with the *H* from WG4 and the maximum velocity U_M is $R_e = 6.4\times10^5$ (HU_M/υ), which is about one factor higher than $R_e = 3.8\times10^5$ and $R_e = 3.2\times10^5$ observed by Ryu (2006) and by Aryiarathne (2011), respectively. This means that the impinging waves in the present study produced more turbulent (R_e >>5000) and supercritical (F_r>1) green water flows than what was generated through the smaller scale wave simulations.

These results may lead to the conclusion that the three-dimensionality of wave breaking should not significantly affect the evolution of horizontal flow velocities, considering more prominent influences of wave impingement conditions. However, more investigations are needed since the velocity measurements from both studies have been made neither with a structure of identical geometrical characteristics (i.e., plain versus triangular frontal edge shapes) nor at equivalent measurement points. More importantly, in a real sea state, the wave conditions at

breaking are unlikely to be distinct or repeatable as during the aforementioned small scale experiments. Hence, the green water wave kinematics and its impact potential should be studied while taking into consideration the random and complex conditions of wave breaking. This present study has significance in that it has investigated the impact potential of extreme wave kinematics with consideration of randomness in wave breaking patterns. As discussed earlier, Figure III-3 demonstrates a variety in breaking patterns, and the large-scale setup of this study has rendered diverse breaking wave characteristics for simulated waves.

In order to make the information from the averaged velocities meaningful as representative of general breaking wave characteristics, the randomness inherent in individual velocity measurements has to be carefully sorted out. For example, the maximum velocities observed during the initial phase of the wave overtopping are attributed largely to the splashing jet flows created by waves impinging on the front face of the deck (type 2 shown in a right column in Figure III-3). On the other hand, when the wave impinges directly on the surface of the deck while breaking, the flow velocities rather gradually increase and the flow structure shows a less turbulent field (type 2 shown in a right column in Figure III-3). Figure III-9a shows the temporal changes in maximum mean velocities in both x and y directions when averaged under different restrictions on the minimum number of realization limits N (*eqn.* (1). The individual time series is obtained from averaging the 5 highest maximum velocities calculated under respective restriction N in time. This means that the maximum mean velocities $U_{N,max}$ with N = 9 (50% of total repetitions), for example, are based on an average of the total number of instantaneous velocities accounted for (n> = N) only if more than 50% of the realizations contain the velocity information. Hence, the time series of $U_{N,max}$ with regard to the variation in N can be an indication of sensitivity of the mean velocity calculations to the number of realizations taken into account.

There are significant variations in the maximum velocities in both x and y directions when t<0.1T (t<0.18 s) with respect to N. These are the moments when the wave front has not yet reached the rear edge of the deck, implying that the flow fields generated in the initial phases of wave overtopping present significant complexity affected by the randomness of the splashing jet type wave flow . Averaging more repetitions shows maximum velocities diminishing in both magnitude as well as temporal variation. This is anticipated since the mean velocities tend to reduce irregularity in the distribution of maximum velocity locations between repeated measurements. However, the calculated mean velocities may readily ignore or undermine the

kinematic impacts due to fast jet waves. Such jet waves impose impulsive impacts on structural protrusions on an orthogonal plane over a deck surface, if any, within a short period after the wave impinging starts. Therefore, the irregularity in the velocity distributions in early phases should be preserved in the calculated mean flow information; otherwise, calculations may fail to capture the impulsive impact of the breaking wave front and cause the loss of velocity information rapidly evolving in phase with the wave front locations. The loss of velocity information is demonstrated by the velocity timeseries of $U_{18,max}$ in Figure III-9a (plotted with diamond markers).

The temporal variation of $U_{18,max}$ shows a rather peculiar pattern: slow propagations in the beginning (U<C), sudden discontinuation (or apparent detention of flow propitiations), and an abrupt increase (a velocity jump) between t = 0.11T and t = 0.13T. However, as it is a phenomenon unlikely to exist in a real flow within such a short period (~0.04 seconds), it is reasonable to consider lower values for the average threshold N. On the other hand, when the average was made using N less than 9, meaning a phenomenon reflected in less than 50% of the data set, the calculated mean velocities tend to overestimate the maximum flow speed and increase turbulence in the mean velocity fields. Hence, the values of N = 12~15 must be appropriate ranges for the available sets of data.

The value N = 12 was selected as a threshold limit based on observation of: the mean velocity maps (e.g., Figure III-4) that show continuation in the propagation of overall velocity fields in time; and the maximum velocity time series (Figure III-7) that shows a consistency in velocity values of neighboring data points. Furthermore, the maximum velocities of $U_{12,max}$ evaluated a higher speed $U_{12,max}$ = 1.5C than that of $U_{15,max}$. Therefore, the estimations with N = 12 can be considered more conservative upper limits. Hence, they may be more applicable as reference velocities estimating the impact potential of overtopping wave kinematics in safety design and engineering defense systems.

It is also interesting to note that the averaged velocities calculated with any chosen values for N converged together after t = 0.13T, coinciding with the wave front reaching the rear of the deck. Here, the maximum velocities stay around U_{max} = 1.3C for about 0.08 seconds, then consistently decrease toward 0.5C. This implies that the irregularity evident in the flow just after breaking becomes diminished. At that stage, the flow field may be dominated by rather uniform x directional inundation overflows. Accordingly, the y direction flow velocities become fairly close to zero. Therefore, it is presumed that the waves overriding the deck surface without

forming a splashing jet front may impose a wave impact load which is less impulsive but lasts for a relatively longer period on a vertical plane over the rear portion of the deck surface. The time interval between the occurrence of this type of impact load and that of the impulsive pressure (discussed earlier) is approximately $0.05T$ ($\approx 0.08\ s$) in present measurements. Aryiarathne et al. (2012) reports similar patterns in the x direction velocities measured during deck impingement during small-scale experiments (see Aryiarathne et al., 2012), velocity time series U_{max})of . However, the time interval between the first impulsive peak and a subsequent, longer-lasting peak was barely $0.01T$ in the velocity measurements from a vertical FOV plane (i.e., based on the BIV images capturing the xz-planes). The distinction between the two types of peaks was unclear in the velocity measurements obtained during the wall impingement. Instead, the intensified velocity humps were observed for significantly longer periods. It is interesting to note that in this case the maximum velocity profile resembles that of $U_{15,max}$. In Figure III-9a, the velocity profile of $U_{15,max}$ tends to average down the initial peak velocities attributed to the splashing jet and form gradually varying velocity humps. Therefore, it is presumed that when the time interval between two types of maximum velocity occurrences is short enough, the maximum velocities due to the splashing jet flow and those due to the later overtopping wave flow must be indistinctive. Hence, during the averaging process, two originally separated peaks could be treated as a single event and result in missing resolution in both magnitude and timing of the maximum velocities. Such a lack of resolution in time and space must be understood as an example of the "scale effects" often observed in the measurements from small scale experiments. Accordingly, it is important to choose appropriate geometric scales for the experiment design so as not to lose critical features of the simulated waves and their interaction with the setup. Therefore, this study may be found informative by providing the wave kinematic information obtained through large laboratory tests. The comparison to the results from an equivalent small scale experiments will give more concrete ideas on how the "scale effects" influence measurements for wave kinematic characteristics and subsequent approaches to data processing.

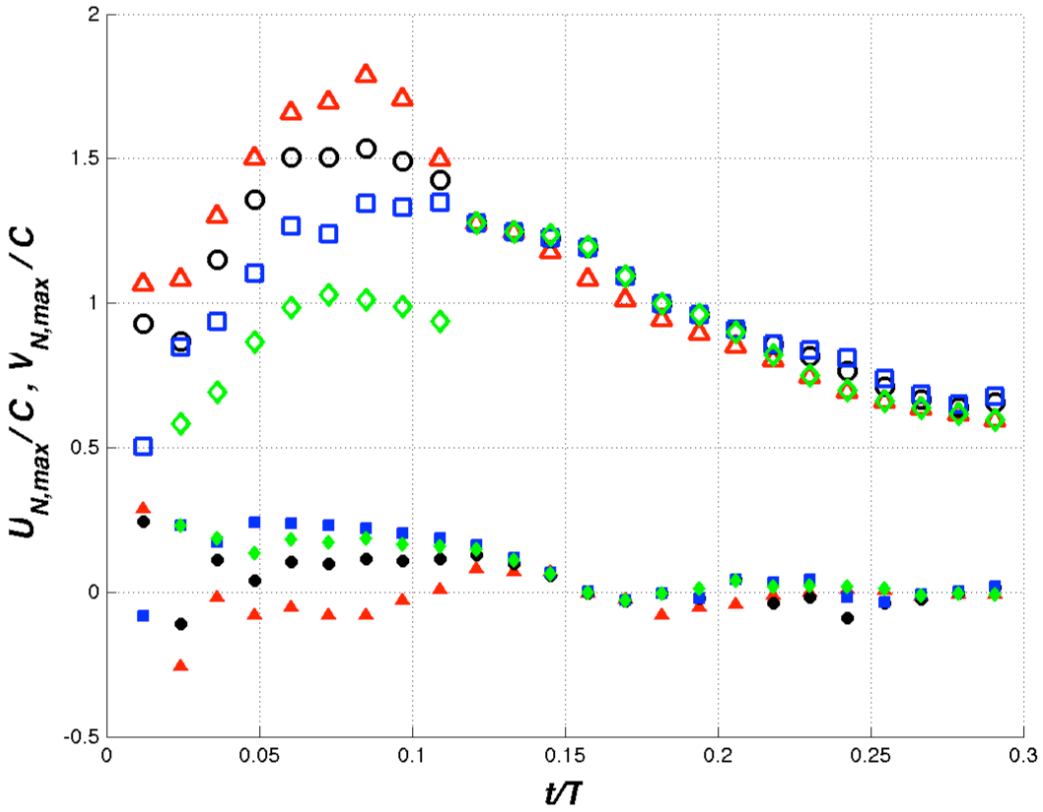

Figure III-9 Mean velocities and turbulence intensities varying with the number of realizations accounted for averaging. Maximum mean velocities $U_{N,max}$ (hollow) and $V_{N,max}$ (solid) are evaluated according to Eqn. (20) with varying threshold limit N,. △: N = 9, ◯: N = 12, □: N = 15, and ◊: N = 18.

III.4 Green water impact pressure

III.4.1 Spatial variations of wave dynamic pressures and maximum wave impacts

Figure III-10 shows spatial and temporal variations of mean pressures on vertical planes measured at various x, y, and z locations above the deck surface. The mean pressures were calculated by averaging a minimum of six repeated instantaneous pressure time histories at each location. The pressures and times are normalized by $\rho C^2 (= 6.66\ kPa)$ and T (=1.65 s), respectively. The respective vertical planes on which the wave impact pressures from an orthogonal direction(+x) were measured are at locations PMz (left column), PCz (middle column), and PSz (right column) as shown in Figure III-1 and listed in Table III-1. The vertical

locations of the measurement points were varied with 3 *cm* interval from 2 cm above the surface of the deck (Figure III-10a), 5 *cm* (Figure III-10b), 8 *cm* (Figure III-10c), and up to 11 *cm* (Figure III-10d). Substantial variations in the arrival time between individual waves (as discussed earlier) mean that averaging without considering such timing differences would have resulted in significant underestimations of the maximum mean pressures. Therefore, before averaging, individual pressure records were first synchronized by defining the time instance when an impulsive peak was recorded as t = 0. After the synchronization, the average standard deviations of instantaneous pressures from the mean pressure values at corresponding moments were about 0.16 *kPa*, or equivalent to 2% of ρC^2.

Overall, the measured pressure time histories have shown a single, prominent peak immediately followed by a gradually decreasing pressure gradient. This is a typical "church roof" profile (Peregrine, 2003) demonstrated during the impingement of jet waves on a rigid surface. The magnitude of the peak pressures appears to be affected mainly by variances in the locations along a vertical plane. Higher maximum pressures are observed at alternative vertical locations at *z* = 2 *cm* and z = 8 *cm*, while significantly decreased peaks are observed at z = 5 *cm* and z = 11 *cm*. Wave front shapes and the amount of entrapped air must have caused the oscillatory changes in peak pressures between the measurement points during the impingement. The wider, horizontal extent of the pressure gradients were observed at z = 2 *cm* with a maximum pressure of 1.5 ρC^2(equivalent to 9.95 *kPA*) in Figure III-10a(i). Hence, it is implied that the wave impacts near the surface of the deck last longer relative to the other locations. Furthermore, the region must be affected by impacts caused by both impulsive jets and intensified gravity waves of the overtopping flow. Note that the location of the maximum impact point is in the middle of the x extent of the deck near the centerline. The wave front velocities reached their maximum between x = 0.5*L* and x = 0.7*L* and higher velocities were observed in the middle of the y extent of the deck as shown in Figure II-4 and Figure III-6. On the other hand, Figure III-5 has shown that the distribution of the flow velocities become fairly uniform once the frontal flow velocities start decreasing from the center (y = 0) after passing of x = 0.7*L*, except for the front-most flow which has velocities slightly higher along the semi-centerlines in x direction. This explains the similarity in the shapes of pressure distributions between PCz and PSz, both located on the end of the rear edge of the deck, respectively at y = 0 and y = 0.25*L*. Furthermore, based on the original pressure time histories before shifting for synchronization

(not presented here), the impulsive pressure responses at z = 2 cm of PS2 in Figure III-10a(iii) overall took place shortly before any measurement point over z of PCz. The pressure records at PMz appear to take place over longer periods (wider shape in the pressure distributions) compared to that at corresponding locations of PSz. Therefore, it is presumed that the fast water front must first hit on a vertical plane slightly to the side of the centerline near y = *L*/4 (Figure III-10a(iii)), then followed by gradually imposing wave impacts from the main volume of wave overflow with increased depth Figure III-10c(ii).

As the measurement point moves higher, the shape of pressure distributions becomes slimmer, demonstrating dominantly impulsive characteristics. Hence, it is presumed that the tip of the impinging wave front must be projected toward z = 8 cm over the deck surface with a dynamic pressure of about $1.0\rho C^2$. Consequently, the greatly decreased pressures (about a factor of 2, compared to the maximum pressures at z = 2 *cm* on each vertical plane) near z = 5 cm must be mainly due to air trapped between the overturning wave crest and rising trough that impacts this intermediate vertical range (around z = 5 cm). Such great variability within a confined vertical extent also indicates a need for higher resolution for pressure measurement points within the vertical ranges below the wave surface and above the deck. Much lower average pressures—below $0.8\rho C^2$ at PM11 and below $0.4\rho C^2$ at both PS11 and PC11—occur intermittently at the highest measurement locations at z = 11 *cm*. This implies that the deck surface water depth is unlikely to exceed 11 *cm*, within the DOF of the BIV images, while droplets caused by impacting jet waves may have splashed randomly up to this level. Note that substantial turbulence in distributions of the mean pressures must have been caused by high frequency oscillation of entrapped air. The most severe fluctuations are observed at z = 2 cm at a mid-point *x* = *L*/2 in Figure III-10a(i) and at z = 8 cm near the rear of the deck at x = *L* as shown in Figure III-10c(ii). The duration of the oscillatory motion due to the entrapped air disappears shortly after the impulsive impact on the vertical plane at x = *L* and y = *L*/4. Therefore, it is presumed that the wave impacting this horizontal extent is mainly a jet flow that imposes rather impulsive impacts.

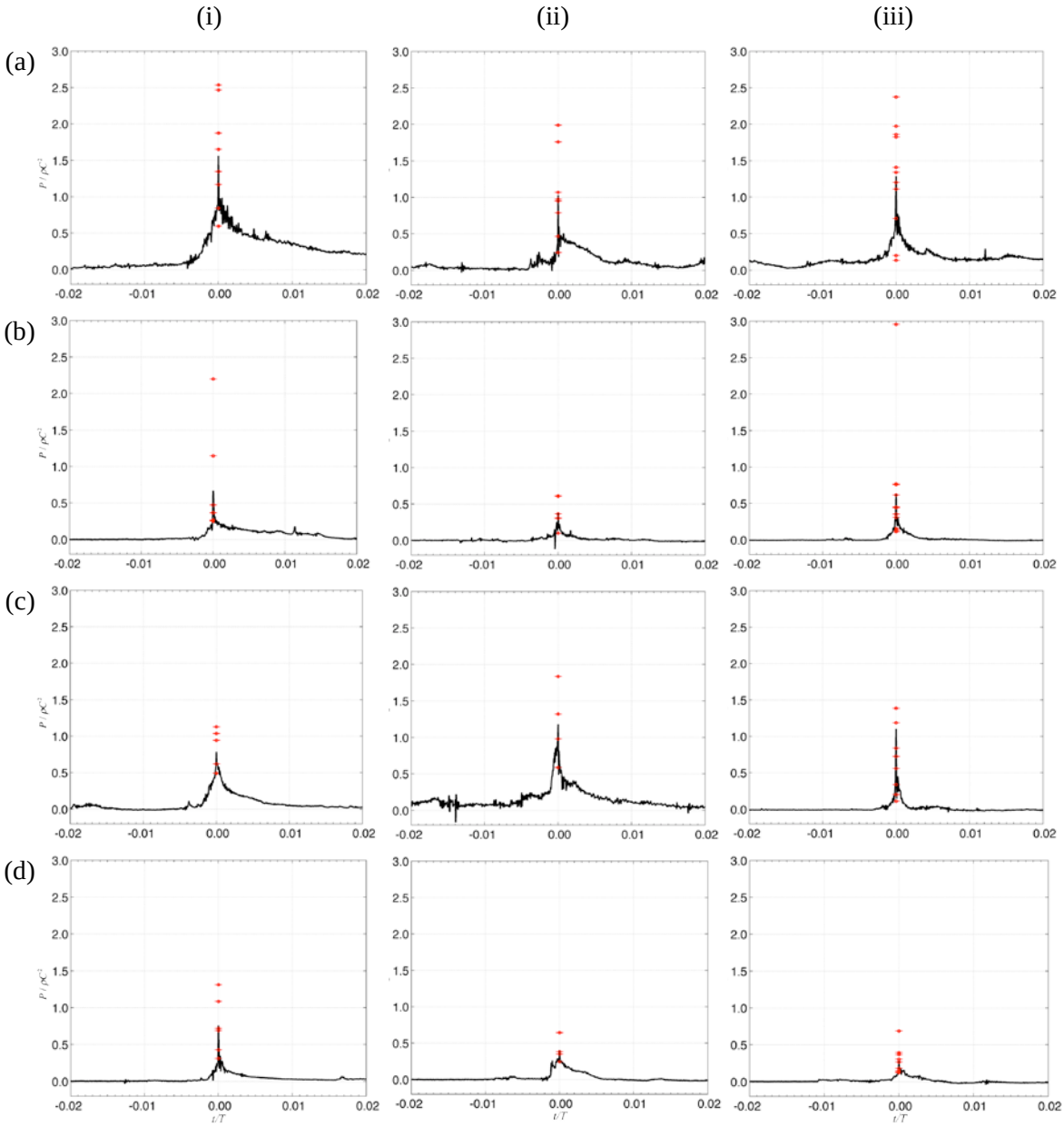

Figure III-10 Mean pressures on vertical planes in time at varying locations above a deck surface. Mean pressures are normalized by ρC^2 and time is normalized by *T*. Vertical planes where the pressure measurements were made are respectively located at (i) x = *L*/2, y = 0.05*L* (PM), (ii) x = *L*, y = 0 (PC), and (iii) x = *L*, y = 0.25*L* (PS). The measurement points on respective vertical planes are varied with 3 cm interval in z (from top to bottom), hence (a) z = 2 cm, (b) z = 5 cm, (c) z = 8 cm, and (d) z = 11 cm. Figure III-1 shows points of measurements and is summarized in Table III-1. Horizontal bars in individual plots mark the maximum pressures recorded by the instantaneous measurements.

Table III-2 summarizes the magnitude of the maximum mean pressure P_{max}, rise time t_r, and pressure gradients dP/dt shown in Figure III-10. The highest pressure observed was $1.56\rho C^2$ (equivalent to 10.38 *kPa*) from PM2 (at z = 2 *cm* above the surface) located at x= *L*/2 behind the leading front of the deck and y = 0.05 m alongside the centerline. In the rear edge of the deck at x = *L*, a vertical variability in the peak pressures was significant in measured pressures from both PCz and PSz. The observed maximum pressures near the end of the deck was slightly lower as $1.18\rho C^2$ at y = 0 (PCz) and as $1.28\rho C^2$ at y = *L*/4. However, the pressure gradient dP/dt increases significantly above 3000 *kPa*/*s* at the vertical points where higher maximum pressures were measured on both vertical planes located at y = 0 and y = *L*/4. This is approximately a two-fold increase in impulsiveness compared to that of dP/dt = 1513.40 *kPa*/*s* from PM2 at the center of the deck.

Table III-2 Measured maximum mean pressures and impulse time

Locations	z (*cm*)	P_{max} (*kPa*)	c_i' ($P_{max}/\rho C^2$)	t_r (*s*)	dP (*kPa*)	dP/dt (*kPa/s*)	$(dP/dt)/(\rho C^2/T)$
PM2	2	10.38	1.56	0.0065	9.84	1513.40	375.14
PM5	5	4.43	0.67	0.0036	4.43	1231.22	305.20
PM8	8	5.23	0.79	0.0036	5.03	1398.47	346.66
PM11	11	5.04	0.76	0.0024	4.92	2051.88	508.62
PC2	2	6.86	1.03	0.0016	6.19	3871.13	959.58
PC5	5	2.55	0.38	0.0056	2.54	453.04	112.30
PC8	8	7.87	1.18	0.0020	6.19	3096.85	767.65
PC11	11	2.70	0.41	0.0027	2.64	976.04	241.94
PS2	2	8.55	1.28	0.0030	7.46	2487.90	616.70
PS5	5	4.16	0.62	0.0023	4.06	1766.48	437.88
PS8	8	7.35	1.10	0.0022	7.23	3284.73	814.22
PS11	11	1.93	0.29	0.0017	1.83	1076.53	266.85

III.4.2 Discussion: scaling effects on pressure impulsiveness and extreme impact probabilities

Both magnitudes and temporal gradients of peak pressures are highly variable between repeated measurements as indicated by the circled tick marks on individual plots. This was anticipated based on the BIV image records demonstrating random evolutions of wave front shapes during overtopping moments. Therefore, the impact potential of the dynamic pressures of overtopping waves can be more effectively evaluated when the maximum pressures are measured with the rate of occurrence or frequency. Hence, the individual pressure measurements were further investigated. Figure III-11 shows distributions of the maximum pressures from repeated measurements. In Figure III-11a, the occurrence rates are plotted against the relative peak pressures by denoting different locations of the vertical measurement planes on a horizontal plane on the deck surface while disregarding variances in z locations. Figure III-11b - d further demonstrates the variation due to changes in z-position within the range of measurement points on individual vertical planes of PMz, PCz, and PSz. In each plot, the instantaneous peak pressures p_{max} were compared to the maximum mean pressure P_{max} shown in Figure III-10. The occurrence rates were evaluated by calculating the ratio between the number of instantaneous peak pressures corresponding to the specified ranges of $p_{max} < -P_{max}$, $-P_{max} \le p_{max} < P_{max}$, $P_{max} \le p_{max} < 3P_{max}$, and $3P_{max} \le p_{max}$, and the total number of repeated measurements either on a vertical plane (Figure III-11a) or at respective measurement points (Figure III-11b-d). The percentage of occurrences of maximum pressure values belonging to the respective ranges were plotted against the center values of each bin. The distributions show that 60% of the peak pressures have occurred within $\pm P_{max}$, indicating that the maximum pressures evaluated based on the mean pressure time histories successfully represent the pressure impact potentials independently from the measurement locations. However, the peak pressures at the high impact regions at z = 2 *cm* on PMz and z = 8 *cm* on PCz often exceed the higher magnitude range of $P_{max} \le p_{max} < 3P_{max}$ in about 50% of measurements. Therefore, the maximum pressures of $p_{max} \approx P_{max}$ can be considered as a reference pressure that practically evaluates the dynamic impacts of overtopping waves with these characteristics, while the increased value, $2P_{max}$, which is the second-most frequently measured pressure value, can be serve as a conservative threshold.

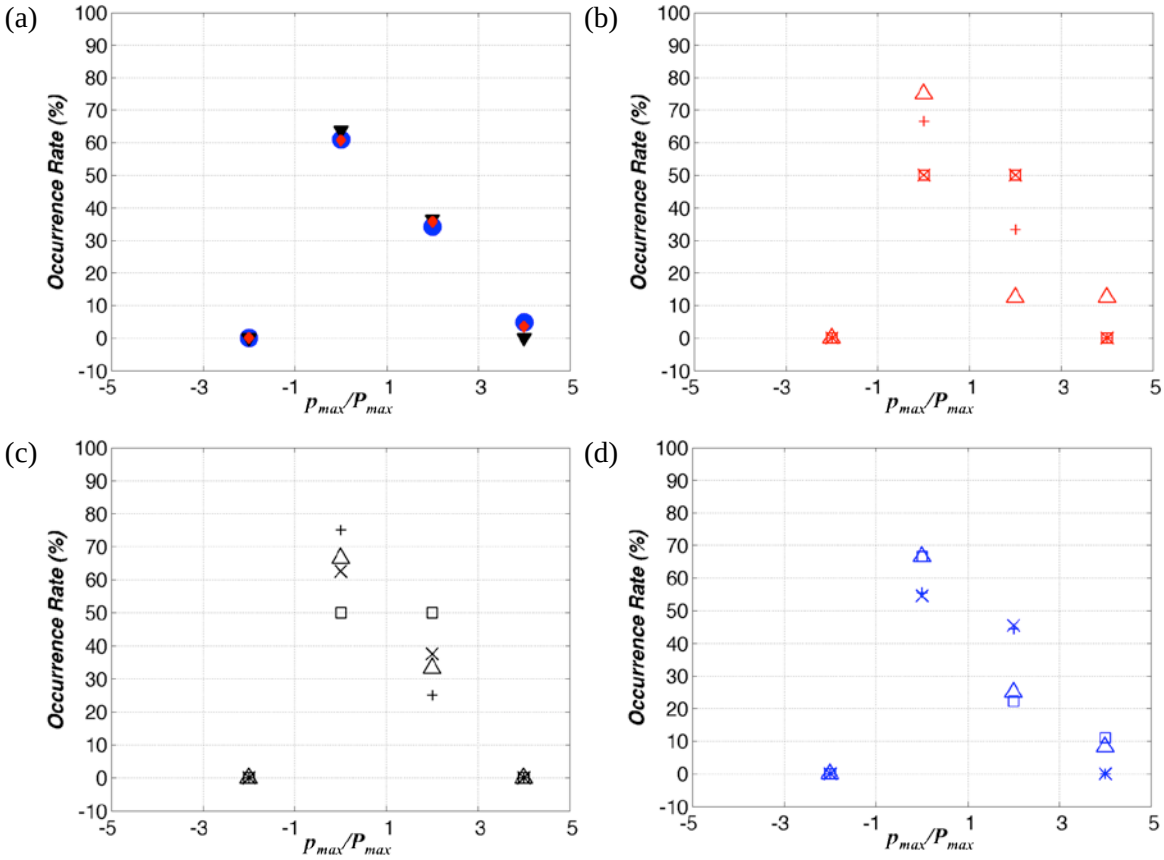

Figure III-11 Distributions of the maximum pressures relative to the maximum mean pressures and rates of occurrence from measured pressures. Maximum pressures from repeated measurements were compared to P_{max} and counted for the number of occurrence within the following ranges: $p_{max} < -P_{max}$, $-P_{max} \le p_{max} < P_{max}$, $P_{max} \le p_{max} < 3P_{max}$, and $3P_{max} \le p_{max}$. Occurrence rates of the pressures belonging to those ranges were plotted against the center values of each bin. (a) Distributions of the maximum pressure occurrences at varying x-y locations: ●, from PMz; ▼, from PCz; and ◆, from PSz. Distributions varying with z locations on each vertical plane at: (b) PMz; (c) PCz; (d) PSz. In (b-c): ×, z = 2 *cm*; △, z = 5 *cm*; □, z = 8 *cm*; +, z = 11 *cm*.

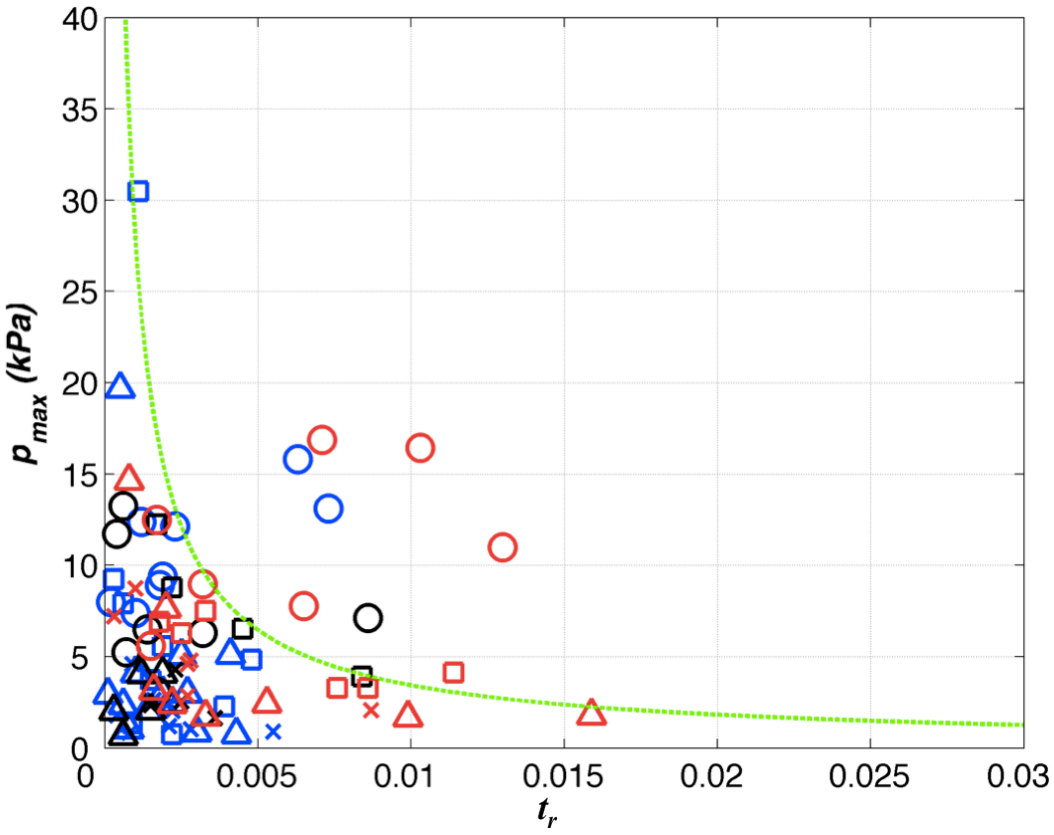

Figure III-12 Maximum impact pressures p_{max} against rise time t_r. Maximum measured pressures: red, at PMz; black, at PCz; blue, at PSz. Different marks denote variation in z at the measurement point of: ○, z = 2 *cm*; △, z = 5 *cm*; □, z = 8 *cm*; ×, z = 11 *cm*; --, an envelope $52t_r^{-0.91}$.

The dynamic impacts from wave impingements are often investigated with regard to the impulsiveness of the imposed pressures by relating the maximum pressures with the rise time toward the peak pressure as:

$$p_{\max} = at_r^b \tag{22}$$

where, a and b are empirical coefficients determining the fitting curve that describes exponential decays of p_{max} with increasing rise time t_r. Numerous researchers have reported a wide variety of values for a and b (e.g., Weggel and Maxwell, 1970; Blackmore and Hewson, 1984; Kirkgöz, 1990; Hattori et al., 1994; Cuomo et al., 2010) and a good summary table is provided in Ariyarathne et al. (2012). The studies have generally demonstrated the tendency of high impact

pressure peaks to be closely associated with a short rise time. However, the Eqn. (3) attempts to derive the correlation between rise time and consequent peak pressures in a dimensional space but no dimensionless similarities are known. On the other hand, when the wave flow contains enough air bubbles to become a water-air mixture, the air bubbles trapped between the water-structure interfaces cause significant oscillation and discontinuity in a measured pressure time series. This, in turn, increases uncertainties in determining a starting moment of the pressure rise that directly leads to the impulsive peak pressures. Consequently, the relationship between the rise time and subsequent peak pressures can vary considerably depending on the measurement conditions such as a measurement scale, and degree of aeration as well as the characteristics of the simulated wave flows.

Figure III-12 shows the maximum pressures from instantaneous measurements against the rise time. In that present scale, 80% of the measured peak pressures observed have a rise time shorter than 5 *ms*, indicating strong impulsiveness. On the other hand, the longer rise times (t_r>5 *ms)* are mostly at a height of z = 2 cm and comprised of both impulsive peak and relatively slow pressure gradients that resulted in a longer duration of pressure imposition, as demonstrated in Figure III-10a. Therefore, in the present scale, impact pressures due to the overtopping waves are predominantly caused by the impulsive peak from an impinging jet while the strong inundation flow may have extended the impact duration, hence causing higher impact loads near the surface of the deck. The line $P_{\max} = 52 t_r^{-0.91}$ in Figure III-12 separates the different features of impulsive pressures above which impact pressures are anticipated to last for longer.

Ariyarathne et al. (2012) investigated the dynamic pressures of three-dimensional green water waves above a deck structure in a smaller-scale setup (i.e., with a geometrical ratio to this study of λ = 1.56, based on the Froude similarity). They measured the maximum impact pressures at z = 0.02 m as 4364 Pa and 5048 Pa respectively at 0.05 m away from the centerline during the wave impingement on the deck surface. Those are equivalent to 6.81 kPa ($\approx 1.07 \rho C^2$) and 7.87 kPa ($\approx 1.24 \rho C^2$) in the present scale and are the same orders of magnitude with the maximum pressures observed in the proximity of the corresponding point z = 0.02 m in the present study. However, the pressure gradients of those categorized as an impulsive type pressure were far below the maximum dP/dt = 1393 kPa/s ($\approx 345.3 \rho C^2/T$) at z = 0.02 m at the centerline. In this study, measured values for dP/dt are higher than 1500 kPa/s ($\approx 371.8 \rho C^2/T$) at any location where the maximum pressures were observed (e.g., at z =

0.02 m from PMz and PSz or z = 0.08 m from PCz). The highest gradients associated with the maximum pressures at each vertical plane were 1513 kPa/s ($375.1\rho C^2/T$) at PM2, 3097 kPa/s ($767.7\rho C^2/T$) at PC8, and 2488 kPa/s ($616.7\rho C^2/T$) at PS2 as shown in Table III-2. Therefore, observation implies that the effect of differences in measurement scales is more substantial to variances of the pressure rise time or duration of the impacts compared to that of the peak pressure magnitudes.

III.5 Correlations between wave impacting pressures and green water kinematics.

The foregoing analyses for the BIV images, green water velocity structures, and pressure time histories have demonstrated impulsive characteristics of green water wave impacts. Furthermore, the time series of the maximum velocity components in x and y directions shown in Figure III-9 indicates that it is the x direction component of the wave flow above a deck surface that predominantly contributes to the dynamic impact on a vertical plane orthogonal to the incoming waves. Therefore, the maximum peak pressures measured during the wave impingement are compared to the impact pressures produced by the kinematic energy due to the maximum velocities of the x directional flow, expressed as:

$$P = \rho U_{\max}^2 \tag{23}$$

As discussed earlier, the maximum flow velocities were observed in the wave front along the centerline during x<0.75*L* Thereafter, the velocities become slightly faster along the semi-centerline. Accounting for such local variability in flow speeds, the wave impact pressures were calculated based on the local mean flow velocities near the locations of vertical pressure measurement planes (i.e., PMz, PCz, and PSz) on xy-planes over the deck surface.

Note that, while the full-field information is available at all velocity output nodes on x-y grids over the deck surface (i.e. 64 by 64 vectors for x and y direction velocities, respectively, on the xy plane within the FOV), only a single velocity vector was obtained from an arbitrary vertical point within the DOF since the BIV measurements were made only on a horizontal plane. Therefore, the maximum pressures from the averaged local pressures from individual sensors at different vertical locations (i.e., z = 2, 5, 8, and 11 cm) were compared to the maximum velocities observed from velocity output nodes within a local window on a horizontal plane over the deck surface. The local windows were selected to contain and surround individual

pressure measurement planes (i.e., PMz, PCz, and PSz) orthogonal to the x-component velocities of incoming wave flows. Figure III-13a shows time series of the maximum local velocities extracted from respective local windows near the pressure sensor locations at PMz, PCz, and PSz. Note that no velocity line means the wave flow containing air bubbles has not reached each pressure sensor location (e.g., the area of local windows). Hence, it is assumed that the maximum kinematic impacts on the vertical planes of both PMz and PCz are caused by the wave frontal flow that impacts the respective planes with U_{max} of 1.3C (3.43 *m/s*) at t = 0.08T (0.14 *s*) and 1.2C (3.11 *m/s*) at t = 0.12T (0.20 *s*). On the other hand, the velocity time series at PSz has shown a slight increase before decreasing at its maxima of 1.1C (3.00 *m/s*) at t = 0.15T (0.22 *s*). Hence, it may be the flow behind the wave front that imposes most significant impacts on the rear end point alongside the center of the deck.

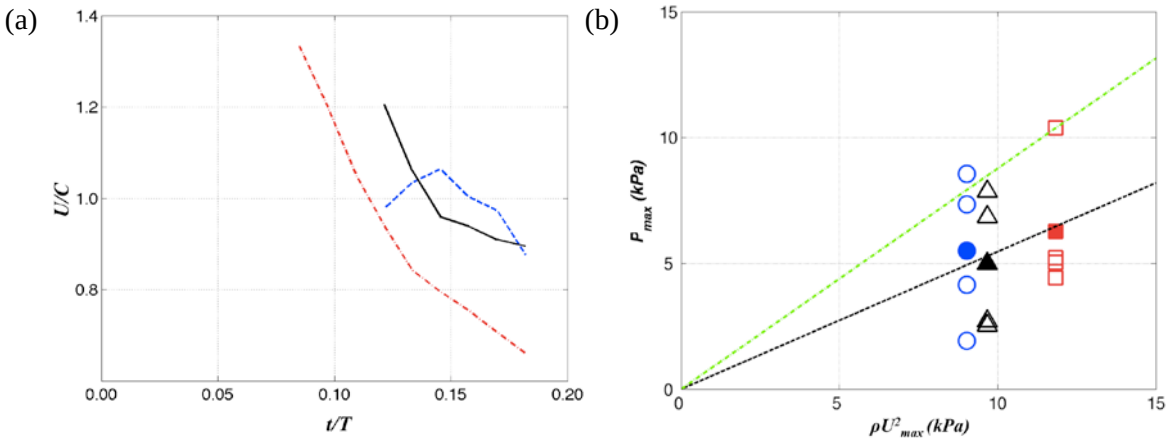

Figure III-13 Maximum local velocities and maximum local pressures. (a) Maximum mean velocities within 23.4 × 23.4 mm^2 local windows on xy-plane containing the pressure measurement points at: -. (dashed-dot), PMz; − (solid), PCz; and - - (dashed), PSz. (b) P_{max} versus ρU^2_{max}: □, PMz; △, PCz; ○, PSz; a dashed line (black) is a least squared fit with mean pressures at respective vertical measurement locations with a slope of 0.55, R^2 is 0.93 and RMSE is 0.65 *kPa;* a dotted line (green) is a least squared fit with absolute maximum pressures at respective vertical measurement locations with a slope of 0.88, R^2 is 0.77 and RMSE is 0.51 *kPa.*

In order to examine correlations between wave kinematic energy and dynamic pressures imposed by impacting waves, the kinematic impact pressures calculated from Eqn. (4) need to

be compared to the maximum pressures. Figure III-13b shows the impact coefficient c_i defined as a ratio of the maximum pressures P_{max}(z) observed from measurement positions z = 2, 5, 8, and 11 *cm* (hollow marks) to $\rho U_{\max}^2$ at corresponding x and y locations over the horizontal plane on the deck. Thus, there are four maximum pressure values from varying z positions on each vertical measurement plane (e.g., the maximum of PM2, PM5, PM8, and PM11, respectively). However, without knowing the vertical profiles of $U(x,y)$, only one maximum velocity value at a location of each pressure measurement plane is currently available (i.e., U_{max} at the locations of PMz). Therefore, the maximum pressure values obtained from each z location are compared to a constant U_{max} for each (x,y) location of the respective vertical measurement planes (hollow marks in Figure III-13b). Figure III-13b shows ratios between the measured maximum pressures and maximum flow velocities orthogonal to each other. The slope of a linear fitting line (dashed, in a dark color) in Figure III-13b representing the mean impact coefficient is 0.55: about 55% of kinematic energy from the overtopping wave is convertible to the impact pressures. On the other hand, for practical applications of extreme value statistics means knowing the average ranges of ratios between maximum P_{max}(z) and $\rho U_{\max}^2$. Therefore, for extreme impact statistics, the upper limit impact coefficients are evaluated with the absolute maximum pressures, those that are the greatest of four pressure values from each pressure measurement plane. The linear fitting line (dotted, in a light color) in Figure III-13b shows the maximum average impact coefficient is 0.88: in extreme cases, about 88% of the kinematic energy from the overtopping wave is converted to impact pressure. Note that distributions of c_i in Figure III-13b demonstrates a clear linear correlations between the measured maximum kinematic energy and either absolute maximum dynamic pressures or averaged maximum pressures on the orthogonal impact surfaces. Admittedly, more pressure information, with higher spatial resolution in measurement points over the deck surface, is required in order to confirm these observations. Nonetheless, the present measurement locations are considered optimal because they were specified for the areas where the most significant wave impact events are expected to take place based on the BIV analysis.

Eqn. (4) can be restated to define c_i' regarding the characteristic wave phase speed C that is often readily available as:

$$P_{\max} = c_i \rho U_{\max}^2 = c_i' \rho C^2 \tag{24}$$

Table III-2 lists the values for c_i' at various pressure measurement locations. The values of c_i' varies from a minimum of 0.29 at PS11 to the maximum of 1.56 at PM2. Note that those c_i' associated with the maximum pressure measurements at respective pressure measurement planes are commonly $c_i' >$ 1.18 where the lowest value is from PC8. Ariyarathne et al. (2012) has reported that c_i' from impulsive wave impacts varied from the lowest $c_i' = 0.59$ to the highest $c_i' =$ 7.24, while non-impulsive impacts from wall impingement waves remained fairly constant near $c_i' = 1.28$. As discussed earlier, the present maximum pressures over different vertical measurement planes have shown strong impulsiveness with $dP/dt >>$ 1393 kPa/s ($\approx 345.3\rho C^2/T$), according to the classifications of Ariyarathne et al. However, the corresponding values of c_i' are varied within relatively narrow ranges ($0.29 \leq c_i' \leq 1.56$) with a smaller maximum value that is rather close to the c_i' associated with non-impulsive impact pressures (Aryarathne et al, 2012). The smaller lower limit $c_i' = 0.29$ must be related to the over-simplification of a vertical profile of U_{max}: the impulsive overtopping flow could produce more variations in flow velocities over inundation depth that could be much slower near the deck surface than that near the free surface. Furthermore, such contradictory patterns in distributions of c_i' may be related to the effects of air entrapments, stated as:

$$P_{\max} = c_i'\rho C^2 = \rho(1-\alpha)\overline{c_i}C^2 \tag{25}$$

Here, $\overline{c_i}$ is the constant impact coefficient expected from fully saturated fluid disregarding air entrapment. α is the void fraction accounting for the volume fraction occupied by air entrapped within a unit volume of fluids. Thus $\alpha = 0$ for fully saturated water and $\alpha = 1$ in the air. Eqn. (25) implies that air entrapments within fluid could result in smaller values for c_i', indicating low rates of kinematic energy transfer to impacting wave forces. Hence, the present smaller values of c_i' observed during more impulsive wave impacts could be indications of a greater degree of air entrapment. Therefore, it is concluded that, in the present large scale experiments, the impact pressures on the structures are strongly affected by both variability of flow structures and impulsiveness of impacting waves containing considerable air volumes. Therefore, this finding suggests that potential dynamic impacts from wave kinematic energy need to be investigated with consideration to the effect of air entrapment. In this context, the wave impact patterns and correlations with green water kinematics will be investigated in further detail by taking the air entrapment effects into account based on measured void ratio in future studies.

III.6 Summary and future study

This study experimentally investigated evolutions of green water wave flows on a three dimensional deck structure in a large scale ocean wave basin. Using the BIV technique, overall flow structures and temporal and spatial distributions of the maximum velocities were successfully evaluated. Pressure measurements were also conducted at four different vertical positions on vertical measurement planes at three different locations on the horizontal plane. Velocity measurements were compared with pressure measurements and correlations between the kinematic energy and dynamic impacts on the structure were evaluated. The results were compared to the results from similar two-dimensional and three-dimensional green water wave studies. The comparisons were discussed with regard to the scaling effects of laboratory experiments. Some findings are summarized as follows:

(1) Two distinctive overflow patterns were observed from both instantaneous velocity fields and BIV images depending on the shapes of breaking wave fronts during impingements. When waves directly impinged on the deck surface, the overtopping wave developed an evident leading front and tended to propagate continuously. When waves first impinged on the side of a structure in advance of impingements on the deck surface, splashing jets from breaking waves were produced. In this case, waves propagated much more rapidly and with significant variability in shapes between repeated tests.

(2) Temporal and spatial distributions of mean green water velocities over a deck surface were evaluated. The mean velocity fields were obtained by taking phase averages of at least 12 instantaneous velocity values from 18 repeated measurements. Spurious errors that are rarely shown in overall instantaneous velocity fields were removed with a threshold limit N = 12.

(3) The most significant spatial variability in mean velocities in the propagating direction was found from the protruding wave front near the center of the deck during early stages of the wave run-up. The maximum front speed of 1.4C was first observed in the center of the deck near y = 0 at a midpoint of the deck (x = 0.5L). The flows along the semi-centerlines reached the maximum velocity of 1.4C at x = 0.7L. After this point, the wave front formed fairly uniform distributions along the y axis. The flow velocities started decreasing below 1C over all fields once the wave frontal flow passed the rear edge and started leaving the deck.

(4) Variations of the maximum mean velocity U_C were investigated along the wave crossing direction. The cross sectional velocity maximum was U_C = 1.58C (4.08 *m/s*) at x = 0.65L at the wave front. However, the rates of velocity increase decayed after the wave front reached local

maximum velocities near $x = 0.65L$. Velocity drops were not observed on the flows arriving on the deck after the overtopping wave fronts exited the deck surface area. In fact, they seemed to never reach maximum within the longitudinal extent of the deck structure.

(5) Temporal variations of the maximum cross sectional velocities U_M were also investigated. The maximum U_M occurred at t = 0.08T (0.14 *s* after the wave front reached the deck front) with $U_M = 1.58C$ at the front. However, the flow that reached the rear edge first ($U_M = 1.3C$) was not at the maximum velocity over the field. In fact, those with higher speeds arrived about 0.01T(0.02 *s*) later. Furthermore, a dimensionless prediction equation for U_C/U_M (Ryu, 2006) was developed and confirmed a strong nonlinear relationship between overtopping wave velocities and time and wave front positions when the flow velocities are developed predominantly in a wave crossing direction.

(6) Kinematic information obtained from this experiment was compared with that from equivalent but smaller scale experiments. The maximum horizontal velocity U_{max} was observed as high as 1.6C (4.13 *m/s*) in present study, while it was $U_{max} = 1.2C$ (2.40 *m/s*) in Ryu (2006) from the flow over the long deck. It is also compared to the three dimensional green water study of Aryiarathne (2011) that reported U_{max} = 1.2C in the wall impingement case and $U_{max} = 1.4C$ in the deck impingement case. Furthermore, the velocity drop phenomena that were commonly observed from the flow on the rear portion of the deck behind the wave front was discussed. It was observed at about 25% of the total longitudinal extent of the deck L in the present scale experiments, while it was much shorter period of 5% (i.e., 3 *cm*) from the long deck experiment in a smaller scale two-dimensional setup by Ryu (2006).

(7) Such significant differences in kinematic structures between green water waves of similar test installations were interoperated as laboratory scale effects. There are indications that small scale experimental setups are often unable to provide sufficient time and space for the overtopping green water wave to fully develop velocity structures. Also, strong randomness reproduced in this large scale wave experiment was characterized with regard to the velocity averaging technique. Discussion for the optimal choice of the average thresholds N for velocity phase averaging was provided as the over-averaging process was found to fail in reflecting essential kinematic features of extreme ocean waves. For present the scale, mean velocity fields accounting for minimum 67% instantaneous velocity fields at corresponding moments were found be adequate.

(8) The magnitudes of the maximum mean pressure P_{max}, rise time t_r, and pressure gradients dP/dt were evaluated based on pressure measurements. Most of measured pressures showed impulsive impact patterns with sudden rises of pressure peaks. The highest pressure was observed as $1.56\rho C^2$ at x = $L/2$.

(9) General distributions of the maximum impact pressures show that 60% of the peak pressures have occurred within $\pm P_{max}$, indicating that the maximum pressures evaluated based on the mean pressure time histories successfully represent the pressure impact potential independently from the measurement locations. In the present study, measured values for dP/dt are higher than 1500 kPa/s ($\approx 371.8\rho C^2/T$) at any locations where the maximum pressures were observed. The experiment scale effects resulted in substantial variances in the pressure rise time or duration of the impacts compared to that of the peak pressure magnitudes.

(10) Correlations between wave kinematic energy and dynamic pressure were examined to determine the impact coefficients. c_i' varied within relatively narrow ranges $0.29 \leq c_i' \leq 1.56$. In the present large scale experiments, the impact pressures on the structures are strongly affected by both variability of flow structures and impulsiveness of impacting waves containing considerable air volumes.

(11) This study suggests that potential dynamic impacts from wave kinematic energy need to be investigated with regard to the effects of air entrapment. Future studies should evaluate the impact coefficients by taking the void ratio measurements into account. This study observed wide variability in frontal shapes of overtopping green water waves. Therefore, BIV measurements need to be made on the vertical plane for evaluations of vertical velocity profiles beneath wave free surfaces. In addition, velocity fields on horizontal planes also need to be examined in detail at various vertical locations below free surfaces. Finally, this study employed a simplified static offshore deck model structure. Future studies should be conducted with more realistic dynamic ocean structures.

CHAPTER IV

EXPERIMENTAL STUDY ON FLOW KINEMATICS AND IMPACT PRESSURE IN LIQUID SLOSHING*

IV.1 Introduction

The huge and potentially devastating impact of liquid sloshing, a violent response from the free surface of gravity waves in a container subject to external excitation, has become a great concern to naval architect and marine engineers. For instance, many offshore oil storage units and various floating structures facilitating the development of natural resources in the deep ocean need to be built based on knowledge about sloshing dynamics for the structural integrity in a rough sea environment (Buchner, 1995; Buchner and Bunnik, 2007). In coastal engineering, impact of extreme surface waves such as hurricanes or tsunamis on structures prone to wave invasion is also a major factor in design consideration for the defensive construction (Bredmose et al., 2003; Hattori et al., 1994; Oumeraci, 1994; Peregrine, 2003). Moreover, an increasing utilization of moving vehicles or vessels as carriers of the liquefied natural gas (LNG) demands more accurate prediction on the dynamic behavior of the contained sloshing liquid in response to the external source of excitation such as oscillatory tank motion or sudden changes in speed and direction of a transporter (Delorme et al., 2009).

The motion of partially filled liquid in an oscillatory container may be characterized mainly by the geometry of the container, the liquid filling ratio, and the amplitude and frequency of the excitation motion (i.e., Abramson, 1966). It was commonly found that the most extreme resonant response occurs near the lowest mode natural frequency (Olsen, 1976). Some other parameters affecting the liquid sloshing motion can be the viscosity and compressibility of the filling liquid, ullage space, flexibility of the tank wall, and cushioning effects of the entrapped air (Bass et al., 1985). The resulting impact of the sloshing liquid on the container structure varies greatly both

*Reprinted with permission from "Experimental study on flow kinematics and impact pressure in liquid sloshing" by Song, Chang, Ryu, and Kwon (2013). *Experiments in Fluids*, DOI:10.1007/s00348-013-1592-5, Copyright [2013] Springer Publishing

in time and space due to the discontinuous, nonlinear transition of the free surface profile. Various numerical and experimental studies investigating effects of the dynamic impact have been performed. Common focuses in the studies are to investigate the localized distribution of hydrodynamic pressures inside the container, and to predict the motion of the unsteady and frequently violent liquid surface.

The existing numerical and analytical methods solving liquid sloshing problems have been developed mainly to resolve the rapid evolution of the free surface and the global distribution of the impact pressures produced by the sloshing waves. For liquid sloshing problems with a small free surface displacement and simple container geometry, theoretical solutions solving the governing Laplace equation are formulated based on the potential flow assumption with applications of the various analytical approximations (Abramson, 1966; Faltinsen, 1974) and numerical schemes (Faltinsen et al., 2000, 2005, and 2011; Thiagarajan et al., 2011) handling the boundary conditions on the free surface. For liquid sloshing in practical situations, especially for a low filling ratio with $h/L < 0.21$ where h is the still water depth and L is the length of the tank in the direction of motion (Ibrahim et al., 2001) or a significant viscous effect, the problem usually leads to nonlinear free surface deformation and violent fluid motion. Such liquid sloshing problem is usually numerically solved using Navier-Stokes equations based models. Most challenges lie in describing the nonlinear evolution of free surface and specifying the complex boundary conditions in the discrete computational domain (Hirt and Nichols, 1981; Ibrahim et al., 2001; Wang et al., 2011). Some liquid sloshing problems with large-amplitude sloshing waves were solved by implementing the finite element method with a Lagrangian description for the free surface (i.e. Okamoto and Kawahara, 1990 and 1997). Some researchers solved the governing shallow water equation by employing the Glimm's method to predict the large amplitude excitation of the free surface, especially when its discontinuity is expected due to the so-called hydraulic jump or wave impacts over the surrounding structure (i.e. Dillingham, 1981; Pantazopoulous, 1988; Zhou et al., 1999; Lee et al., 2002). Some implemented the finite different method or finite volume method within a fixed computational domain with an employment of various interface capturing methods such as the volume of fluid method (VOF; Hirts and Nichols, 1981) or level set method (LSM; Osher and Sethian, 1988).

The implementation of interface capturing methods for tracking the free surface enables a refined description of the violent sloshing flow where the viscosity or compressiblity effects play important roles (i.e., flow inside a tank of complex geometry and air-water mixing during

sloshing motion). For example, Celebi and Akyildiz (2002) and Akyildız and Ünal (2006) applied VOF methods to compute three-dimensional sloshing flows in a rectangular tank with baffles. Bredmose et al. (2009) solved the conservation equations employing the Riemann solver model in the finite-volume framework to compute the two-dimensional compressible, aerated flow. Chen (2011) employed the Reynolds Averaged Navier-Stokes (RANS) model with the level-set method to study both the compressible and incompressible flows in a two- and three-dimensional membrane-type LNG tank. More details and applications of various solution methods for solving the violent sloshing problems can be found in Mikelis et al. (1984), Amenio and Rocca (1996), Ibrahim et al., (2001), Rhee (2005), and Chen (2011). Alternatively, some researchers employed meshless methods to overcome the constraint in boundary value adoption for the computational grid. Among them, Rafiee et al. (2011) implemented the smoothed particle hydrodynamics method (SPH; Gingold and Monaghan, 1977) based on a Lagrangian approach by describing the flow with a large set of particles moving with the flow. Wu and Chang (2011) developed an improved radial basis function (RBF) method to overcome the strong nonlinearity of non-breaking sloshing waves inside a rectangular container undergoing two- and three-dimensional excitations.

Advances in computational resources in the past decades have contributed a great improvement in solving the liquid sloshing problems. Even so, numerical approaches often expose limitation in realistically simulating violent sloshing flows that are discontinuous, inhomogeneous, and three-dimensional due to the strong turbulence and multiphase nature of the flow.

The problem becomes either not amenable to the numerical models (such as air entrainment, bubble defragmentation and degasing) or not feasible to the enormous computation expanses. Furthermore, results computed using numerical simulations require data for validation, thus many laboratory as well as some prototype investigations have been conducted to improve our understanding of the liquid sloshing flow.

Experimental studies of liquid sloshing predominantly measure temporal and spatial distributions of dynamic pressures induced by the wave impact on container structures using pressure transducers (e.g., Akyildiz and Ünal, 2005; Bullock et al., 2007; Chan, 1994; Panigrahy et al., 2009). Laboratory observations commonly found that the magnitude of peak pressure and time scale of impulsive response vary significantly, depending on the shape of the incipient waves (Hattori et al., 1994; Hull and Müller, 2002) and the degree or types of aeration (i.e.,

dispersed small bubbles versus entrapped air pocket) in the breaking process (Bullock et al., 2007). Besides the impact pressure measurements, a small number of researchers selectively measured the velocity, acceleration, and impact force in the vicinity of the impact regions (i.e., Buchner, 1995; Oumeraci et al., 1995; Lugni et al., 2005 and 2010; Eswaran et al., 2011). In general, it was observed that the maximum impact pressure occurs near the still water level (SWL) with a magnitude of 1 to 2 times the hydrostatic pressure and the corresponding duration between the pressure rise and fall is in the order of 1 ms (e.g., Bagnold, 1939; Cooker and Peregrine, 1995).

While many characterized the impact load on a vertical wall based on the breaker type, disagreement exists among researches in the predictions of the high pressure region on structures and associated breaking condition due to wave impact (e.g., Oumeraci et al., 1993, 1995; Hattori et al., 1994; Hull and Müller, 2002). More specifically, Hattori et al. (1994) and Oumeraci et al. (1995) reported that the maximum pressure occurred on vertical walls at the SWL based on their laboratory experiments with three different types of breakers, namely the flip-through, small air pocket, and large air pocket cases. Hull and Müller (2002) reported that vertical locations of the maximum pressure shifted from above the SWL for the flip-though breaker to the SWL for the air-entrapment cases. Furthermore, it is generally accepted that the trapped air pocket between the advancing liquid volume and the vertical wall softens the direct impact from the liquid by providing a cushioning effect. However, it has also been reported that the entrapped air pockets or the flow aeration during the impact tend to expand the impact area (i.e., on the vertical extent of the wall) and lengthen the impact duration based on both laboratory and field measurements (Crawford et al., 1997; Bullock et al., 2004 and 2007). The resulting force and impulse are indeed comparable to that produced by a direct liquid impact from the wave impingement.

In spite of certain contradictions in pressure predictions, it is commonly perceived that such impact mechanism is a localized process; hence the magnitude and degree of the impulsiveness of the impact pressure vary significantly in both space and time, mainly due to the rapidly evolving impinging waves (Chan and Melville, 1988; Oumeraci et al., 1993; Chan, 1994). The knowledge on the wave impingement obtained from laboratory experiments has been somewhat limited mainly because of employed instruments, such as the point-measurement tools of pressure sensors and wave gauges, are often incapable of providing sufficient resolution to capture the full-field evolution of fast-varying breaking waves without costly instrumentation or burdensome efforts (Chan, 1994).

Recently, the advancement of image techniques provides great potential to tackle the sloshing problem. Laboratory experiments have been more extensively developed to measure flow kinematics and its relations with the dynamic impact on structures. Researchers started to use snapshot images of advancing waves and their subsequently impact on structures to study the problem. Evolution of the free surface and shape of the breakers were examined to find their relationship with the slamming pressures and forces on the structures (e.g. Chan, 1994; Hattori et al., 1994; Bredmose et al., 2003). Applying the particle image velocimetry (PIV) technique, researchers investigated flow velocities of the impacting waves and the subsequent jet formation (i.e., Oumeraci et al., 1995; Lugni et al., 2006; Eswaran et al. 2011). Prominent results on liquid sloshing were obtained by a set of work conducted by Lugni et al. (2006 and 2010) to investigate the kinematics and dynamic impact response of two-dimensional sloshing waves during the flip-through event.

Lugni et al. (2006) classified the impact mechanism into three modes depending on the wave breaking condition and degree of the aeration around the flip-through moment. They quantified the velocities and acceleration of the free surface flow during the first occurrence of the wave impact until the jet formation. They reported that the maximum horizontal speed of the advancing wave crest reached about 2.7C just before the wave crest impacting on the tank wall, and the maximum speed of the rising jet reached 9.0C right after the impact, where $C = \sqrt{gh}$ is the characteristic phase speed (C = 1.1 m/s with a still water depth h = 0.125 m in their experiment) based on the linear shallow water approximation. They further estimated the acceleration of the upward jet to reach an incredible magnitude of 1500g with g be the gravitational acceleration. Subsequently, Lugni et al. (2010) provided a more detailed examination on the flip-through process where the formation and evolution of air cavity during the sloshing impact at the tank wall plays a crucial role. In the study they chose the third impact wave against the first impact wave which was examined in their earlier paper in Lugni et al. (2006). They investigated the role of air compressibility and ullage pressure to the impact mechanism since the flow in the later impact was more violent with a greater degree of air entrapment between the wave front and the tank wall. They reported that the maximum horizontal velocity was about 2.3C before impact; whereas the maximum vertical velocity was about 3.6C and the maximum acceleration was about 100g at the initiation of jet formation. The work of Lugni et al. (2006 and 2010) provides perhaps the most concrete quantification on the kinematics of sloshing wave impact. The coverage of velocities and accelerations in their

measurements, however, were limited only to the moment before the vertical jet started to rise after the wave impact. The maximum velocities and accelerations reported from their 2006 work were noticeably greater than what was reported in their 2010 work. Although the data faithfully support the authors' conclusions, the measurements may need to be validated or at least compared with other equivalent studies; especially the violent sloshing flow that is known to notoriously affect PIV measurements due to the large amount of air bubbles. Therefore, flow kinematics as well as dynamic pressures of liquid sloshing may need to be further evaluated in a way that can account for the multiphase, turbulent nature of the impinging waves and up-rushing jets.

Ryu et al. (2005) developed the bubble image velocimetry (BIV) technique by combining the PIV and shadowgraphy methods for velocity measurements in gas-liquid flows by correlating textures formed by gas-liquid interfaces in the BIV images. The BIV technique was later applied in the measurements of green water flows on two-dimensional structures (Ryu et al., 2007a, 2007b; Ryu and Chang, 2008) and three-dimensional structures (Chang et al., 2011; Ariyarathne et al., 2012), wave breaking on a sloping beach (Pedrozo-Acuña et al., 2011; Rivillas-Ospina et al., 2012), and open channel aerated flows (Lin et al., 2008; Lin et al., 2012). The BIV technique has been proven to work well in measuring velocities in highly aerated flows and violent impact between the liquid and structures.

In the present study, velocity measurements using BIV and pressure measurements using pressure sensors at selected boundary locations were performed to investigate the kinematics and dynamics of liquid sloshing flows inside a partially filled rectangular container model undergoing a one-dimensional sinusoidal motion. The velocities of local flows were analyzed to examine their influence on local dynamic pressure on a side walls and the top wall of the container based on the measurements. The goal is to quantitatively obtain full-field flow velocities, and to investigate possible correlation between impact potential of the sloshing liquid kinematics and the dynamic response in term of pressure on the liquid container in simple oscillatory motion. The study may also provide quantitative data in velocities and pressures for physical and numerical model validations.

IV.2 Experimental setup

Experiments investigating the liquid sloshing kinematics and dynamics of a partially filled sloshing tank were carried out at the sloshing test facility in Pusan National University. A glass-walled rectangular tank model was placed on a computer-controlled platform that is capable of generating six degrees of freedom motion. The tank has dimensions of 0.79 m in length (L) and 0.48 m in width and height, while the motion platform was controlled to generate sinusoidal oscillation along the longitudinal axis as $\zeta = \zeta_0 \sin(2\pi f t)$ where ζ is the oscillatory displacement of the tank, ζ_0 is the amplitude of the displacement, and f is the frequency. Liquid motion inside a closed tank in periodic movement is dominated by the liquid filling ratio, the amplitude and frequency of the tank motion, and the geometry of the tank. For a rectangular tank in periodic motion, the modal frequency f_n of the liquid can be calculated from the linear potential theory as

$$f_n = \frac{1}{2\pi}\sqrt{\frac{n\pi}{L} g \tanh\left(\frac{n\pi h}{L}\right)} \tag{26}$$

where L is the longitudinal length of the tank, h is the still water depth, g is the gravitational acceleration, and n is the modal number. The resonance response of the sloshing liquid takes place near the lowest modal frequency f_1.

We investigated the hydrodynamic responses of the sloshing flow by choosing a filling ratio at 30% and an excitation frequency at the corresponding f_1 mode as shown in Table IV-1. When the tank was filled at the 30% of the tank depth (i.e., h = 0.144 m), the standing wave-like flow condition took place at its natural frequency, producing a highly aerated violent turbulent flow as wave impact occurred. Table IV-1 summarizes the test parameters and the characteristic scales of the resulting sloshing flow, including the characteristic velocity based on the sloshing wave phase speed $C = \sqrt{gh}$, the characteristic pressure based on the initial-depth hydrostatic pressure ρgh, and the displacement amplitude ζ_0 of the oscillatory tank.

Table IV-1 Test condition of liquid sloshing

Filling depth h (m)	Filling ratio h/H (%)	First-mode frequency f_1 (Hz)	Excitation frequency f (Hz)	Characteristic wave period T (s)	Characteristic phase speed C (m/s)	Hydrostatic pressure ρgh (kPa)	Tank displacement ζ_0 (mm)
0.144	30	0.715	0.715	1.40	1.2	1.4	50

In the experiments, the BIV technique was employed to obtain the sloshing flow velocities as well as the tank displacement and free surface profile. The BIV system features a high-speed camera that has a 1024×1024 pixel resolution, a 10-bit dynamic range, a 1200 Hz maximum framing rate, and an illumination system formed by four 600W light bulbs. The high-speed camera was mounted with a 105 mm focal lens with the aperture set at f/1.8 and placed at 3.9 m in front of the tank. A translucent plastic sheet was attached to the rear wall of the glass tank to form a LED-like backlit plane illuminated by a pair of the lights for creating bubble shadow images. Another pair of lights was installed on the front side of the tank with a 60-degree angle to the normal in order to produce more intensity variation in the shadowgraph images captured by the camera. Figure IV-1 shows the setup of the sloshing tank sitting on the motion platform and the coordinate system. Note that we fixed the coordinate system with x being in the horizontal longitudinal direction and z in the vertical upward direction and the origin (x, z) = (0, 0) locating at the center and bottom of the tank.

The camera recorded images with a field of view (FOV) of 0.56×0.56 m^2 that covers the full height but slightly greater than one-half of the tank from the right side wall, as shown in Figure IV-1a. The center of the BIV measurement plane is 0.10 m behind the glass wall. The camera was operated at 1000 frames per second throughout the experiments. The images were first inverted then cross-correlated to obtain the instantaneous velocities using PIV software from LaVision Inc. The velocity determination was started with an initial 64×64 pixel interrogation area and then reduced to a final 32×32 pixel interrogation area with a 50% overlap between adjacent interrogation areas. This results in an 8.75 mm spacing between adjacent velocity vectors. Spurious vectors were removed by applying median filter. The BIV experiments were repeated 20 times to obtain mean velocities using the ensemble average method.

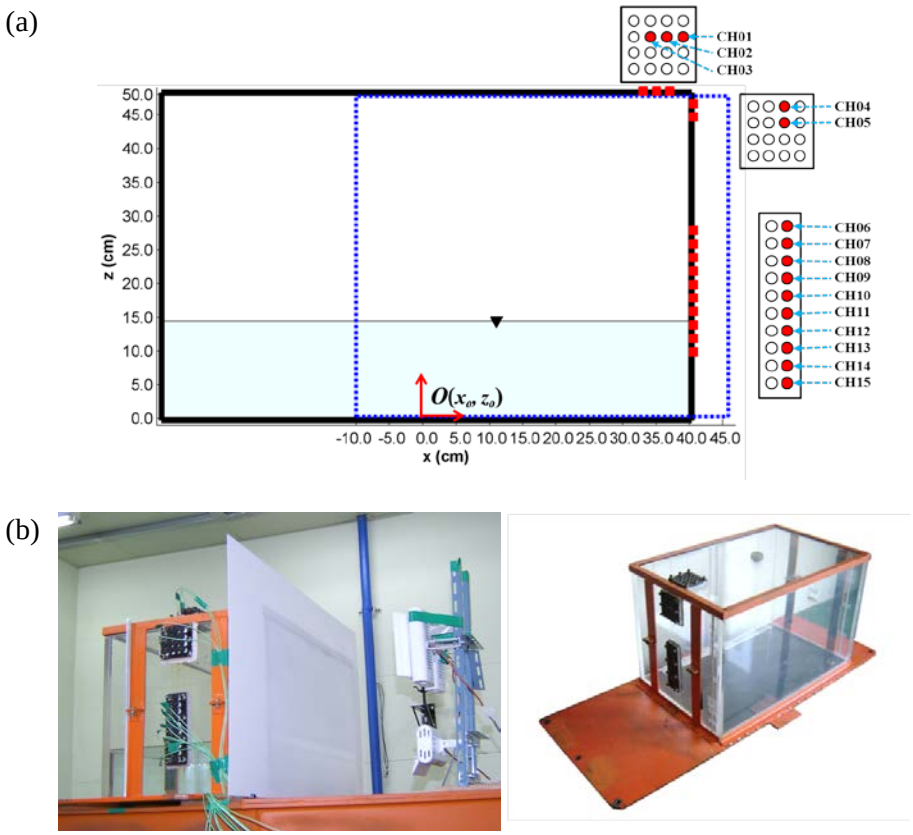

Figure IV-1 Experimental setup and coordinates. (a) Sketch of the tank with locations of pressure sensors on the side and top walls of the tank, the coordinate system, and the FOV for the BIV measurement (dotted line). (b) Photos of the tank and BIV illumination arrangement (left) and sloshing tank (right). Note that the tank moves sinusoidally in the x direction so the FOV represents the instant when the tank is at the mid position at $\zeta = 0$.

The BIV technique directly uses air-water interfaces in the image without the use of a laser for illumination. The measurement plane is controlled by minimizing the depth of field (DOF) within which objects (i.e., air bubbles and water droplets in this case) are in focus and sharp so carrying more weight (i.e., higher intensity) in the correlation process for velocity determination. The DOF was controlled by adjusting the camera aperture. According to Ray (2002), the nearest limit is $R = \ell f_c^2 / \left(f_c^2 + N \ell C_c \right)$ and the farthest limit is $S = \ell f_c^2 / \left(f_c^2 - N \ell C_c \right)$, where ℓ is the distance between the camera and the focal plane, f_c is the camera focal length, C_c is the circle of confusion of the camera, and N is the f-number of the camera aperture. The DOF is calculated as $D = S - R$. In the present study, ℓ = 4.0 m, f_c = 105 mm, N = 1.8, and C_c = 0.03 mm. created by

the limited DOF can be estimated as $\varepsilon = D/2\ell$. Accordingly, the DOF is D = 0.16 m and the associated error is ε = 2.0%. More details on BIV and its errors can be found in Ryu et al. (2005).

In addition to velocity measurements, pressures on the right side wall and on the top wall of the tank were also measured using a total of 15 piezoresistive type sensors from Kistler Co. The sensors have a diameter of 9.5 mm and a natural frequency higher than 70 kHz. The sensors were placed along the centerline of the tank and termed CH01 to CH15 as shown in Figure IV-1. CH01–CH03 were on the top wall near the right upper corner where the overturning jet up-rushed and directly impacted at a nearly normal angle during the sloshing process. CH03 is 30 mm from the right side wall and the spacing between the adjacent sensors is 20 mm. CH04–CH05 were on the side wall near the upper right corner where the sloshing flow was mainly in the tangential direction (i.e., flow ran up along the wall). CH04 is 30 mm below the top wall and the spacing is 20 mm between these two sensors. CH06–CH15 were on the lower side wall where the sloshing flow impacted in mostly a normal angle. Again the spacing is 20 mm between the adjacent sensors with the lowest sensor CH15 located at 100 mm above the tank bottom. All the sensors were flush with the inner surface of the tank walls and sampled at 20 kHz throughout the experiments. Note that the still water depth h reached only up to CH13 for the present 30% filling ratio case.

IV.3 Flow kinematics

Figure IV-2 shows time history of the tank displacement. The initial tank motion was ramped up with a hyperbolic increase in the amplitude before it developed a complete sinusoidal motion of $\zeta/\zeta_o = \sin(2\pi t/T)$ with an amplitude of ζ_o = 50 mm from $t = 2.5T$. The motion of the tank during the ramp-up period when $t < 2.5T$ followed $\zeta/\zeta_o = a\sqrt{t/nT} + b$ where a = 53.1, b = 4.45, and n = 2.50. The motion of the tank was obtained by tracing the displacement of the right-side wall in the BIV images at each time instant. A comparison between the desired tank motion and the recorded displacement confirms that the tank achieved a quasi-steady sinusoidal motion after $t = 2.5T$. Thus, we considered only data from $t/T > 2.5$ in all subsequent analysis in the present study.

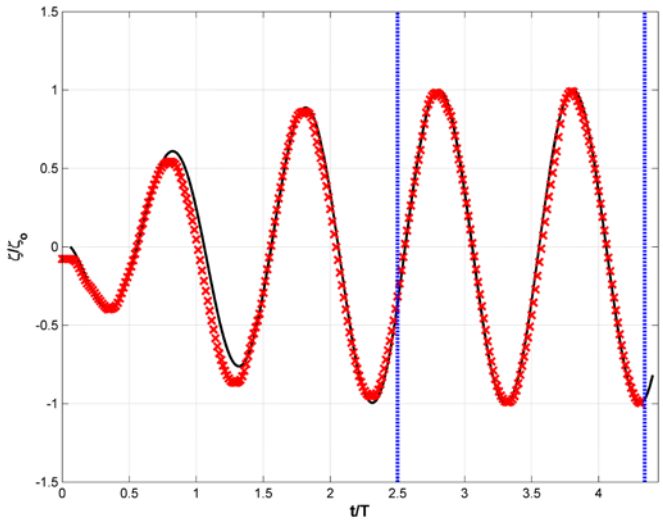

Figure IV-2 Normalized time history of tank displacement. Solid line: input forcing signal for platform motion $\zeta/\zeta_o = \sin(2\pi t/T)$ including an initial ramp. The motion of the tank during the ramp-up at $t < 2.5T$ followed $\zeta/\zeta_o = a\sqrt{t/nT} + b$ where a = 53.096, b = 4.45, and n = 2.5. Solid line: desired tank motion; ×: recorded tank displacement based on BIV images. The two dotted lines at t/T = 2.5 and 4.5 indicate the interval used in the analysis after the tank motion achieved a stable sinusoidal motion.

Figure IV-3 shows the evolution of the mean velocities as well as mean free surface of the sloshing waves before and after the impact on the right-side wall at the fourth cycle (t/T > 3.5 in Figure 2). Since the BIV method works only when air bubbles or air-water interfaces present, some velocities were not available due to a lack of bubbles or were manually removed through masking due to unknown uncertainty when fewer bubbles present (by inspecting the mean images). Note that only every other row and every other column of the obtained velocity vectors were plotted in each panel (i.e., only one quarter of the total vectors were plotted) so they are more legible.

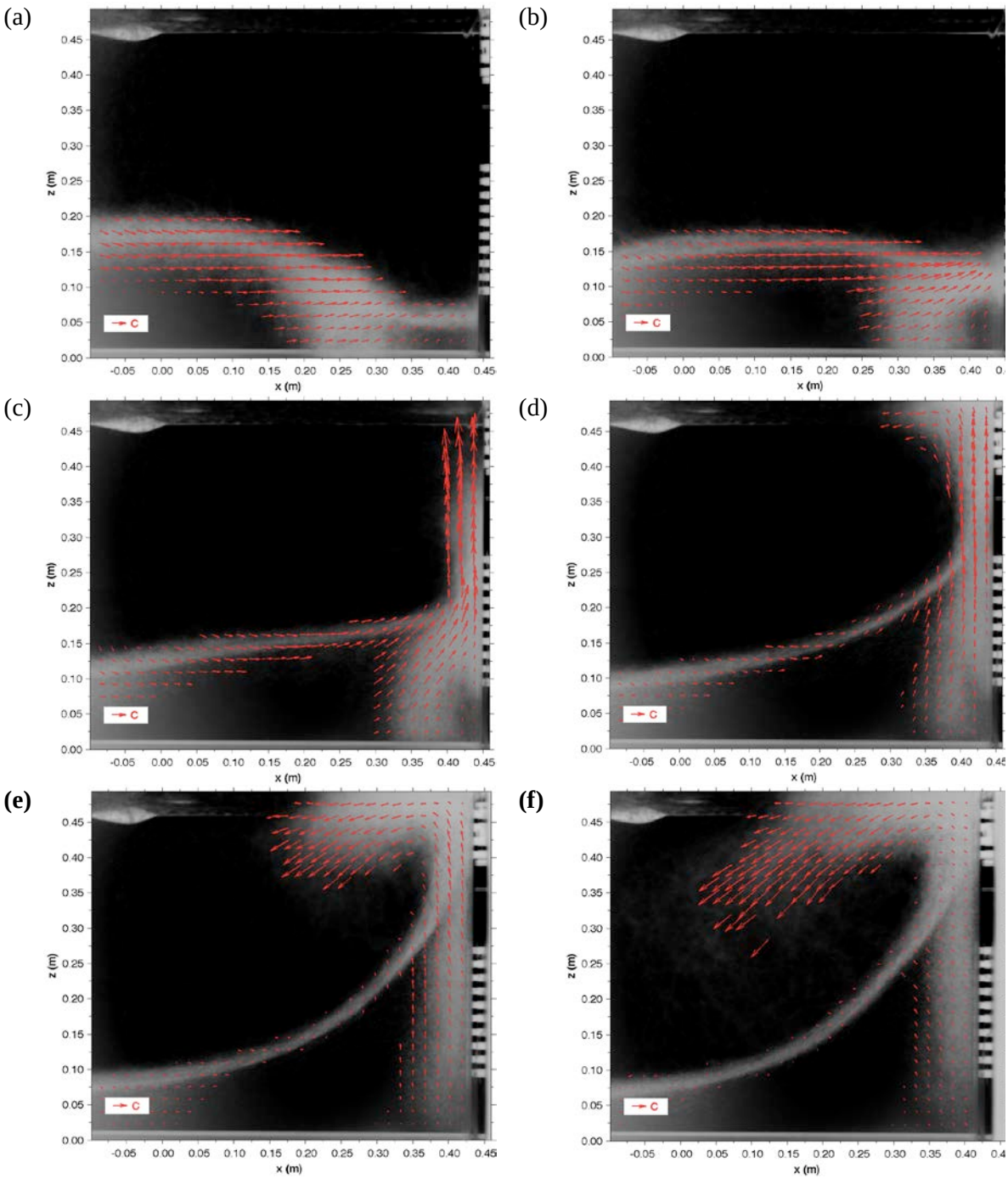

Figure IV-3 Evolution of the sloshing waves at t/T = (a) 3.74, (b) 3.79, (c) 3.84, (d) 3.89, (e) 3.94, (f) 3.99, (g) 4.04, (h) 4.09, (i) 4.14, and (j) 4.19. Note that only approximately one-half of the tank is covered, as shown by the FOV in Figure IV-1a. The velocities and images are ensemble-averaged values and the images were inverted (so bubble shadows and air-water interface become bright). Only velocity vectors in every other row and every other column were plotted (i.e., only one-quarter of total velocity vectors were plotted).

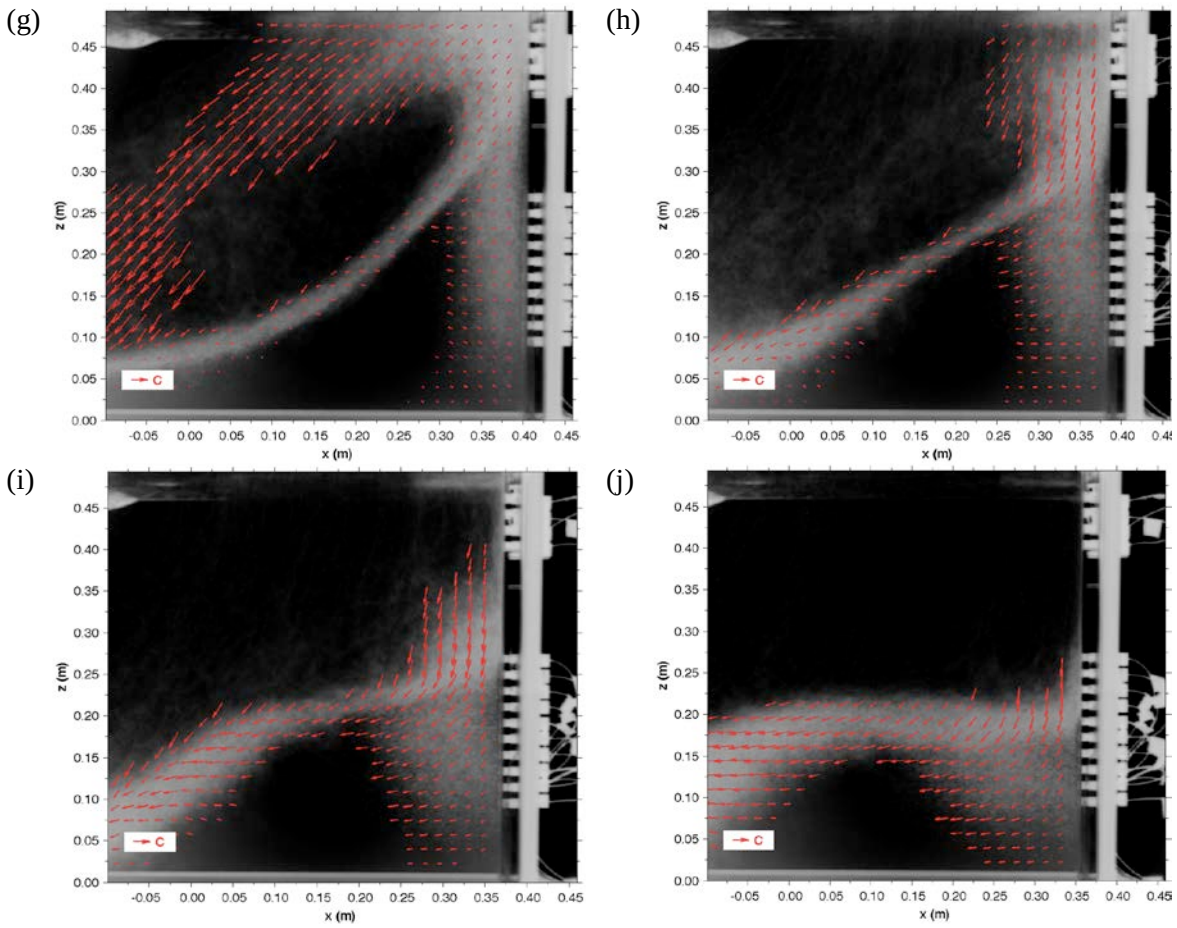

Figure IV-3 Continued

In the sloshing flow, the sloshing wave advanced predominantly in the *x* direction in phase with the direction of the tank motion when the tank was moving to the right (Figure IV-3a and Figure IV-3b). As the sloshing wave traveled past the midpoint in the longitudinal extent of the tank (i.e., at $x = 0$), the horizontal velocity at the wave crest gradually increased and reached $1.6C$ at $t/T = 3.74$ before impacting the wall, as shown in Figure IV-3a. At $t/T = 3.79$ in Figure IV-3b, the "flip-though" event (Peregrine, 2003) took place when the motion of the tank temporally stopped as it reached its maximum displacement and was about to change its direction. As the rigid tank wall prevented of the flow from further horizontal advance, the flow rapidly turned upwards and changed its momentum to the vertical direction, forming an up-shooting jet at $t/T = 3.84$ in Figure IV-3c. When the tank was about to move to the left at $t/T = 3.89$ (Figure IV-3d), the momentum of the flow near the wall transferred to the rising jet; thus

the flow direction dominantly became vertical toward the upper corner of the tank. The impact process of the sloshing wave on the right side wall and the consequent development to the vertical jet will be discussed with more details later. The thickness of the jet seemed to increase in Figure IV-3d after the impact with the side wall that increased its air entrainment. Even though the jet upward velocity was high, the jet was indeed decelerating with the acceleration approximately equal to $-g$ due to the effect of gravity, obtained by check the jet front velocities at different times during the runup. The wall area beneath the still liquid free surface seemed only subject to moderately pressure because the wave trough at the side wall started to rise prior to the arrival of the wave front, causing the wave crest to arrive at the SWL upon impact.

After the jet impacting the top wall of the tank, its momentum changed to the $-x$ direction along the top wall. While traveling to the left, the jet started to break and free fall with the liquid in mostly the droplet form (Figure IV-3e–g). As the sloshing liquid used up its kinematic energy that fueled the jet rise and redirecting the flow to the $-x$ direction, the runup process slowed down and the elevated sloshing liquid fell from the top wall due to gravity as shown in Figure IV-3h. Subsequently, the elevation of the free surface near the right tank wall quickly decreased (Figure IV-3i) due to run-down while the tank was moving to the left; the sloshing wave started to move to the $-x$ direction. After Figure IV-3j at $t/T = 4.19$, the flow again became dominantly horizontal in response to the motion of the tank and the post run-down process. As the wave moving toward the left-side wall, the impact and runup process of the sloshing flow at the left side wall should be similar to what occurred near the right side wall, shown in Figure IV-3, due to the symmetrical configuration and periodic movement of the tank.

Figure IV-4 shows the detailed mean velocities of the sloshing flow superimposed on instantaneous images in the process when the sloshing wave was impacting the right side wall and developing into a vertical jet in between $t/T = 3.74$ and $t/T = 3.84$ (between Figure IV-3a and Figure IV-3c). At $t/T = 3.74$ in Figure IV-3a, the wave trough encountered the side wall at an elevation around $z = 0.08$ m which is much lower than the SWL at $z = 0.144$ m. Meanwhile the propagating wave crest developed into a steep front (Figure IV-4a). This fast moving wave crest and the rapidly rising trough converge at a point on the wall at the SWL at around $t/T = 3.78$ (Figure IV-4b). Note that for the present $f = f_1$ condition, the overturning wave crest encountered the wall before impinging to its front water surface. Indeed the wave front made contact with the side wall slightly before the formation of a overturning jet of breaking wave while the flip-through of the wave trough has started, resulting in the size of the entrapped air pocket between

the wall and the wave front being unnoticeably small. After the impact, the jet flow continued to rise toward the top wall (Figure IV-4c – d), reached a speed of 3.4*C* at the front at *t/T* = 3.84 (Figure IV-3c), until deflected by the top wall.

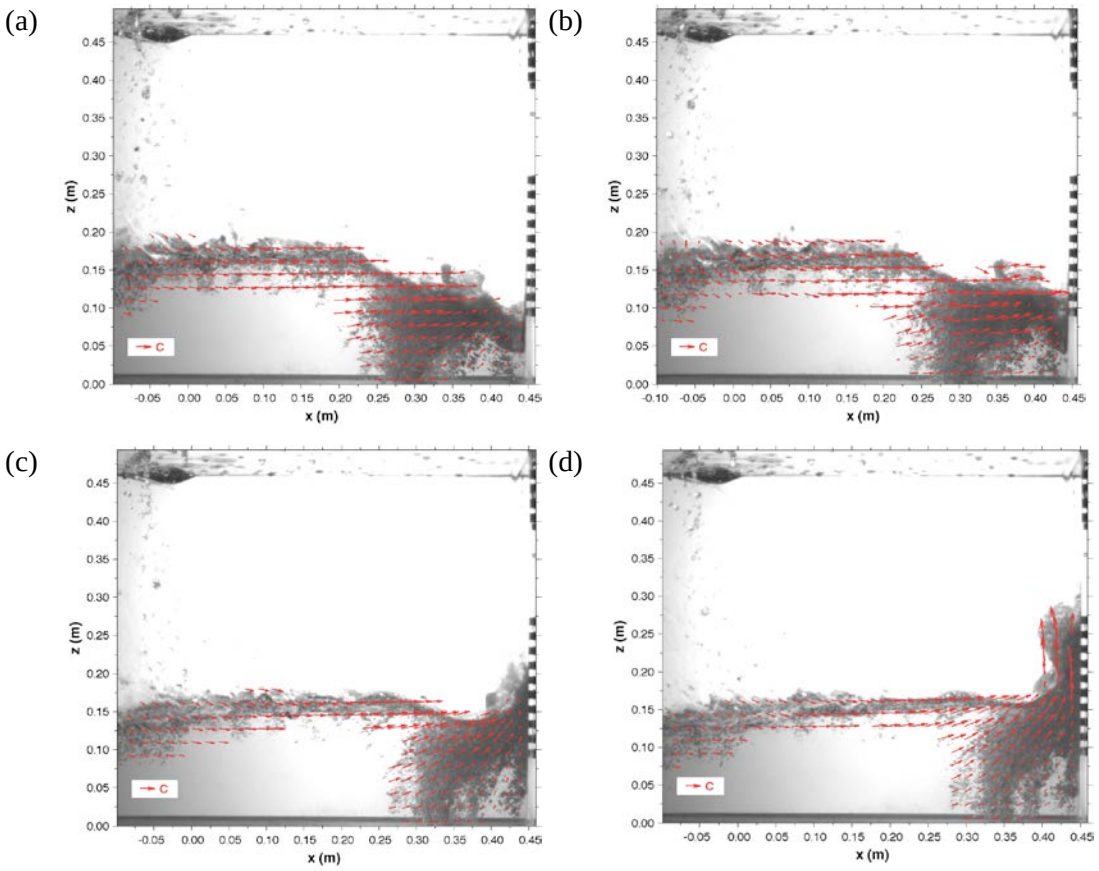

Figure IV-4 Sloshing wave impacting on tank side wall at t/T = (a) 3.76, (c) 3.78, (d) 3.80, and (e) 3.82. Note that the velocities are ensemble-averaged mean quantities but the images are original instantaneous snapshots.

Based on Figure IV-3 and Figure IV-4, some interesting observations are summarized below. The velocities near the front crest of the sloshing wave during the wave advancing stage before impacting the side wall were predominantly in the horizontal direction, reaching a maximum magnitude of 1.6*C* (Figure IV-3b). This magnitude is lower than the magnitude of 2.3*C* reported by Lugni et al. (2010). Interestingly, the magnitude of 1.6*C* is similar to the 1.5*C*

maximum horizontal velocity found in Ryu et al. (2007b) measured before a plunging breaking wave impinging on a rectangular structure and causing green water on the structure. After the sloshing wave impacted on the side wall, the maximum runup velocity in the present study reached 3.4*C* (Figure IV-3c) near the front of the up-rushing jet. This velocity is very close to the maximum velocity of 3.6*C* reported by Lugni et al. (2010). Similarly, the velocity of 3.4*C* is also very close to the maximum upward velocity of 2.9*C* reported by Ryu et al. (2007b) measured during the runup stage after the breaking wave impacting on the vertical wall of the rectangular structure in the green water study. Even though liquid sloshing is quite different from green water, these maximum horizontal and vertical velocities are surprisingly similar.

Figure IV-5 shows the maximum velocities U_{max} and W_{max} during the sloshing process which may be related to high momentum and thus high impact forces, and their temporal variations with respect to the tank motion over the two quasi-steady periods shown in Figure IV-2. In the figure, a greater magnitude of W_{max} in the first quasi-steady cycle (t/T = 2.5–3.5) was observed (at t/T = 2.84) in comparison to that in the second quasi-steady cycle (t/T > 3.5); whereas the magnitude of U_{max} observed in both cycles were comparable to each other. By examining the BIV video images, it was observed that the propagating wave toward the right-side wall in the second quasi-steady cycle had more interaction with the reflecting wave and falling droplets generated by the first quasi-steady cycle. On the other hand, the wave in the first quasi-steady cycle was less disturbed by reflection and droplets created by the previous cycle since the tank motion in the previous cycle was not yet fully developed (see the Figure IV-2). Accordingly, the sloshing wave in the first quasi-steady cycle was less interfered by the opposite-direction momentum left from the previous cycle, resulting in less disturbed wave propagation toward the right-side wall that in turn resulting in higher vertical velocities in the up-rushing jet as shown in Figure IV-5. We hence assumed that the sloshing kinematics observed during the second quasi-steady cycle in Figure IV-5 is more likely to be fully developed so all discussion, including the velocity maps in Figure IV-3 and Figure IV-4, was based on that cycle.

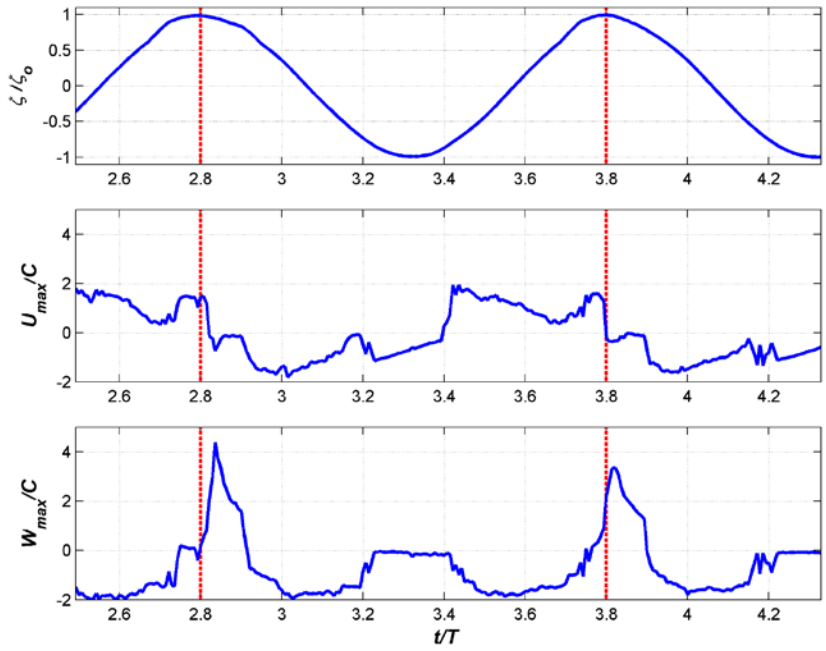

Figure IV-5 Time series of tank displacement ζ and maximum mean velocities U_{max} and W_{max}. The vertical dashed lines denote the instants when the tank displacement reached the rightmost position.

By further examining Figure IV-3 to Figure IV-5, it was found that U_{max} gradually increased to 1.6C at t/T = 3.79 (and at t/T = 2.81) in the direction of the tank motion until the tank reached the rightmost position at $\zeta/\zeta_o = 1$. When the tank appeared to be motionless at around t/T = 3.80 (and t/T = 2.80), U_{max} rapidly reduced to near zero and remained near zero for about 0.1T. Due to conservation of momentum, it corresponded to the moment when W_{max} sharply increased, indicating that the advancing horizontal momentum is being transferred to the vertical direction thus potentially created a large pressure and forces to the tank side wall. After a sharp increase of W_{max} to 3.4C at t/T = 3.82 (and to 4.4C at t/T = 2.84), W_{max} decreased due to gravity and the jet front reached the tank top wall. W_{max} then decreased rapidly after the uprising jet lost its momentum. The rundown process immediately started and U_{max} started to increase in the $-x$ direction due to the transfer of momentum in the rundown process plus the tank motion toward the left. The observation based on the maximum velocities in Figure IV-5 was also observed from the velocity maps in Figure IV-3. Moreover, it was found that the U_{max} reached its maximum value at about 0.02T (~ 0.03 s) before the tank started to reverse its direction, and

W_{max} reached its maximum value at about 0.02T after the tank started to reverse its direction. Such rapid transition in momentum direction and magnitude accompanied with the violent motion of the free surface may imply large impact forces between the sloshing waves and the rigid tank structure in the process.

IV.4 Impact pressure

To investigate the dynamic aspect of the sloshing flow, pressure measurements were taken using fifteen pressure sensors mounted along the longitudinal centerline of the tank on the right-side wall (CH04–CH15) and the top wall (CH01–CH03) as shown in Figure IV-1. Note that the sloshing wave focused at around CH13, close to the SWL at z = 0.144 m, at t/T =2.8 and 3.8 (see Figure IV-3b and Figure IV-4b), and the uprising jet directly slammed CH01 to CH03 mounted on the top wall of the tank (Figure IV-3c to Figure IV-3d). The wall regions where the violent impact occurred were examined based on the pressure measurements while the nearby flow velocities were used to find possible correlation between the impact pressures and the velocities. These violent interactions have potential to cause damages to the tank structure.

Figure IV-6 shows pressures measured at selected locations on the side wall and the top wall. Note that the pressures were scaled by the hydrostatic pressure ρgh (= 1.41 kPa). After examining the pattern, pressures from the fifteen sensors were categorized into three groups, termed groups A, B, and C, based on their relative location to sloshing impact and their orientation to sloshing flow direction in the sequential order of occurrence. The pressure time histories for CH13–CH15 in Figure IV-6a are categorized as *group A*; these sensors located at and below the SWL in the direct impact zone of the breaking wave. The pressure pattern is similar to the typical "church roof" profile (Peregrine, 2003). They were first subject to impulsive pressure with a high peak value around 5 to 10 ρgh at approximately t/T = 2.8 and 3.8 when the breaking wave impinged the side wall (see Figure IV-3b), immediate followed by relatively uniform pressure with a magnitude about ρgh that lasted about 0.4T (until t/T = 3.2 and 4.2 when the tank moved to the leftmost location). Subsequently, a great portion of the liquid volume moved toward the left side wall, lowering the water depth near the right side wall to below CH15 so the pressure reading was essentially zero. Pressure time histories for CH09–CH12 (not shown here) showed a similar pattern as that at CH13–CH15 except the magnitudes of the impulsive peak at approximately t/T = 2.8 and 3.8 were much less pronounced. Such impact patterns were often observed on sensors mounted on the side wall above the wave impact

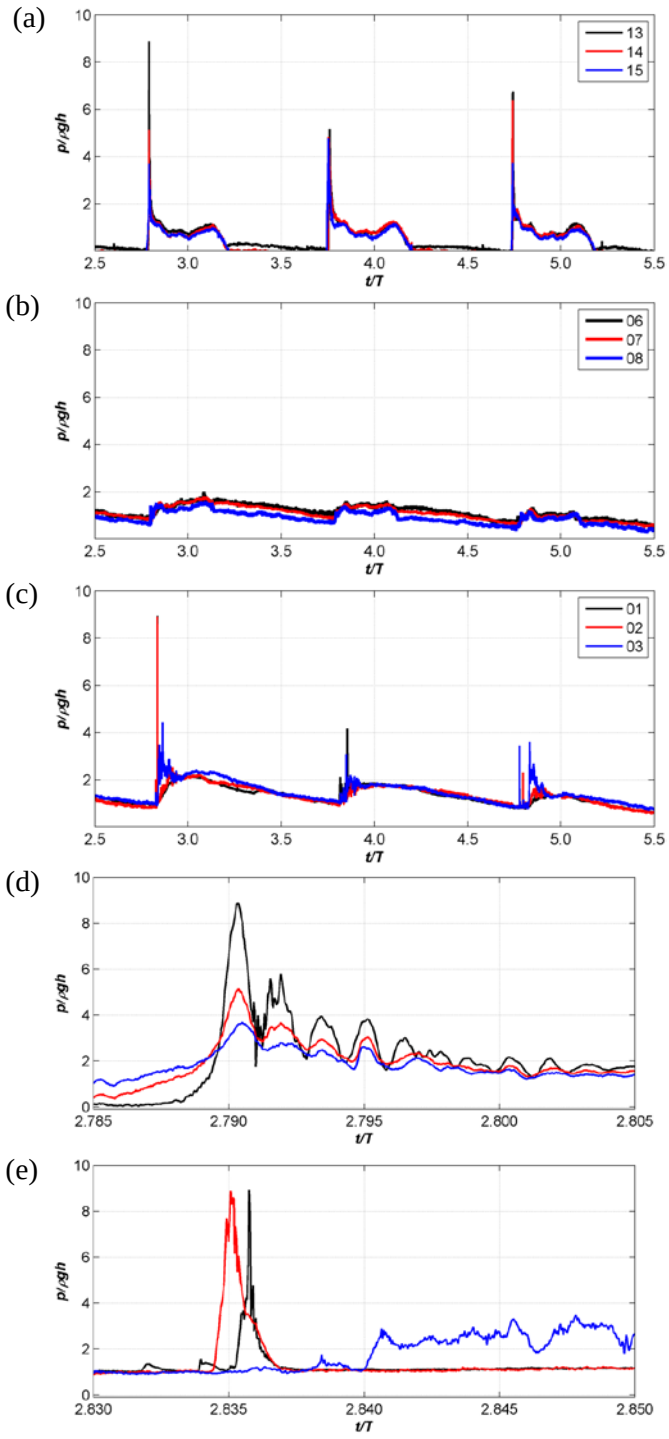

Figure IV-6 Time histories of pressures on tank walls: (a) group A on side wall below the SWL, (b) group B on side wall above the SWL, (c) group C on the top wall. (d) Close-up view of pressure time history corresponding to the first impact in (a). (e) Close-up view of pressure time history corresponding to the first impact in (c).

zone but on the way of the uprising jet formed after the impact. Since the flow velocities were dominantly in the vertical direction (Figure IV-3c) which is tangential to the wall and thus to the surface of the sensors, the jet flow imposed little dynamic effect to the sensors so relatively low peak pressures were recorded from CH09–CH12. These pressures are in transition from group A to group B.

Figure IV-6b shows the pressure time series for CH04–CH08 above the SWL on the side wall. Smooth profiles, little variations with a magnitude around ρgh, as if they were under the hydrostatic pressure, were observed in the figure; these pressures were categorized as *group B*. These sensors were on the way of the uprising jet with dominant velocities tangential to the surface of the sensors. Figure IV-6c shows the pressure time histories for CH01–CH03 mounted on the top wall. These pressures were categorized as *group C*; the pressures appeared to be more random and less repeatable, not only among the 3 pressures but also among their peak values. The peak values in group C seem to be comparable with that in group A, but slightly less pronounced. Indeed the pattern of peak pressures in group C is quite different from that in group A (more to follow). Unlike the near zero low pressure zero observed in group A, the pressures in group C seemed never return to zero. The reason is not clear, but based on the PIV video images we suspect that the "wet ceiling" may be the cause. Due to a large amount of droplets created from wave impacts, water stayed on the top wall for quite a long time. Water continued to drop for a few minutes even after the tank motion completely stopped at the end of each run. The water film seemed to leave some pressure on the sensors but we were not sure if that caused the low reading to close to ρgh, somewhat similar to the low pressures observed in group B in Figure IV-6b.

Figure IV-6d shows detailed pressure time series for group A (CH13–CH15) at the impulsive impact at around t/T = 2.8 in Figure IV-6a. Pressure oscillation lasting for about $0.005T$ (or 7 ms) during the impact was observed, indicating there were small air pockets (observed by examining the BIV video images and discussed in the previous section) entrapped between the wall and the nearly vertical sloshing wave front before impinging the side wall. This type of pressure pattern is similar to what was observed by Lugni et al. (2006) in their air-entrapment case during the flip-through event of breaking sloshing waves. The impulsive pressures started to oscillate immediate after the fast rising peak caused by the direct wave impact and continued with an oscillation period of about $0.0014T$ (or 500 Hz). The total period of the pressure impact between the incipience of the peak rise and the recovery to the initial

condition (i.e., $2.78 \leq t/T \leq 3.20$ or $3.75 \leq t/T \leq 4.20$) lasted about $0.4T$ to $0.5T$ (Figure IV-6a). Such pressure time scale is in agreement with that reported by other experimental studies. For example, Peregrine (2003) reported that violent peak pressures act for about 1 millisecond in laboratory observation and Lugni et al. (2006) estimated the resonance frequency of the peak oscillation to be 650 Hz. The magnitude of peak pressure and the degree of oscillation were the greatest at the highest location in group A (all sensors were at or below the impact point on the wall) due to the high velocity at the wave crest, and decreased toward the lower locations on the wall. We indeed recorded the pressure time histories over twelve sloshing periods (not shown here) and found a fairly repeatable pressure profile for this group of sensors located below the SWL, except the magnitude of the peak pressures varied between $5\rho gh$ and $20\rho gh$.

Figure IV-6e shows the typical pattern of impulsive pressures among a total of twelve measured sloshing periods in group C (CH01–CH03). A sudden rise and fall of impulsive pressures was observed at CH01 and CH02 mounted on the top wall. The oscillation pattern observed at CH13 at SWL was not seen here. The average rising time of the impulsive pressures was about $0.001T$ (1 ms) with an average peak pressure of about $10\rho gh$. Note that the shape of the pressure time histories at CH01 and CH02 is comparable to what Lugni et al. (2006) observed from a pressure sensor mounted on the side wall at the SWL. On the other hand, the pressure at CH03, located close to the upper right corner of the top wall, in Figure IV-6e demonstrated a completely different pattern from the other two adjacent sensors (CH01 and CH02) on the top wall. Its pressure showed random fluctuations that lasted a much longer duration with a much lower pressure magnitude of about $3\rho gh$. The shape of the pressure time history at CH03 is comparable to what was observed during the wall impact of broken wave in Lugni et al. (2006) that involved a highly aerated flow interacting with a wall. Further inspection of the BIV video images and velocity fields (i.e., Figure IV-3c to Figure IV-3d) found that CH01 and CH02 that are a short distance away from the side wall subjected to direct impact of the uprising jet front; whereas the portion of the jet closer to the side wall which impacted CH03 appeared to contain a higher aeration (based on the shadow intensity difference in the BIV images). We therefore believe that a higher void fraction consisting of small air bubbles present in the up-rushing liquid jet might produce a cushioning effect that alleviates the dynamic impact from the jet (occurred at CH03). The mechanism is different from that with air pockets entrapped between the wave crest and the side wall (occurred at CH13–CH15) and producing oscillating impact pressures.

IV.5 Impact pressure versus velocity

The dynamic pressures from the liquid sloshing flow have been shown to vary from location to location as well as from cycle to cycle, mainly depending on the local shape and velocity and thus the momentum of the approaching wave or up-rushing jet in contact with the structure. Since the dynamic pressures are mainly caused by the change of flow momentum, it is logical to connect the dynamic pressures on the walls and corresponding kinematics of the sloshing flow and to find if a correlation between the impact pressures and the sloshing velocities exists.

Figure IV-7 shows the side by side plots for the measured group A (CH11–CH13) and group C (CH01–CH03) pressures and their corresponding mean velocities. The velocities were calculated based on the average values over 5 velocity vectors, distributed in a cross-shaped pattern within a 17.5 mm by 17.5 mm windows in front of each pressure sensor. Hereafter we refer the averaged local mean velocity simply as the local velocity. Using such an area for local velocity is because pressures were measured over a circular area of 9.5 mm in diameter (the surface area of each sensor) and to smooth out possible errors (discussion will follow). According to Figure IV-3, the local horizontal velocities were plotted against the pressure readings from sensors on the side wall (CH11–CH13); whereas the local vertical velocities were plotted against the pressure readings from sensors on the top wall (CH01–CH03). The underlying assumption is that the high dynamic impacts in the pressure readings were delivered mainly through a change of magnitude and direction of the predominant momentum in the direction aligned with that of each sensor surface after the impacts. The broken lines in the local velocities in Figure IV-7 indicate no liquid velocities (i.e., no water) in the small area in front the corresponding sensor.

The local velocities in Figure IV-7 show a high similarity profile but different magnitude among measurements in each group. The local velocities of the uprising jet reached a maximum vertical velocity of 3.0C near CH02, while the sloshing wave traveled with a maximum horizontal velocity of 1.4C near CH12. These maximum local velocities are slightly lower than the maximum velocities of 3.4C and 1.6C found in Figure IV-3 and Figure IV-4, attributed to the average of five velocity vectors near each sensor. Averaging 5 points in a “plus” shape to represent the impact velocity is because of large velocity variation at the wave focusing stage (Figure IV-3b, Figure IV-4a and Figure IV-4b) near the pressure sensors in group A (CH11–CH15). Choosing a single velocity vector right in front of each sensor does not really represent the local sloshing velocity since such a near wall velocity is in general lower than its neighboring

vectors due to the wall effect and the spatial resolution of the BIV measurements. The two peak velocities over the two periods in each panel in Figure IV-7 do not differ much, but the corresponding two peak pressures are quite different. As observed in Figure IV-6a and Figure IV-6c and discussed earlier, "cushioning" effects produced by bubbles in the flow and air pockets between the wave front and the side wall may be the cause.

A practical application of flow kinematics is to relate it with the dynamic impact pressures. Figure IV-7 demonstrates the impulsive pressures occurred coincidentally with the impingement of the high velocities normal to the sensor surface at each pressure sensor in groups A and C. Furthermore, Figure IV-6b implies only normal velocities to the sensor surfaces would create high dynamic pressures; the high velocities tangential to the wall (and therefore the sensor surfaces) did not result in noticeable pressure impulses. The observation suggests that the local normal velocities to the walls are related to the high impact pressures. Since pressures are relatively low except at the impulsive-impact incidents, we followed the approach in Ariyarathne et al. (2012) by correlating the peak pressure, $p_{\max}$, with the maximum kinetic energy, $\rho U_{\max}^2$ or $\rho W_{\max}^2$, depending on the orientation of each sensor, i.e.

$$p_{\max} = c_i \rho U_{\max}^2 \qquad \text{or} \qquad p_{\max} = c_i \rho W_{\max}^2 \tag{27}$$

where c_i is the impact coefficient. Accordingly, $p_{\max}$ at CH11 through CH15 located on the side wall were correlated with $\rho U_{\max}^2$, while $p_{\max}$ at CH01 through CH03 on the top wall were correlated with $\rho W_{\max}^2$. The pressure records from sensors CH04–CH10, located on the side wall above the SWL, did not show eminent impulsiveness in pressures when the high-velocity overturned jet impinged on the side wall as demonstrated in Figure IV-6b. At those sensors the flow direction was mainly tangential to the surface of the side wall so they lacked the needed dynamic impact to generate high pressure impulses.

Accordingly, the relation between the dynamic impact pressures and the corresponding flow kinematics was examined using the pressures and the local velocities at sensors CH01–CH03 and CH11–CH15. The local peak velocities were scaled by the wave phase speed and shown as $\beta = V_{\max} / C$ in Table IV-2 in which V_{max} is the magnitude of U_{max} or W_{max}. The two values for each pressure sensors are the resulting peaks in the first quasi-steady cycle and the second quasi-steady cycle as show in Figure IV-7. For CH11–CH15 on the side wall, β varies between 0.7 and 1.4 with an average value of 1.0. The highest β value occurred at CH12 located at immediately

above the SWL. For CH01–CH03 on the top wall, the β values are much higher – varying between 1.9 and 3.0 with an average value of 2.4.

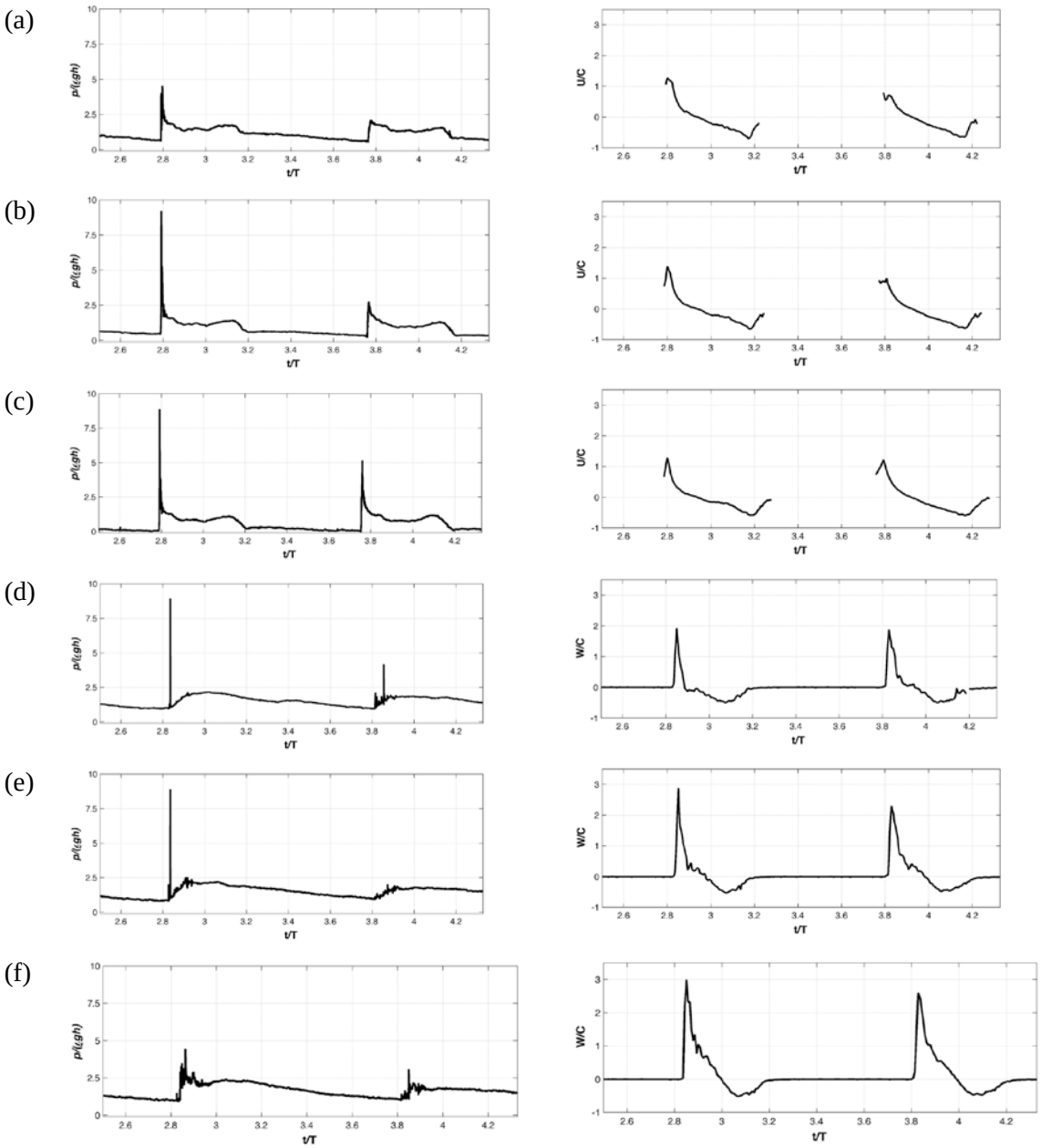

Figure IV-7 Local velocities and pressure time series: group A pressures (left column) on the side wall for (a) CH11, (b) CH12, and (c) CH13 and corresponding local horizontal velocities (right column); group C pressures on the top wall for (d) CH01, (e) CH02, and (f) CH03 and corresponding local velocities.

Table IV-2 Peak values in the pressure and velocity measurements and impact coefficients

CH	p_{max} (kPa)	$\frac{p_{\max}}{\rho C^2}$	$\beta = \frac{V_{\max}}{C}$	ρV^2_{max} (kPa)	$\frac{\rho V^2_{\max}}{\rho C^2}$	c_i	c_i'
01	12.6	8.9	1.9	5.2	3.6	2.4	8.9
	5.9	4.2	1.9	5.0	3.6	1.2	4.2
02	12.6	8.9	2.9	11.7	8.4	1.1	8.9
	2.8	2.0	2.3	7.5	5.3	0.4	2.0
03	6.3	4.4	3.0	12.7	9.0	0.5	4.4
	4.3	3.1	2.6	9.5	6.8	0.5	3.1
11	6.4	4.5	1.3	2.3	1.6	2.8	4.5
	3.0	2.1	0.8	0.9	0.6	3.4	2.1
12	13.0	9.2	1.4	2.7	1.8	4.8	9.2
	3.9	2.8	1.0	1.4	0.9	2.7	2.8
13	12.5	8.9	1.3	2.3	1.6	5.4	8.9
	7.3	5.2	1.2	2.1	1.4	3.5	5.2
14	7.3	5.1	0.9	1.2	0.9	6.1	5.1
	6.8	4.8	1.2	1.9	1.3	3.5	4.8

Figure IV-8a shows $p_{\max}$ versus $\rho U^2_{\max}$ for pressure sensors CH11–CH15 on the side wall, while Figure IV-8b shows $p_{\max}$ versus $\rho W^2_{\max}$ for pressure sensors CH01–CH03 on the top wall. Table IV-2 also lists the values of $p_{\max}$, $\rho U^2_{\max}$ or $\rho W^2_{\max}$, and the corresponding c_i for each of the eight sensors. In Figure IV-8a, the averaged impact coefficient determined by linear least-square regression is 4.20 with a coefficient of determination R^2 = 0.85, indicating a strong correlation between pressures and velocities (or kinetic energy) at the impact events. In comparison, the averaged impact coefficient in Figure IV-8b is only 0.77, whereas the very low R^2 = 0.39 indicating a weak correlation. By further examining the figure, the range of $\rho U^2_{\max}$ in

Figure IV-8a is within a narrow range with all values below $1.8\rho C^2$ (or 2.7 kPa), compared to a relatively wide range and higher values of $3.6\rho C^2$ to $9.0\rho C^2$ (or 5.0 kPa to 12.7 kPa) for $\rho W_{\max}^2$ in Figure 8b. On the other hand, the values of $p_{\max}$ are approximately in the same range with a maximum magnitude around $9\rho C^2$ (or 12.7 kPa).

(a)

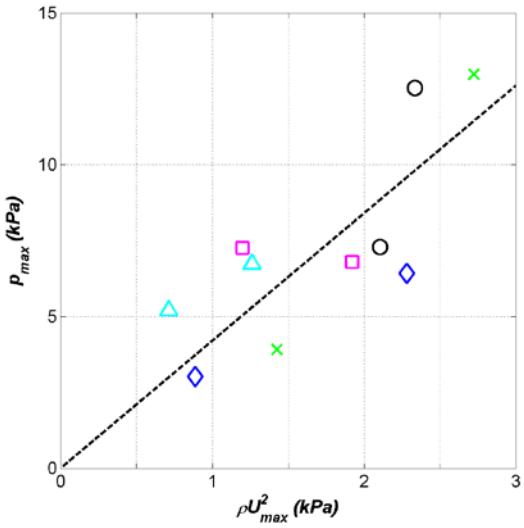

(b)

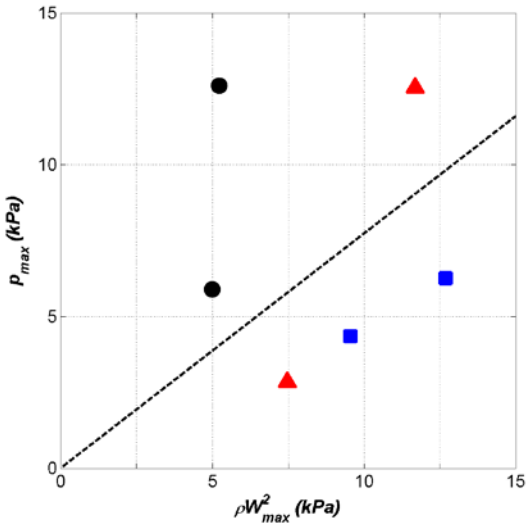

Figure IV-8 Derivation of impact coefficients. (a) $p_{\max}$ versus $\rho U_{\max}^2$ for CH11–CH15. (b) $p_{\max}$ versus $\rho W_{\max}^2$ for CH01–CH03. The solid line in each plot denotes the least square regression fit to the data. The fitted line has a slope of 4.20 and a coefficient of the determination R^2 = 0.85 in (a) and a slope of 0.77 and R^2 = 0.39 in (b).

The results in Table IV-2 and Figure IV-8 suggest that dynamic pressures produced by sloshing wave impingement on the side wall are linearly proportion to the local kinetic energy of the sloshing liquid advancing at a velocity close to the wave celerity prior to breaking. However, once the waves break and produce upward moving jets along the side wall, the dynamic impact on the container top wall may be strongly affected by the bubbly fluid density (likely with a high void fraction). The linear relation between the impact pressures and local kinetic energy directly calculated based on the single-phase liquid density is no longer valid. Local kinetic energy calculated based on the flow velocities and fluid density that accounts for void fraction should be considered. Without taking void fraction into account, a low correlation in the pressure-kinetic energy relation would appear as shown in Figure IV-8b. Based on green water measurements, Ariyarathne et al. (2012) concluded that including void fraction into equation (2) would improve the correlation since fluid density is otherwise mistakenly assumed to equal that of water. They proposed a modified relation as $p_{\max} = c_i \left(1-\alpha\right) \rho V_{\max}^2$ and found an improved regression for c_i. For practical applications, neither void fraction nor velocities are easy to obtain in a sloshing flow. The depth-based phase speed C may be the only kinematic variable that can be used to represent the characteristic velocity. Accordingly, we define a modified impact coefficient c_i' to connect the impact pressures with kinetic energy as follows

$$p_{\max} = c_i' \rho C^2 \tag{28}$$

where the modified impact coefficient $c_i' = c_i \beta^2$ with $\beta = V_{\max} / C$. The values of c_i' are included in Table IV-2 (c_i' also equals the third column $p_{\max} / \rho C^2$). As stated above, the c_i values ranging from 0.4 to 7.4 (a variation of nearly 20 times), and very different c_i values between pressures measured on the side wall (CH11–CH15) and that on the top wall (CH01–CH03) were observed. According to Table IV-2, the average value of c_i = 4.5 on the side wall is much greater than that of c_i = 1.0 on the top wall, a nearly 5 times difference. On the contrary, for CH11–CH15 on the side wall the range of c_i' is much narrower, ranging from 2.0 to 9.2 (a variation less than 5 times) with an average value of c_i' = 5.1. This average c_i' value on the side wall is nearly identical to the average c_i' value of 5.3 (a merely 3% difference) on the top wall for CH01–CH03.

The above discussion implies that the local peak kinetic energy that caused the corresponding peak pressure on the side wall may not be too different from the local peak kinetic

energy acting on the top wall, even though the average local peak velocities differ by 2.4 times and therefore the local kinetic energy differs by 5.8 times (average β = 1.0 for the side wall versus average β = 2.4 for the top wall in Table IV-2). Based on the numbers above and assuming that the peak pressures completely depend on the density accounted local kinetic energy, i.e., $p_{\max} = c_i \left(1-\alpha\right) \rho V_{\max}^2$, we estimated the void fraction to be around α = 0.83 (i.e., only 17% of the water density) in the uprising jet front. This way the jet produced the same impact pressure on the top wall as that produced by the horizontally advancing sloshing waves ($\alpha \approx 0$ assumed) on the side wall.

Since the average c_i' values are essentially identical ($c_i' \approx 5.2$) between the side wall and top wall sloshing impacts, the following equation may be used to approximate maximum impact pressures in liquid sloshing:

$$p_{\max} \approx 5.2 \rho g h \tag{29}$$

The above equation was obtained based on the averaged value of the present experimental data. The fluctuations in c_i' is quite large, whereas the applicability of Equation (4) may be limited to the present test condition. Future study is needed if the still water depth, the filling ratio, the tank dimensions, or the excitation frequency is varied. Other effects such as tank scale, tank geometry, and working fluids need also be considered for practical applications.

IV.6 Summary and conclusions

This paper studied both the kinematics and dynamics of liquid sloshing in a rectangular container with a 30% filling ratio. The sinusoidal oscillation at the resonant frequency of the tank motion produced breaking waves impinging on the structure side walls, and runup jets impacting the structure top wall. The evolution of the sloshing flow velocities was obtained using the BIV technique, while pressures were also recorded on the right side wall and the top wall. Impact pressures on the side wall and top wall due to the liquid sloshing were correlated with the local kinetic energy of the flows.

The study found that the high velocities of the sloshing waves were dominantly in the horizontal direction coincident with the direction of the tank motion. The horizontal velocities near the free surface reached 1.6C with $C = \sqrt{\rho g h}$ being the wave phase speed calculated based on the shallow water assumption. As the tank reached its maximum displacement and about to

reverse, the dominant flow changed its direction rapidly to vertical upward after the breaking wave crest impinging on the side wall and forming an up-rushing jet. The vertical velocity of the rising jet reached 3.4*C* before it impacted the top wall.

During the flip-through event as the fast moving wave crest collided with the side wall, the steep wave crest and the rapidly rising wave trough converged, resulting in a focused impact on the side wall at the SWL. The resulting impulsive peak pressure was recorded as about $10\rho gh$. The peak was immediately followed by the evident pressure oscillation with a frequency approximately 500 Hz, indicating an entrapment of air pockets between the wall and the sloshing wave front. After the wall impact, the multiphase up-rushing jet shot up and impacted the top wall. The magnitude of the pressure was again about $10\rho gh$, similar to that recorded by the breaking wave impact on the side wall, and the average rising time of the impulsive pressure was only 0.001*T* with *T* being the tank oscillation period.

Correlating the dynamic impact pressures with the corresponding local maximum flow velocities in the direction normal to the walls was performed by introducing the impact coefficient c_i and the modified impact coefficient c_i', defined as $p_{\max} = c_i \rho V_{\max}^2 = c_i' \rho C^2$ with $V_{\max}$ being the magnitude of the maximum local velocities. Based on the impacts of the horizontally dominant flow on the side wall, it was found that $c_i = 4.20$. The impact coefficient was greatly reduced to $c_i = 0.77$ based on the impacts of the uprising jet on the top wall. However, the average values of the modified impact coefficient c_i' between the side wall impacts and the top wall impacts were nearly identical, with the average value of $c_i' = 5.2$.

CHAPTER V

SUMMARY

This dissertation experimentally investigated the extreme wave kinematics emphasizing the wave interactions with constructed coastal and ocean environments. In CHAPTER I, general overview of this dissertation and specific objectives of each chapters were provided.

In CHAPTER II, the study investigated the velocity structures of the initial inundation flow during propagation of tsunami-like long waves interacting with inland complex topography produced by multi-cylinder patch arrays synthesizing discontinuous coastal vegetation system. The effects of the varying macro roughness from vegetation patches were provided through variations in the unit patch size and distance between equally spaced vegetation patches, respectively. For evaluations of rapidly evolving velocities of the turbulent wave runup front, the present study developed a “wave front tracing method”, implementing non-intrusive video imagery techniques. The first part of CHAPTER II provided detailed description on the developed “wave front tracing method". For validation of the theory, the velocity results from the present method were first compared to that from the analytical velocity calculations based on the mathematically defined wave front function. In additions, the wave front velocities based on the image recordings of the tsunami-like long wave propagations were compared to the direct velocity measurements from the ADV devices. The accuracy of the present method was discussed. The second part of the CHAPTER II applied the "wave front tracing method" to calculate the wave front velocities propagating on the macro roughness area while interacting with various configurations of the vegetation patch layouts. The velocity structures generated during the initial long-wave runup were provided for respective vegetation patch configurations. The characteristics of the result velocity field evolutions and their implications were discussed in relation to the effects of the size and spacing of the macro roughness patch layouts.

In CHAPTER III, the study performed the laboratory investigations to measure the green water velocities and dynamic impacts of the extreme ocean waves on a fixed deck structure in the deep ocean environment. The experiments are conducted in a large-scale ocean wave basin to simulate extreme ocean waves impinging on an offshore structure. Using the BIV technique, overall flow structures, temporal and spatial distributions of the maximum velocities were successfully evaluated. Pressure measurements were also conducted at various vertical and horizontal plains selected as wave impacting locations. Velocity measurements were compared

with the pressure measurements and correlations between the kinematic energy and dynamic impacts on the structure were evaluated. The results were presented in comparison to the results from similar two-dimensional and three-dimensional green water wave study. Especially, the comparisons were discussed with regard to the scaling effects of laboratory experiments.

In CHAPTER IV, the study is extended for more violent sloshing wave flows. The study experimentally investigated flow kinematics and impact pressures of a partially filled liquid sloshing flow during the periodic longitudinal motion of a rectangular tank. The evolution of the sloshing flow velocities was evaluated using the BIV technique, while the impact pressures were also measured on the right side wall and the top wall. Impact pressures on the side wall and top wall due to the liquid sloshing were correlated with the local kinetic energy calculated from the local impact flow velocities. Detailed analysis on the dynamic pressure structures was provided with regard to the impacting flow kinematics obtained from the local velocity information. Furthermore, the impact correlations were evaluated between the dynamic impact pressures and local kinematic energy. The correlation results were discussed in relation to the impulsiveness and degree of aeration of the impacting sloshing liquid.

REFERENCES

Abramson, H.N., 1966. The dynamic behavior of liquids in moving containers, with applications to space vehicle technology. Scientific and Technical Information Division, National Aeronautics and Space Administration, Washington, 467 p.

Akilli, H., Akar, A. and Karakus, C., 2004. Flow characteristics of circular cylinders arranged side-by-side in shallow water. *Flow Measurement and Instrumentation*, 15(4): pp. 187-197.

Akyildiz, H. and Ünal, E., N., 2005. Experimental investigation of pressure distribution on a rectangular tank due to the liquid sloshing. *Ocean Engineering*, 32(11–12): pp. 1503-1516.

Akyildız, H. and Ünal, E., N., 2006. Sloshing in a three-dimensional rectangular tank: Numerical simulation and experimental validation. *Ocean Engineering*, 33(16): pp. 2135-2149.

Ariyarathne, K., Chang, K.-A. and Mercier, R., 2012. Green water impact pressure on a three-dimensional model structure. *Experiments in Fluids*, 53(6): pp. 1879-1894.

Bagnold, R.A., 1939. Interim report on wave-pressure research, Institution of Civil Engineers.

Baldock, T.E., Cox, D., Maddux, T., Killian, J. and Fayler, L., 2009. Kinematics of breaking tsunami wavefronts: A data set from large scale laboratory experiments. *Coastal Engineering*, 56(5–6): pp. 506-516.

Bass, R.L., Bowles, J.E.B., Trudell, R.W., Navickas, J., Peck, J.C., Yoshimura, N., Endo, S. and Pots, B.F.M., 1985. Modeling criteria for scaled lng sloshing experiments. *Journal of Fluids Engineering*, 107(2): pp. 272-280.

Bird, P.A.D., Crawford, A.R., Hewson, P.J. and Bullock, G.N., 1998. An instrument for field measurement of wave impact pressures and seawater aeration. *Coastal Engineering*, 35(1–2): pp. 103-122.

Blackmore, P.A. and Hewson, P.J., 1984. Experiments on full-scale wave impact pressures. *Coastal Engineering*, 8(4): pp. 331-346.

Blenkinsopp, C.E. and Chaplin, J.R., 2007. Void fraction measurements in breaking waves. *Proceedings: Mathematical, Physical and Engineering Sciences*, 463(2088): pp. 3151-3170.

Blenkinsopp, C.E. and Chaplin, J.R., 2011. Void fraction measurements and scale effects in breaking waves in freshwater and seawater. *Coastal Engineering*, 58(5): pp. 417-428.

Bredmose, H., Brocchini, M., Peregrine, D.H. and Thais, L., 2003. Experimental investigation and numerical modelling of steep forced water waves. *Journal of Fluid Mechanics*, 490: pp. 217-249.

Bredmose, H., Peregrine, D.H. and Bullock, G.N., 2009. Violent breaking wave impacts. Part 2: Modelling the effect of air. *Journal of Fluid Mechanics*, 641: pp. 389-430.

Bredmose, H., Hunt-Raby, A., Jayaratne, R. and Bullock, G.N., 2010. The ideal flip-through impact: Experimental and numerical investigation. *Journal of Engineering Mathematics*, 67(1-2): pp. 115-136.

Buchner, B., 1995. The impact of green water on fpso design. *Proceedings of Offshore Technology Conference*, 1995: pp. 45-57.

Buchner, B. and Bunnik, T., 2007. Extreme wave effects on deepwater floating structures, Houston, Texas, Offshore Technology Conference, OTC - 18493.

Bullock, G., Müller, G., Obhrai, C., Peregrine, H., Bredmose, H. and Wolters, G., 2004. Field and laboratory measurement of wave impacts. In: *Coastal structures 2003*, American Society of Civil Engineers, pp. 343-355. *doi:10.1061/40733(147)29:* http://dx.doi.org/10.1061/40733(147)29.

Bullock, G.N., Crawford, A.R., Hewson, P.J., Walkden, M.J.A. and Bird, P.A.D., 2001. The influence of air and scale on wave impact pressures. *Coastal Engineering*, 42(4): pp. 291-312.

Bullock, G.N., Obhrai, C., Peregrine, D.H. and Bredmose, H., 2007. Violent breaking wave impacts. Part 1: Results from large-scale regular wave tests on vertical and sloping walls. *Coastal Engineering*, 54(8): pp. 602-617.

Catálan, P.A. and Haller, M.C., 2008. Remote sensing of breaking wave phase speeds with application to non-linear depth inversions. *Coastal Engineering*, 55(1): pp. 93-111.

Celebi, M.S. and Akyildiz, H., 2002. Nonlinear modeling of liquid sloshing in a moving rectangular tank. *Ocean Engineering*, 29(12): pp. 1527-1553.

Chan, E.-S., 1994. Mechanics of deep water plunging-wave impacts on vertical structures. *Coastal Engineering*, 22(1–2): pp. 115-133.

Chan, E.S. and Melville, W.K., 1988. Deep-water plunging wave pressures on a vertical plane wall. *Proceedings of the Royal Society of London a Mathematical and Physical Sciences*, 417(1852): pp. 95-131.

Chang, K.-A., Ariyarathne, K. and Mercier, R., 2011. Three-dimensional green water velocity on a model structure. *Experiments in Fluids*, 51(2): pp. 327-345.

Chanson, H., Aoki, S. and Hoque, A., 2006. Bubble entrainment and dispersion in plunging jet flows: Freshwater vs. Seawater. *Journal of Coastal Research*, 2006: pp. 664-677.

Chen, H.-c., 2011. CFD simulation of compressible two-phase sloshing flow in a lng tank. *Cell*, 1(1): pp. 31-57.

Cooker, M.J. and Peregrine, D.H., 1995. Pressure-impulse theory for liquid impact problems. *Journal of Fluid Mechanics*, 297: pp. 193-214.

Cox, D. and Shin, S., 2003. Laboratory measurements of void fraction and turbulence in the bore region of surf zone waves. *Journal of Engineering Mechanics*, 129(10): pp. 1197-1205.

Cox, D., Tomita, T., Lynett, P., Holman, R. and English, G., 2008. Tsunami inundation with macro-roughness in the constructed environment, *International Conference on Coastal Engineering*, Hamburg, Germany, 2008: pp. 1421–1432.

Cox, D.T. and Scott, C.P., 2001. Exceedance probability for wave overtopping on a fixed deck. *Ocean Engineering*, 28(6): pp. 707-721.

Cox, S.J. and Cooker, M.J., 1999. The motion of a rigid body impelled by sea-wave impact. *Applied Ocean Research*, 21(3): pp. 113-125.

Crawford, A., Bullock, G., Hewson, P. and Bird, a.P., 1997. Classification of breaking wave loads on vertical structures. *Journal of Waterway, Port, Coastal, and Ocean Engineering*, 119(4): pp. 381-397.

Curtis, W., Hathaway, K., Seabergh, W. and Holland, K., 2002. Measurement of physical model wave diffraction patterns using video. In: *Ocean wave measurement and analysis (2001)*, American Society of Civil Engineers, pp. 23-32. *doi:10.1061/40604(273)3:* http://dx.doi.org/10.1061/40604(273)3.

Dahdouh-Guebas, F., Jayatissa, L.P., Di Nitto, D., Bosire, J.O., Lo Seen, D. and Koedam, N., 2005. How effective were mangroves as a defence against the recent tsunami? *Current Biology*, 15(12): pp. R443-R447.

Danielsen, F. et al., 2005. The asian tsunami: A protective role for coastal vegetation. *Science*, 310(5748): pp. 643.

Delorme, L., Colagrossi, A., Souto-Iglesias, A., Zamora-Rodríguez, R. and Botía-Vera, E., 2009. A set of canonical problems in sloshing, part I: Pressure field in forced roll—comparison between experimental results and sph. *Ocean Engineering*, 36(2): pp. 168-178.

Dillingham, J., 1981. Motion studies of a vessel with water on deck. *Marine Technology*, 18(1): pp. 38-50.

Eswaran, M., Singh, A. and Saha, U.K., 2011. Experimental measurement of the surface velocity field in an externally induced sloshing tank. *Proceedings of the Institution of Mechanical Engineers, Part M: Journal of Engineering for the Maritime Environment*, 225(2): pp. 133-148.

Faltinsen, O.M., 1974. A non-linear theory of sloshing in rectangular tanks. *Journal of Ship Research*, 18(4): pp. 224-241.

Faltinsen, O.M., Rognebakke, O.F., Lukovsky, I.A. and Timokha, A.N., 2000. Multidimensional modal analysis of nonlinear sloshing in a rectangular tank with finite water depth. *Journal of Fluid Mechanics*, 407: pp. 201-234.

Faltinsen, O.M., Greco, M. and Landrini, M., 2002. Green water loading on a fpso. *Journal of Offshore Mechanics and Arctic Engineering*, 124(2): pp. 97-103.

Faltinsen, O.M., Rognebakke, O.F. and Timokha, A.N., 2005. Classification of three-dimensional nonlinear sloshing in a square-base tank with finite depth. *Journal of Fluids and Structures*, 20(1): pp. 81-103.

Faltinsen, O.M., Firoozkoohi, R. and Timokha, A.N., 2011. Analytical modeling of liquid sloshing in a two-dimensional rectangular tank with a slat screen. *Journal of Engineering Mathematics*, 70(1-3): pp. 93-109.

Fernando, H.J.S., Samarawickrama, S.P., Balasubramanian, S., Hettiarachchi, S.S.L. and Voropayev, S., 2008. Effects of porous barriers such as coral reefs on coastal wave propagation. *Journal of Hydro-environment Research*, 1(3–4): pp. 187-194.

Forbes, K. and Broadhead, J., 2007. The role of coastal forests in the mitigation of tsunami impacts, Food and Agriculture Organization of the United Nations, Regional Office for Asia and the Pacific, Bangkok, Tailand.

Forristall, G.Z., 2000. Wave crest distributions: Observations and second-order theory. *Journal of Physical Oceanography*, 30(8): pp. 1931-1943.

Franco, C. and Franco, L., 1999. Overtopping formulas for caisson breakwaters with nonbreaking 3d waves. *Journal of Waterway, Port, Coastal, and Ocean Engineering*, 125(2): pp. 98-108.

Greco, M., Faltinsen, O.M. and Landrini, M., 2001. Basic studies of water on deck, *Twenty-Third Symposium on Naval Hydrodynamics*, Val de Reuil , France, The National Academies Press, 2001.

Hamoudi, B. and Varyani, K.S., 1998. Significant load and green water on deck of offshore units/vessels. *Ocean Engineering*, 25(8): pp. 715-731.

Hattori, M., Arami, A. and Yui, T., 1994. Wave impact pressure on vertical walls under breaking waves of various types. *Coastal Engineering*, 22(1–2): pp. 79-114.

Hirt, C.W. and Nichols, B.D., 1981. Volume of fluid (vof) method for the dynamics of free boundaries. *Journal of Computational Physics*, 39(1): pp. 201-225.

Holland, T.K., Holman, R.A., Lippmann, T.C., Stanley, J. and Plant, N., 1997. Practical use of video imagery in nearshore oceanographic field studies. *Oceanic Engineering, IEEE Journal of*, 22(1): pp. 81-92.

Holman, R.A. and Stanley, J., 2007. The history and technical capabilities of argus. *Coastal Engineering*, 54(6–7): pp. 477-491.

Hull, P. and Müller, G., 2002. An investigation of breaker heights, shapes and pressures. *Ocean Engineering*, 29(1): pp. 59-79.

Ibrahim, R.A., 2005. Liquid sloshing dynamics: Theory and applications, Wayne State University, Michigan, Cambridge, 2005.

Kaplan, M., Renaud, F.G. and Luchters, G., 2009. Vulnerability assessment and protective effects of coastal vegetation during the 2004 tsunami in sri lanka. *Natural Hazards and Earth System Sciences*, 9(4): pp. 1479-1494.

Kirkgöz, M.S., 1990. An experimental investigation of a vertical wall response to breaking wave impact. *Ocean Engineering*, 17(4): pp. 379-391.

Kobus, H. and Koschitzky, H.P., 1991. Local surface aeration at hydraulic structures, in air entrainment in free-surface flows. *IAHR, Hydraulic Design Structures Series*, 4: pp. 29–53.

Lam, K., Li, J.Y., Chan, K.T. and So, R.M.C., 2003. Flow pattern and velocity field distribution of cross-flow around four cylinders in a square configuration at a low reynolds number. *Journal of Fluids and Structures*, 17(5): pp. 665-679.

Lamarre, E. and Melville, W.K., 1992. Instrumentation for the measurement of void-fraction in breaking waves: Laboratory and field results. *IEEE Journal of Oceanic Engineering*, 17(2): pp. 204-215.

Lamarre, E. and Melvillea, W.K., 1994. Void-fraction measurementsa nd sound-speedf ields in bubble plumes generated by breaking waves. *Journal of the Acoustical Society of America*, 95(3): pp. 1317-1328.

Lee, T.-h., Zhou, Z. and Cao, Y., 2002. Numerical simulations of hydraulic jumps in water sloshing and water impacting. *Journal of Fluids Engineering*, 124(1): pp. 215-226.

Leonhardsen, R.L., Ersdal, G. and Kvitrud, A., 2001. Experience and risk assessment of fpsos in use on the norwegian continental shelf: Descriptions of events. *The 11th*

International Offshore and Polar Engineering Conference, Stavanger, Norway, 1: pp. 309–314.

Lim, H.-J., Chang, K.-A., Su, C.B. and Chen, C.-Y., 2008. Bubble velocity, diameter, and void fraction measurements in a multiphase flow using fiber optic reflectometer. *Review of Scientific Instruments*, 79(12): pp. 125105.

Lin, C., Hsieh, S., Kuo, K. and Chang, K., 2008. Periodic oscillation caused by a flow over a vertical drop pool. *Journal of Hydraulic Engineering*, 134(7): pp. 948-960.

Lin, C., Hsieh, S.-C., Lin, I.J., Chang, K.-A. and Raikar, R., 2012. Flow property and self-similarity in steady hydraulic jumps. *Experiments in Fluids*, 53(5): pp. 1591-1616.

Lippmann, T.C. and Holman, R.A., 1989. Quantification of sand bar morphology: A video technique based on wave dissipation. *Journal of Geophysical Research: Oceans*, 94(C1): pp. 995-1011.

Liu, P.L.F., Wu, T.R., Raichlen, F., Synolakis, C.E. and Borrero, J.C., 2005. Runup and rundown generated by three-dimensional sliding masses. *Journal of Fluid Mechanics*, 536: pp. 107-144.

Lugni, C., Brocchini, M. and Faltinsen, O.M., 2006. Wave impact loads: The role of the flip-through. *Physics of Fluids*, 18(12): pp. 122101-122117.

Lugni, C., Miozzi, M., Brocchini, M. and Faltinsen, O.M., 2010. Evolution of the air cavity during a depressurized wave impact. I. The kinematic flow field. *Physics of Fluids*, 22(5): pp. 056101-056117.

Lynett, P., 2011. Tsunami inundation, modeling of. In: *Extreme environmental events*, R.A. Meyers (Editor), Springer, New York, pp. 1008-1021. http://dx.doi.org/10.1007/978-1-4419-7695-6_53.

Mikelis, N.E., Miller, J.K. and Taylor, K.V., 1984. Sloshing in partially filled liquid tanks and its effect on ship motions: Numerical simulations and experimental verification. *Royal institution of naval architects transactions* (126). Lloyd's Register of Shipping, London, UK.

Miller, R.L., 1968. Experimental determination of run-up of undular and fully developed bores. *Journal of Geophysical Research*, 73(14): pp. 4497-4510.

Mori, N., Liu, P.C. and Yasuda, T., 2002. Analysis of freak wave measurements in the sea of japan. *Ocean Engineering*, 29(11): pp. 1399-1414.

Mori, N. and Cox, D.T., 2003. Dynamic properties of green water event in the overtopping of extreme waves on a fixed dock. *Ocean Engineering*, 30(16): pp. 2021-2052.

Nandasena, N.A.K., Tanaka, N. and Tanimoto, K., 2008. Perspective of coastal vegetation patches with topography variations for tsunami protection in 2d - numerical modeling. *Hydraulic Engineering*, 52: pp. 133-138.

Nepf, H.M., 1999. Drag, turbulence, and diffusion in flow through emergent vegetation. *Water Resources Research*, 35(2): pp. 479-489.

Nepf, H.M., 2004. Vegetated flow dynamics. In: *The ecogeomorphology of tidal marshes, Coastal estuarine stud.*, AGU, Washington, DC, pp. 137-163. http://dx.doi.org/10.1029/CE059p0137.

Nepf, H.M., 2012. Hydrodynamics of vegetated channels. *Journal of Hydraulic Research*, 50(3): pp. 262-279.

Ochi, M.K. and Tsai, C.-H., 1984. Prediction of impact pressure induced by breaking waves on vertical cylinders in random seas. *Applied Ocean Research*, 6(3): pp. 157-165.

Okamoto, T. and Kawahara, M., 1990. Two-dimensional sloshing analysis by lagrangian finite element method. *International Journal for Numerical Methods in Fluids*, 11(5): pp. 453-477.

Okamoto, T. and Kawahara, M., 1997. 3-d sloshing analysis by an arbitrary lagrangian-eulerian finite element method. *International Journal of Computational Fluid Dynamics*, 8(2): pp. 129-146.

Olsen, H., 1976. What is sloshing? *Seminar on Liquid Sloshing*, Det Norske Veritas.

Oumeraci, H., Klammer, P. and Partenscky, H., 1993. Classification of breaking wave loads on vertical structures. *Journal of Waterway, Port, Coastal, and Ocean Engineering*, 119(4): pp. 381-397.

Oumeraci, H., 1994. Review and analysis of vertical breakwater failures — lessons learned. *Coastal Engineering*, 22(1–2): pp. 3-29.

Oumeraci, H., Bruce, T., Klammer, P. and Easson, W.J., 1995. PIV measurement of breaking wave kinematics and impact loading of caisson breakwaters, *23rd International Conference on Coastal Engineering*, Venice, Italy., 1995.

Panigrahy, P.K., Saha, U.K. and Maity, D., 2009. Experimental studies on sloshing behavior due to horizontal movement of liquids in baffled tanks. *Ocean Engineering*, 36(3–4): pp. 213-222.

Pantazopoulous, 1988. Three-dimensional sloshing of water on decks (25). Society of Naval Architects and Marine Engineers, Jersey City, NJ, ETATS-UNIS.

Park, H., Cox, D.T., Lynett, P.J., Wiebe, D.M. and Shin, S., 2013. Tsunami inundation modeling in constructed environments: A physical and numerical comparison of free-surface elevation, velocity, and momentum flux. *Coastal Engineering*, 79(0): pp. 9-21.

Pedrozo-Acuña, A., Simmonds, D.J. and Reeve, D.E., 2008. Wave-impact characteristics of plunging breakers acting on gravel beaches. *Marine Geology*, 253(1–2): pp. 26-35.

Pedrozo-Acuña, A., de Alegría-Arzaburu, A.R., Torres-Freyermuth, A., Mendoza, E. and Silva, R., 2011. Laboratory investigation of pressure gradients induced by plunging breakers. *Coastal Engineering*, 58(8): pp. 722-738.

Peregrine, D.H., 2003. Water-wave impact on walls. *Annual Review of Fluid Mechanics*, 35(1): pp. 23-43.

Rafiee, A., Pistani, F. and Thiagarajan, K., 2011. Study of liquid sloshing: Numerical and experimental approach. *Computational Mechanics*, 47(1): pp. 65-75.

Raupach, M.R. and Shaw, R.H., 1982. Averaging procedures for flow within vegetation canopies. *Boundary-Layer Meteorol*, 22(1): pp. 79-90.

Raupach, M.R., 1992. Drag and drag partition on rough surfaces. *Boundary-Layer Meteorol*, 60(4): pp. 375-395.

Ray, S.F., 2002. Applied photographic optics: Lenses and optical systems for photography, film, video, electronic and digital imaging, 2002. Oxford: Focal, ISBN: 0240515404.

Rhee, S.H., 2005. Unstructured grid based reynolds-averaged navier-stokes method for liquid tank sloshing. *Journal of Fluids Engineering*, 127(3): pp. 572-582.

Rivillas-Ospina, G., Pedrozo-Acuña, A., Silva, R., Torres-Freyermuth, A. and Gutierrez, C., 2012. Estimation of the velocity field induced by plunging breakers in the surf and swash zones. *Experiments in Fluids*, 52(1): pp. 53-68.

Rockwell, D., Lin, J.C., Cetiner, O., Downes, K. and Yang, Y., 2001. Quantitative imaging of the wake of a cylinder in a steady current and free-surface waves. *Journal of Fluids and Structures*, 15(3–4): pp. 427-443.

Rueben, M., Holman, R., Cox, D., Shin, S., Killian, J. and Stanley, J., 2011. Optical measurements of tsunami inundation through an urban waterfront modeled in a large-scale laboratory basin. *Coastal Engineering*, 58(3): pp. 229-238.

Ryan, A., 2010. Image processing for estimating run-up. *Personal communication* Oregon State University.

Ryu, Y., Chang, K.-A. and Lim, H.-J., 2005. Use of bubble image velocimetry for measurement of plunging wave impinging on structure and associated green water. *Measurement Science and Technology*, 16: pp. 1945-1953.

Ryu, Y., 2006. Extreme wave impinging and overtopping. *Doctor of Philosophy Dissertation*, Texas A&M University, College Station, TX, 170 p.

Ryu, Y., Chang, K.-A. and Mercier, R., 2007a. Application of dam-break flow to green water prediction. *Applied Ocean Research*, 29(3): pp. 128-136.

Ryu, Y., Chang, K.-A. and Mercier, R., 2007b. Runup and green water velocities due to breaking wave impinging and overtopping. *Experiments in Fluids*, 43(4): pp. 555-567.

Ryu, Y. and Chang, K.-A., 2008. Green water void fraction due to breaking wave impinging and overtopping. *Experiments in Fluids*, 45(5): pp. 883-898.

Short, N., M., Sr. 2005. The Everglades: America's Most Threatened Ecosystem, Federation Of American Scientists, *http://www.fas.org/irp/imint/docs/rst/sect3/sect3_8.html*, Edited.

Stansberg, C.T., 2000. Nonlinear extreme wave evolution in random wave groups. *International Offshore and Polar Engineering Conference*, Seattle, USA, 3: pp. 1-8.

Stansberg, C.T. and Nielsen, F.G., 2001. Nonlinear wave–structure interactions on floating production systems. *The 11th International Offshore and Polar Engineering Conference*, Stavanger, Norway, ISOPE, 4: pp. 363–372.

Stockdon, H.F. and Holman, R.A., 2000. Estimation of wave phase speed and nearshore bathymetry from video imagery. *Journal of Geophysical Research: Oceans*, 105(C9): pp. 22015-22033.

Stone, B. and Shen, H., 2002. Hydraulic resistance of flow in channels with cylindrical roughness. *Journal of Hydraulic Engineering*, 128(5): pp. 500-506.

Synolakis, C., Imamura, F., Tsuji, Y., Matsutomi, H., Tinti, S., Cook, B., Chandra, Y.P. and Usman, M., 1995. Damage, conditions of east java tsunami of 1994 analyzed. *Eos, Transactions American Geophysical Union*, 76(26): pp. 257-257.

Takemura, T. and Tanaka, N., 2007. Flow structures and drag characteristics of a colony-type emergent roughness model mounted on a flat plate in uniform flow. *Fluid Dynamics Research*, 39(9–10): pp. 694-710.

Tanaka, N., Sasaki, Y., Mowjood, M.I.M., Jinadasa, K.B.S.N. and Homchuen, S., 2007. Coastal vegetation structures and their functions in tsunami protection: Experience of the recent indian ocean tsunami. *Landscape and Ecological Engineering*, 3(1): pp. 33-45.

Tanaka, N., 2009. Vegetation bioshields for tsunami mitigation: Review of effectiveness, limitations, construction, and sustainable management. *Landscape and Ecological Engineering*, 5(1): pp. 71-79.

Tanaka, N., Nandasena, N.A.K., Jinadasa, K.B.S.N., Sasaki, Y., Tanimoto, K. and Mowjood, M.I.M., 2009. Developing effective vegetation bioshield for tsunami protection. *Civil Engineering and Environmental Systems*, 26(2): pp. 163-180.

Tanaka, N., 2011. Effectiveness and limitations of vegetation bioshield in coast for tsunami disaster mitigagation. In: *The tsunami threat - research and technology*, N.-A. Mörner (Editor), InTech, pp. 161-178.

Tanaka, N., Jinadasa, K.B.S.N., Mowjood, M.I.M. and Fasly, M.S.M., 2011. Coastal vegetation planting projects for tsunami disaster mitigation: Effectiveness evaluation of new establishments. *Landscape and Ecological Engineering*, 7(1): pp. 127-135.

Thiagarajan, K.P., Rakshit, D. and Repalle, N., 2011. The air–water sloshing problem: Fundamental analysis and parametric studies on excitation and fill levels. *Ocean Engineering*, 38(2–3): pp. 498-508.

Thuy, N.B., Tanimoto, K., Tanaka, N., Harada, K. and Iimura, K., 2009. Effect of open gap in coastal forest on tsunami run-up—investigations by experiment and numerical simulation. *Ocean Engineering*, 36(15–16): pp. 1258-1269.

Thuy, N.B., Tanimoto, K. and Tanaka, N., 2010. Flow and potential force due to runup tsunami around a coastal forest with a gap: experiments and numerical simulations. *Science of Tsunami Hazards*, 29(2): pp. 43-69.

Ting, F.C.K. and Kirby, J.T., 1994. Observation of undertow and turbulence in a laboratory surf zone. *Coastal Engineering*, 24(1–2): pp. 51-80.

Tomita, T. and Honda, K., 2007. Tsunami estimation including effect of coastal structures and buildings by 3d model, *Coastal Structures*, Venice, 2007.

United States Environmental Protection Agency (2013), Water:Wetlands, United States Environmental Protection Agency, http://water.epa.gov/type/wetlands/marsh.cfm

Wang, C.Y., Teng, J.T. and Huang, G.P.G., 2011. Numerical simulation of sloshing motion inside a two dimensional rectangular tank by level set method. *International Journal of Numerical Methods for Heat & Fluid Flow*, 21(1): pp. 5-31.

White, B.L. and Nepf, H.M., 2008. A vortex-based model of velocity and shear stress in a partially vegetated shallow channel. *Water Resources Research*, 44(1): pp. W01412.

Wood, D., Peregrine, D. and Bruce, T., 2000. Wave impact on a wall using pressure-impulse theory. I: Trapped air. *Journal of Waterway, Port, Coastal, and Ocean Engineering*, 126(4): pp. 182-190.

Wu, N.-J. and Chang, K.-A., 2011. Simulation of free-surface waves in liquid sloshing using a domain-type meshless method. *International Journal for Numerical Methods in Fluids*, 67(3): pp. 269-288.

Xu, L. and Barltrop, N., 2008. Bow impact loading on FPSOs 2—theoretical investigation. *Ocean Engineering*, 35(11–12): pp. 1158-1165.

Xu, L., Barltrop, N. and Okan, B., 2008. Bow impact loading on FPSOs 1—experimental investigation. *Ocean Engineering*, 35(11–12): pp. 1148-1157.

Yeh, H., 1991. Tsunami bore runup. *Natural Hazards*, 4(2-3): pp. 209-220.

Yeh, H.H. and Mok, K.-M., 1990. On turbulence in bores. *Physics of Fluids A: Fluid Dynamics*, 2(5): pp. 821-828.

Zhou, Z., de Kat, J. O., and Buchner, B, 1999. A nonlinear 3-d approach to simulate green water dynamics on deck,, *Proc 7th International Sympo- sium on Numerical Ship Hydrodynamics*, 1999.

Zong, L. and Nepf, H., 2010. Flow and deposition in and around a finite patch of vegetation. *Geomorphology*, 116(3–4): pp. 363-372.

Zong, L. and Nepf, H., 2011. Spatial distribution of deposition within a patch of vegetation. *Water Resources Research*, 47(3), W03516.